

Transport Theory for Metals with Excitonic Instabilities

DISSERTATION

zur Erlangung des akademischen Grades

Doctor rerum naturalium

(Dr. rer. nat.)

vorgelegt

der Fakultät Mathematik und Naturwissenschaften der
Technischen Universität Dresden

von

Dipl.-Phys. Maxim Breitzkreiz

geboren am 30.03.1986 in Omsk

eingereicht am 30.04.2015

Die Dissertation wurde im Zeitraum von Dezember 2011
bis April 2015 am Institut für theoretische Physik
angefertigt.

Erstgutachter: Prof. Dr. Carsten Timm
Zweitgutachter: Prof. Dr. Jörg Schmalian

Abstract

Metals with excitonic instabilities are multiband systems with significant electron-electron interaction. The electronic transport in such systems is affected by collective fluctuations of the electrons, leading to anomalous features in the measured transport coefficients. Many of these anomalies have not been well understood because the transport mechanisms in these systems tend to be rather complex. The complexity arises, on the one hand, from the multiband nature and, on the other, from the anisotropic scattering of electrons accompanied by emitting or absorbing collective fluctuations. Previous works considering scattering due to collective fluctuations have mainly focused on single-band systems, for example in the context of the normal-state transport in cuprates. The recent discovery of high-temperature superconductivity in iron pnictides has renewed the interest in multiband systems.

Exploring the transport mechanisms in multiband systems, I find some interesting new aspects, which do not occur in single-band systems. In particular, anisotropic scattering in a model with electronlike and holelike Fermi surfaces can lead to a negative conductivity contribution of the minority carriers, i.e., in an electric field, the minority carriers drift in the direction opposite of what one would expect based on their charge. I show that this effect can explain a reduced magnetoresistance in connection with an enhanced Hall coefficient, which has been measured in pnictides.

Of particular interest are multiband models with hot spots on the Fermi surface, in part because of their relevance for the iron pnictides. Hot spots are states with enhanced scattering and therefore reduced excitation lifetimes. In single-band systems, the hot spots are found to have a much lower contribution to the total conductivity than other parts of the Fermi surface, which leads to the so-called hot-spot structure. I show that in the multiband case, the conductivity contributions are much more isotropic around the Fermi surface so that hot spots contribute to transport with a similar strength as other parts of the Fermi surface. I discuss this effect on the basis of an approximate analytical solution of

the transport problem and numerically calculate the temperature dependence of several transport coefficients.

It turns out that in the nematic phase of iron pnictides, the unexpectedly strong conductivity contribution of hot spots can explain the puzzling behavior of the resistive anisotropy. I show that the experimental observations can be explained within a scenario in which the anisotropy is mainly due to the broken symmetry of the spin-fluctuation spectrum in the nematic phase.

In the spin-density-wave state, strongly anisotropic scattering can arise due to the propagating magnons. Using a two-band model relevant for iron pnictides, I find that this scattering can lead to an unusual interruption of the orbital motion of electrons in the magnetic field. As a consequence, the low-field magnetoresistance is linear with an alternating sign of the slope as a function of the direction of the current. In strong magnetic fields, the interrupted orbital motion makes the system unstable, which is characterized by a drop of the resistivity to zero.

Contents

1	Introduction and overview	1
1.1	Transport in condensed matter	1
1.2	Iron pnictides	2
1.3	Outline	6
2	Transport theory	8
2.1	Non-equilibrium Green's function approach	8
2.2	Scattering due to collective excitations	10
2.3	Collective excitations and umklapp scattering	12
2.4	Transport in the presence of a magnetic field	15
2.5	Conductivity of single crystals and twinned crystals	17
3	Negative transport times due to anisotropic interband scattering	22
3.1	Introduction	22
3.2	Solution of the Boltzmann equation	24
3.3	Transport times	25
3.4	Transport coefficients	28
3.4.1	Resistivity	28
3.4.2	Magnetoresistance and Hall coefficient	28
3.5	Conclusions	31
4	Transport in multiband systems with hot spots on the Fermi surface	32
4.1	Introduction	32
4.2	Model	33
4.3	Analytical considerations	36
4.3.1	Angular shift towards the hot spot	38
4.4	Results	41
4.4.1	Scattering rate	42
4.4.2	Hot-spot picture	43
4.4.3	Transport coefficients	44

4.5	Conclusions	50
5	Resistive anisotropy in the nematic phase of iron pnictides	52
5.1	Introduction	52
5.2	Model	54
5.3	Resistive anisotropy	56
5.3.1	Vanishing orbital splitting	57
5.3.2	Finite orbital splitting	61
5.4	Conclusions	61
6	Transport in the spin-density-wave phase of iron pnictides	63
6.1	Introduction	63
6.2	Model	64
6.3	Spin-fluctuation scattering	67
6.4	Interrupted orbital motion	72
6.5	Magnetoresistance	75
6.6	Conclusions	80
7	Summary and outlook	81
	Bibliography	84

1 Introduction and overview

1.1 Transport in condensed matter

Transport phenomena in condensed matter belong to the most fascinating manifestations of quantum mechanics. A highlight is the integer quantum Hall effect, which is now used to measure the ratio of two fundamental constants of nature to very high precision [1]. Even more intriguing and theoretically challenging effects, such as the fractional quantum Hall effect, can arise due to significant electronic correlations. One class of correlated systems are metals with excitonic instabilities, which show interesting transport anomalies, many of which could not be understood so far [2–7].

The principle underlying most of the theory of transport is linear response, in which the response of the system, e.g., in the form of a finite macroscopic current, is considered to be proportional to the external field that drives the system out of equilibrium. There are two different approaches: The Kubo approach [8] considers the correlation of *two* propagating particles in the *equilibrium* state, while the non-equilibrium approach [9, 10] considers the propagation of *one* particle in the *non-equilibrium* state. The general principle behind the fact that the transport problem can be tackled from two different angles is the fluctuation-dissipation theorem, which relates the correlation of two single-particle excitations to the dissipation of one single-particle excitation.

The theoretical description of the electronic transport in metals involves the consideration of different scattering processes through which the system can relax into the equilibrium state. An electron can scatter off impurities, phonons, and also off other electrons. The latter is the most complicated process since it involves at least one other electron, which itself contributes to the transport. In fact, scattering due to electron-electron interaction can be even more complex in case of significant electronic correlations. The scattering of a single electron can then be part of a long chain of correlated scattering processes. One can nevertheless still maintain a picture of single-electron scattering by considering that indivi-

dual electrons scatter off a *collective fluctuation* of the interacting electron gas. Electrons can emit or absorb a collective fluctuation with, in general, *anisotropic* distribution of scattering momenta: Certain scattering momenta can be preferred due to the peaks in the spectrum of the fluctuations.

The development of a theoretical description, which accounts for such an *anisotropic* scattering due to collective fluctuations, is a central goal of this thesis. In the simple case of *isotropic* scattering the relaxation of an electron is determined by its lifetime, i.e. the inverse imaginary part of its selfenergy. Anisotropic scattering, on the other hand, complicates the relaxation process such that the mean relaxation time of an electron no longer coincides with its lifetime. In fact, the deviations of transport coefficients from the predictions based purely on lifetimes can be very significant, as has been emphasized in connection with the critical behavior at magnetic phase transitions [11, 12], as well as in connection with spin-fluctuation scattering in cuprates [13] and heavy-fermion materials [14]. Most of the theoretical considerations which correctly account for the anisotropic scattering are based on single-band models. In this thesis I will extend the transport theory to the multiband case, for which, as it turns out, some transport paradigms have to be reconsidered.

The multiband description is relevant for systems that are close to an excitonic instability [15–19], which is characterized by the condensation of electrons and holes from different Fermi surfaces (FSs) [20, 21]. This instability is favored if the FSs are close to nesting, i.e., if there exist wavevectors \mathbf{Q}_i which approximately connect extensive parts of two FSs [22]. An example of FSs which are close to nesting of real materials is shown in Fig. 1.1. Nesting typically leads to enhanced charge and spin susceptibilities $\chi(\mathbf{q})$ for wavevectors $\mathbf{q} \approx \mathbf{Q}_i$. Below the critical temperature, spin-density-wave (SDW) and charge-density-wave states with wavevectors \mathbf{Q}_i can be realized [23–26]. A system in the SDW state with non-vanishing FSs is often called an *itinerant antiferromagnet*, since the magnetic moment is carried by delocalized electrons, in contrast to a magnetic order with *localized* magnetic moments, typically found in more strongly correlated systems.

1.2 Iron pnictides

The discovery of high-temperature superconductivity in iron pnictides in 2008 [28, 29] has significantly raised the interest in excitonic models. Besides superconductivity with a critical temperature of up to 56 K [30, 31], many other intriguing

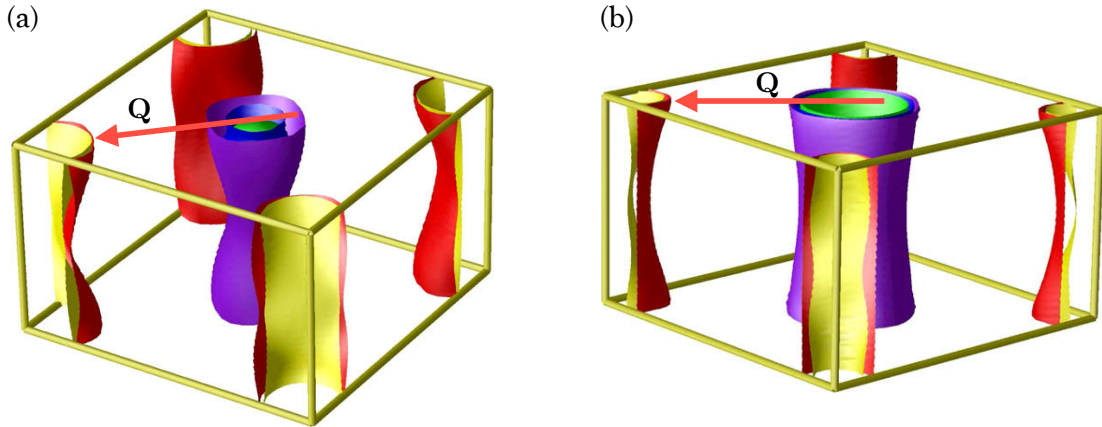


Figure 1.1: Nearly nested FSs of (a) the paramagnetic 10% electron-doped and (b) the 10% hole-doped BaFe_2As_2 calculated within the local-density and virtual-crystal approximations. The Brillouin zone corresponds to the two-iron unit cell. The three FSs in the center of the Brillouin zone are holelike, whereas the two FSs in the corners are electronlike. From Ref. [27].

phenomena are associated with iron pnictides and are currently the subject of intense research [32–36]. A simplified phase diagram is sketched in Fig. 1.2(a) to highlight some aspects that will be relevant in the following. The ground state of the parent compounds is a metallic SDW state with an ordering temperature T_N between 100 and 200 K [34]. The SDW transition is accompanied by a structural transition at the temperature T_s from a tetragonal lattice structure with equal in-plane lattice constants $a_T = b_T$ for $T > T_s$ to an orthorhombic structure for $T < T_s$ with lattice constants $a_O \neq b_O$. In some cases the structural transition appears slightly above T_N , whereas in others it coincides with the magnetic transition. By applying uniaxial strain, T_s can be shifted above T_N also in the latter case. The phase between T_s and T_N is often called *Ising nematic* or just *nematic* [33, 37] and will be discussed in more detail in chapter 5. The stripe antiferromagnetic order below T_N is commensurate with the lattice; the possible ordering vectors $\mathbf{Q}_X = (0, \pi/a_O)$ and $\mathbf{Q}_Y = (\pi/b_O, 0)$ are half of the reciprocal lattice vectors.

The 122 systems $A\text{Fe}_2\text{As}_2$, where A stands for an alkaline-earth metal, are the most interesting family for transport investigations because single crystals have been grown that are large enough for transport measurements. Figure 1.1 shows the FSs of two 122 systems obtained from local-density-approximation calculations. The FSs show a roughly cylindrical shape, hence two-dimensional models are often employed. The two-dimensionality results from the layered crystal struc-

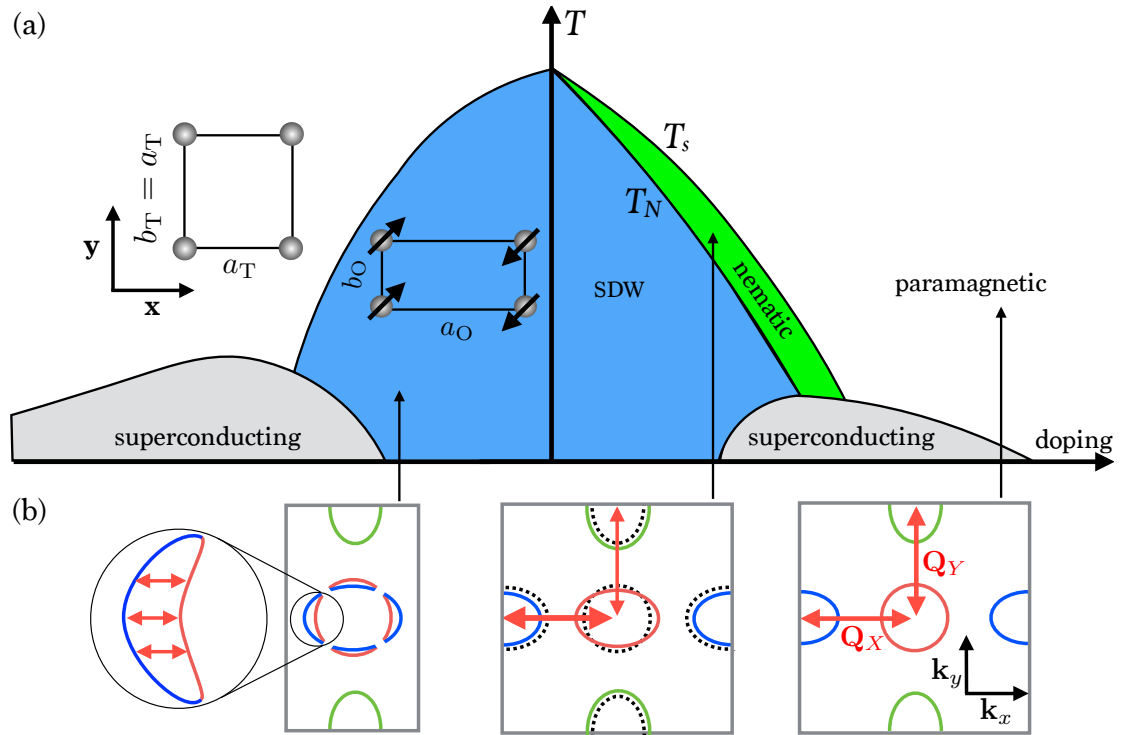


Figure 1.2: (a) Schematic phase diagram of iron pnictides. The lattice structure is tetragonal in the paramagnetic phase and orthorhombic in the nematic and SDW phases with in-plane (xy -plane) lattice constants a_T , b_T and a_O , b_O , respectively. The cartoon of the orthorhombic lattice structure exaggerates the real distortion, which is only a few tenth of a per cent [38]. The direction of the stripe antiferromagnetic ordering vector is set as the x -direction throughout this work. (b) From right to left: FSs of the two-band model used in chapters 4–6 to study transport in the paramagnetic, nematic, and SDW phase of iron pnictides, respectively. In the paramagnetic phase, the FSs consist of a nearly circular hole pocket (red) and two elliptical electron pockets (blue and green). The nematic transition at T_s leads to the splitting of the iron d_{xz} and d_{yz} orbitals. As a result, the FSs distort in comparison to the FSs of the paramagnetic state (dotted lines). The SDW transition at T_N leads to the doubling of the unit cell and the corresponding folding of the Brillouin zone. The SDW gap opens at the crossing points of the hole pocket and the backfolded (blue) electron pocket, resulting in four banana-shaped FSs. The red arrows indicate the scattering of electrons due to spin fluctuations. In the nonmagnetic phases, the scattering is enhanced for scattering vectors close to \mathbf{Q}_X and \mathbf{Q}_Y . In the nematic phase, the broken symmetry of the spin-fluctuation peaks at \mathbf{Q}_X and \mathbf{Q}_Y gives rise to stronger scattering in the direction \mathbf{Q}_X . Finally, In the SDW phase, scattering is enhanced between different sides of the banana pockets.

ture [35]. Some resistivity measurements for 122 compounds show a conductivity ratio between out-of-plane and in-plane conductivities on the order of 100 [39], which supports a very weak out-of-plane dispersion. Other measurements, however, find a much smaller ratio [40].

A peculiarity of the iron-pnictide bandstructure is the complicated mixing of all five iron $3d$ orbitals at the Fermi energy [41], from which the d_{xy} , d_{xz} , and d_{yz} are the most dominant ones. The importance of the orbital origin of the bands has been emphasized by several authors [42–47]. Nevertheless, there are many theoretical considerations using effective band models that mimic the correct FS topology [48] but neglect the orbital content [18, 19, 26, 27, 36, 37, 49–55]. Besides the obvious advantage of being more tractable for calculations, simplified models can provide a more transparent picture of the basic mechanisms and usually involve a relatively small number of input parameters [36]. It is commonly, but not universally, believed that the main mechanisms can be understood within band models, which is supported by the success of these models in explaining several phenomena including magnetism [24, 49, 50], nematicity [37, 52], unconventional superconductivity [26, 27, 36], and transport [17–19, 53, 54].

Figure 1.2(b) schematically shows the evolution of the FSs of a common band model through the different phases of iron pnictides. The Brillouin zone in this model is “unfolded” and corresponds to the single-iron unit cell, which is a simplification of the real two-iron Brillouin zone shown in Fig. 1.1. The unfolding procedure, which can be performed in two ways [56, 57], invokes a simplification of the weak hybridization of iron and pnictogen orbitals. The effective two-dimensional band-model mimics those parts of the three-dimensional FSs that are strongly interacting and are thus more relevant for the excitonic instability than other parts of the FSs [56]. As summarized in the supplemental material of Ref. [58], the main features of the FS topology are reproduced by band models similar to the one shown in Fig. 1.2(b). A natural property of such models is the ellipticity of the electron pockets, which has been shown to be necessary to explain certain effects, e.g., in the magnetic response [49, 50, 59] and in transport [19, 53].

The spin fluctuations in iron pnictides [60–62] are believed to form the pairing glue for superconductivity [26, 36, 55] and perhaps to drive the structural transition [2, 33, 37, 52]. The precise mechanisms are the subject of current research, for which transport investigations can provide valuable insights. Figure 1.2(b) also indicates the scattering due to spin fluctuations in the different phases. In the paramagnetic phase, electrons scatter predominantly with momen-

tum changes close to \mathbf{Q}_X and \mathbf{Q}_Y , due to the peaked spin-fluctuation spectrum at this wavevectors. This leads to enhanced interpocket scattering. In the nematic phase, the broken symmetry of the spin-fluctuation peaks at \mathbf{Q}_X and \mathbf{Q}_Y gives rise to strongly anisotropic transport behavior. Finally, in the SDW phase, spin fluctuations, which in this phase include the damped magnon mode, give rise to strong intrapocket scattering between different sides of the reconstructed pockets.

1.3 Outline

In chapter 2 I will introduce the general theoretical framework for the study of the linear-response transport with scattering due to collective excitations. Some simplifications and their physical meaning will be discussed, which make the complex transport description applicable for investigations in the following chapters. In the same chapter, I will also calculate the general connection between the conductivity of a single crystal and the conductivity of a “twinned” crystal consisting of domains rotated by 90° with respect to each other. This will be useful for considering transport of twinned and detwinned 122 pnictides in chapter 6.

In chapter 3, I will consider a generic excitonic model with two concentric FSs and anisotropic scattering [17], relevant for materials such as chromium and its alloys [63, 64], transition-metal dichalcogenides [65], electron-hole bilayers [66], and iron pnictides [26, 51, 67]. The simplicity of this model will allow for an exact analytical solution of the transport problem, even in case of strongly anisotropic scattering. We will see that anisotropic scattering can cause some fraction of carriers to drift in the “wrong” direction, i.e., such as producing a negative contribution to the total charge current—an effect which can explain the unusually small magnetoresistance in combination of an enhanced Hall coefficient, measured in iron pnictides.

Chapters 4–6 are devoted to study more advanced band model, which is relevant for the paramagnetic, nematic, and SDW phases of iron pnictides, respectively. An overview over the FS topology in the different phases is given in Fig. 1.2(b). An exact analytical solution of the transport problem within this model is impossible. In chapter 4 I will therefore discuss the transport problem both numerically and analytically using some approximations. The analytical considerations will be especially useful to understand some intriguing phenomena such as the nearly equal conductivity contribution of all states on the FS, which is unusual since some states have significantly reduced lifetimes. In chapter 5 I will show that this

peculiarity can explain the characteristic behavior of the resistive anisotropy in the nematic phase. Probably the most exotic transport effects will be discussed in chapter 6. Here, we will find a thermodynamic instability of the magnetically ordered system in an external magnetic field, which is due to the scattering of electrons off damped magnons. I will conclude in chapter 7.

2 Transport theory

In this chapter I will discuss some methods for theoretical investigations of transport. First, I will briefly review the non-equilibrium Green's function approach, which will lead us to the kinetic equation. Afterwards I will consider scattering due to collective excitations and I will derive the corresponding Boltzmann equation, also called Bethe-Salpeter equation in the Kubo formalism, which will be the starting point for the calculations in subsequent chapters. I will then briefly sketch the basics of the Kubo approach. The Kubo formalism will be useful to discuss the importance of umklapp processes if we consider scattering due to collective excitations. In the last part of this chapter I will derive a relation between the conductivity of a single crystal with anisotropic conductivity and the corresponding twinned crystal that consists of domains rotated by 90° with respect to each other. The existence of an exact relation is specific for two-dimensional systems. It will become very useful for the investigations of the resistivity in the SDW phase of the iron pnictides.

2.1 Non-equilibrium Green's function approach

The advantage of the non-equilibrium approach over the Kubo formalism in determining the linear-response transport behavior is that within the former the transport can be described with *single-particle* Green's functions, e.g., simply as the expectation value of the current operator. On the other hand, within the Kubo formalism, transport is related to the correlation of two particles and is thus determined by *two-particle* Green's functions. For the purpose of considering semiclassical transport effects in the presence of an external magnetic field, the non-equilibrium approach [10] is more convenient than the Kubo formalism, as the diagrammatic consideration of vertex corrections in the latter is very complicated [68, 69].

In the following, I will present the basic idea of the non-equilibrium approach. The Green's functions are usually considered in the so-called Wigner or mixed

representation, in which the time and spatial coordinates are split into relative and center-of-mass coordinates. Fourier transforming the relative coordinates, the arguments of the Green's functions become $(\mathbf{k}, \omega; \mathbf{r}, t)$. In the following the center-of-mass coordinates \mathbf{r}, t will be suppressed for clarity.

Based on Fermi-liquid theory, one can assume that the spectral function of the electrons has well-defined peaks around some quasi-particle energies $\varepsilon_{\mathbf{k}}$. For the investigations of the semiclassical transport effects, one can go even further and assume that the spectral functions are narrow, i.e., $A(\mathbf{k}, \omega) \approx 2\pi\delta(\varepsilon_{\mathbf{k}} - \omega)$. This is referred to as the *quasiparticle approximation* [9, 10]. The “lesser” and “greater” Green's functions can be written as

$$G^<(\mathbf{k}, \omega) = A(\mathbf{k}, \omega)f_{\mathbf{k}} \quad \text{and} \quad G^>(\mathbf{k}, \omega) = A(\mathbf{k}, \omega)(1 - f_{\mathbf{k}}), \quad (2.1)$$

respectively. The lesser Green's function determines the expectation value of the total charge current

$$\mathbf{J} = e \sum_{\mathbf{k}} \mathbf{v}_{\mathbf{k}} f_{\mathbf{k}}, \quad (2.2)$$

where the velocity is given by $\mathbf{v}_{\mathbf{k}} \equiv \hbar\nabla_{\mathbf{k}}\varepsilon_{\mathbf{k}}$. $f_{\mathbf{k}}$ can be interpreted as the momentum distribution function, which in equilibrium reduces to the Fermi distribution,

$$f_{\mathbf{k}} \xrightarrow{\text{equil.}} n_F(\varepsilon_{\mathbf{k}}) = \frac{1}{e^{\varepsilon_{\mathbf{k}}/k_B T} + 1}, \quad (2.3)$$

where k_B is the Boltzmann constant, T is the temperature, and the Fermi energy is set to zero.

We consider electrons exposed to the spatially homogeneous external force

$$\mathbf{F} = e\mathbf{E} + \frac{e}{\hbar} \mathbf{v}_{\mathbf{k}} \times \mathbf{B} - \frac{\varepsilon_{\mathbf{k}}}{T} \nabla T, \quad (2.4)$$

which is due to the Lorentz force for electric and magnetic fields, \mathbf{E} and \mathbf{B} , respectively, and a spatial temperature gradient ∇T . In the linear-response regime the fields and the temperature gradient are assumed to be small. The equations of motion for the lesser and greater Green's functions can therefore be simplified by means of the gradient expansion [70]. Applying also the quasiparticle approximation, we arrive at the so-called kinetic equation [9, 10, 70]

$$\mathbf{F} \cdot \nabla_{\mathbf{k}} f_{\mathbf{k}} = (1 - f_{\mathbf{k}})\Sigma^<(\mathbf{k}, \varepsilon_{\mathbf{k}}) - f_{\mathbf{k}}\Sigma^>(\mathbf{k}, \varepsilon_{\mathbf{k}}), \quad (2.5)$$

where $\Sigma^<$ and $\Sigma^>$ are self-energies, which depend on the details of the interactions

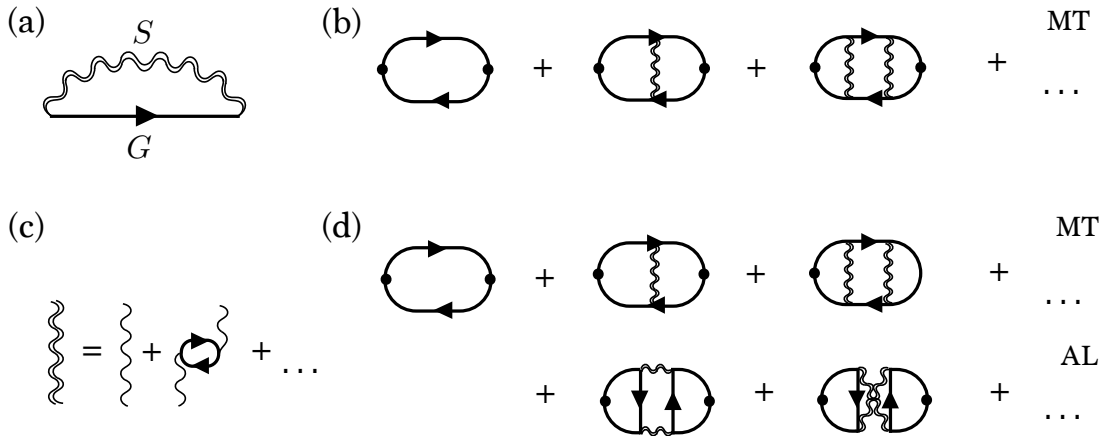


Figure 2.1: (a) Self-energy diagram with an electron propagator G and a bosonic propagator S representing a collective excitation. (b) Diagrams to be considered according to the Ward identity for the conductivity within the Kubo approach if the bosonic propagator in (a) does not contain electron propagators. The first term is called Drude term and the following terms are Maki-Thompson (MT) type ladder diagrams. (c) Schematic picture of a bosonic propagator which contains electron propagators. (d) Conductivity diagrams for the bosonic propagator of type (c). In addition to the MT diagrams Aslamazov-Larkin- (AL-) type diagrams appear.

between the electrons. The solution of the kinetic equation determines the non-equilibrium distribution function $f_{\mathbf{k}}$ and consequently the transport behavior. The kinetic equation is also called the *quantum Boltzmann equation* [8] because it has the form of the semiclassical Boltzmann equation but is derived within quantum mechanics. The left-hand side can be interpreted as the change of the distribution due to the force and the right-hand side as the change due to scattering. The self-energies $\Sigma^<(\mathbf{k}, \varepsilon_{\mathbf{k}})$ and $\Sigma^>(\mathbf{k}, \varepsilon_{\mathbf{k}})$ can be interpreted as the scattering rates for scattering into and out of state \mathbf{k} , respectively [70]. In general they depend on the non-equilibrium distribution $f_{\mathbf{k}}$.

2.2 Scattering due to collective excitations

We want to consider scattering of electrons due to bosonic collective excitations [71] and consider the self-energy diagram depicted in Fig. 2.1(a). The bosonic

propagators can be written as

$$S^{<}(\mathbf{k}, \omega) = B(\mathbf{k}, \omega) n(\omega) \quad \text{and} \quad S^{>}(\mathbf{k}, \omega) = B(\mathbf{k}, \omega) (1 + n(\omega)), \quad (2.6)$$

where $B(\mathbf{k}, \omega)$ is the spectral function of the bosons and $n(\omega)$ is the Bose-Einstein distribution function. Note that in Eq. (2.6) we assumed that in contrast to the electrons, the bosons are in equilibrium. If we specifically assume the bosons to describe collective excitations of the electrons themselves, which are not in equilibrium, then this assumption requires justification—this will be discussed in the next section. The self-energies entering Eq. (2.5) read

$$\Sigma^{>(<)}(\mathbf{k}, \varepsilon_{\mathbf{k}}) = g^2 \sum_{\mathbf{q}} \int \frac{d\omega}{2\pi} G^{>(<)}(\mathbf{k} - \mathbf{q}, \varepsilon_{\mathbf{k}} + \omega) S^{>(<)}(\mathbf{q}, \omega), \quad (2.7)$$

where g is the electron-boson coupling constant.

We now set $\mathbf{B} = 0$ and consider the case $\mathbf{B} \neq 0$ in a separate section 2.4. To linearize Eq. (2.5) with respect to the (weak) force \mathbf{F} , we make the most general ansatz

$$f_{\mathbf{k}} = n_F(\varepsilon_{\mathbf{k}}) - n'_F(\varepsilon_{\mathbf{k}}) \mathbf{F} \cdot \mathbf{\Lambda}_{\mathbf{k}}, \quad (2.8)$$

where $n'_F(\varepsilon_{\mathbf{k}}) = dn_F(\varepsilon_{\mathbf{k}})/d\varepsilon_{\mathbf{k}}$. $\mathbf{\Lambda}_{\mathbf{k}}$ is independent of \mathbf{F} and in the semiclassical picture can be seen as the *mean free path* (MFP) of the electron in state \mathbf{k} , according to the following explanation: Consider a classical particle in the weak force field \mathbf{F} . The energy of the particle traversing the path $\mathbf{\Lambda}_{\mathbf{k}}$ changes by $\mathbf{\Lambda}_{\mathbf{k}} \cdot \mathbf{F}$. Hence, the occupation of the state \mathbf{k} changes by $-n'_F(\varepsilon_{\mathbf{k}}) \mathbf{F} \cdot \mathbf{\Lambda}_{\mathbf{k}}$ in agreement with Eq. (2.8).

We insert Eqs. (2.1), (2.7), and (2.8) into Eq. (2.5) and make use of the quasi-particle approximation. Neglecting higher orders in \mathbf{F} , we obtain for a state \mathbf{k} at the Fermi level, i.e., for $\varepsilon_{\mathbf{k}} = 0$,

$$\mathbf{\Lambda}_{\mathbf{k}} = \tau_{\mathbf{k}} \mathbf{v}_{\mathbf{k}} + \tau_{\mathbf{k}} \sum_{\mathbf{q}} W_{\mathbf{k}}^{\mathbf{k}+\mathbf{q}} \mathbf{\Lambda}_{\mathbf{k}+\mathbf{q}}, \quad (2.9)$$

where

$$\tau_{\mathbf{k}} = \left(\sum_{\mathbf{q}} W_{\mathbf{k}}^{\mathbf{k}+\mathbf{q}} \right)^{-1}, \quad (2.10)$$

$$W_{\mathbf{k}}^{\mathbf{k}+\mathbf{q}} \equiv p_T(\varepsilon_{\mathbf{k}+\mathbf{q}}) \frac{g^2 B(\mathbf{q}, \varepsilon_{\mathbf{k}+\mathbf{q}})}{\varepsilon_{\mathbf{k}+\mathbf{q}}}, \quad (2.11)$$

$$p_T(x) \equiv x \left(\coth \frac{x}{2k_B T} - \tanh \frac{x}{2k_B T} \right). \quad (2.12)$$

In Eqs. (2.9) and (2.10), $\tau_{\mathbf{k}}$ can be identified as the quasiparticle lifetime, determined by the retarded self-energy, $\tau_{\mathbf{k}} \equiv (2 \text{Im} \Sigma^R(\mathbf{k}, \varepsilon_{\mathbf{k}}))^{-1}$. Equation (2.10) can be derived by explicitly calculating the retarded part of the self-energy in Fig. 2.1(a). $W_{\mathbf{k}}^{\mathbf{k}+\mathbf{q}}$ can be interpreted as the scattering rate from state \mathbf{k} to state $\mathbf{k} + \mathbf{q}$.

Assuming inversion symmetry so that $\varepsilon_{\mathbf{k}} = \varepsilon_{-\mathbf{k}}$, $\mathbf{v}_{\mathbf{k}} = -\mathbf{v}_{-\mathbf{k}}$, and $B(\mathbf{q}, \omega) = B(-\mathbf{q}, \omega)$ we find that $\Lambda_{\mathbf{k}} = -\Lambda_{-\mathbf{k}}$, which ensures particle conservation,

$$\sum_{\mathbf{k}} f_{\mathbf{k}} = \sum_{\mathbf{k}} n_F(\varepsilon_{\mathbf{k}}), \quad (2.13)$$

as can be seen by summing both sides of Eq. (2.8).

Equation (2.9) will form the starting point for considering transport in specific models in the next chapters. It will be referred to as the *Boltzmann equation*. In the next section, we will see that it can be derived within the Kubo approach, where it is called the *Bethe-Salpeter equation* [13]. The second term on the right-hand side of Eq. (2.9) averages to zero if the scattering rate is isotropic, i.e., if it does not depend on \mathbf{q} . In the case of anisotropic scattering, however, the corrections due to the second term become important. These corrections are called *forward-scattering* or *backscattering corrections* depending on whether small- or large-angle scattering processes are dominant. To refer to these corrections in general without specifying the explicit form of the scattering I will use the term *forward-scattering corrections* in the following.

2.3 Collective excitations and umklapp scattering

In this section I will briefly review the Kubo approach. This will be useful to discuss the justification for assuming the collective excitations to be in equilibrium, mentioned in the previous section. Within the Kubo formalism, Eq. (2.9) can be

obtained starting from the self-energy

$$\Sigma(\mathbf{k}, i\nu_n) = k_B T g^2 \sum_{\mathbf{q}, i\omega_n} G(\mathbf{k} - \mathbf{q}, i\nu_n - i\omega_n) S(\mathbf{q}, i\omega_n), \quad (2.14)$$

where ν_n (ω_n) represents a fermionic (bosonic) Matsubara frequency, and G and S respectively denote the electron and boson propagators. The calculation of the conductivity then requires the consideration of Feynman diagrams with two fermionic propagators. Neglecting quantum corrections, one has to sum all ladder diagrams, shown schematically in Fig. 2.1(b). Taking only the first term in the sum, called the Drude term, one obtains $\Lambda_{\mathbf{k}} = \tau_{\mathbf{k}} \mathbf{v}_{\mathbf{k}}$ instead of Eq. (2.9). This will be referred to as the *Drude approximation*,

$$\Lambda_{\mathbf{k}}^D = \tau_{\mathbf{k}} \mathbf{v}_{\mathbf{k}} \quad (2.15)$$

(in the modern literature the term *relaxation-time approximation* is also used frequently). The corrections to the Drude approximation in Eq. (2.9) are obtained in the Kubo formalism by summing up the whole series of ladder diagrams in Fig. 2.1(b). These are the so-called vertex corrections, which are related to the forward-scattering corrections in the Boltzmann approach. The vertex corrections in Fig. 2.1(b) are of Maki-Thompson (MT) type, and they give rise to the second term on the right-hand side of Eq. (2.9).

Particle conservation requires that the vertex corrections satisfy a Ward identity [13]. The Ward identity can be written as a functional derivative,

$$V(\mathbf{k}, \mathbf{k}', i\nu_n, i\nu'_n) \propto \frac{\delta \Sigma(\mathbf{k}, i\nu_n)}{\delta G(\mathbf{k}', i\nu'_n)}, \quad (2.16)$$

where $V(\mathbf{k}, \mathbf{k}', i\nu_n, i\nu'_n)$ is the four-point vertex connecting the upper and lower fermion lines in Fig. 2.1(b). Since the self-energy considered in Eq. (2.14) contains only one electron propagator, there is only one vertex and the diagrams considered in Fig. 2.1(b) are complete.

Let us now consider what happens if the bosonic propagator S in Eq. (2.14) describes collective fluctuations of electrons and thus contains electron propagators as shown schematically in Fig. 2.1(c). According to the Ward identity, Eq. (2.16), the vertex function has additional terms due to the additional electron propagators in the self-energy. The additional terms give rise to additional series of diagrams for the conductivity, which are shown schematically in Fig. 2.1(d). These diagrams

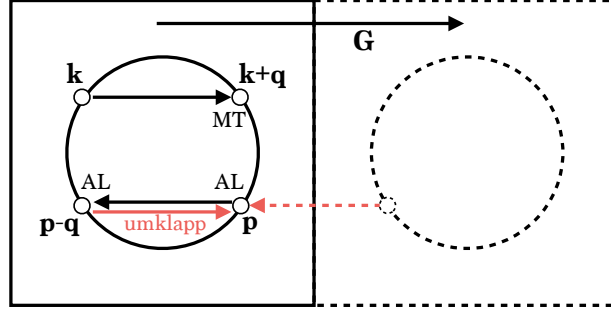


Figure 2.2: Scattering of an electron from \mathbf{k} to $\mathbf{k} + \mathbf{q}$ with $\mathbf{q} \approx \mathbf{G}/2$. The solid square is the Brillouin zone with a FS (circle) and the reciprocal lattice vector \mathbf{G} . The contribution of the final state $\mathbf{k} + \mathbf{q}$ to the MFP is accounted for by the MT vertex corrections. If the scattering is because of electron-electron interaction, momentum conservation requires another electron to scatter either from \mathbf{p} to $\mathbf{p} - \mathbf{q}$ or, since $\mathbf{q} \approx \mathbf{G}/2$, from $\mathbf{p} - \mathbf{q}$ to \mathbf{p} because of umklapp. The normal and the umklapp AL terms representing the second electron nearly cancel.

are of Aslamazov-Larkin (AL) type and in general produce additional terms in the Boltzmann equation (2.9).

Let us compare this to the non-equilibrium formalism from which we derived Eq. (2.9) via the assumption that the collective excitations are in equilibrium and thus do not contribute to transport. Evidently, within the Kubo formalism, the contribution of the collective fluctuations is represented by AL diagrams. I will now explain the physical meaning of neglecting them. It is useful to consider the relaxation of a non-equilibrium system towards the equilibrium state. The MFP $\Lambda_{\mathbf{k}}$ can be seen as the mean path an electron in state \mathbf{k} traverses during the relaxation. If the relaxation time is equal to the quasiparticle lifetime $\tau_{\mathbf{k}}$, the MFP obviously reads $\tau_{\mathbf{k}}\mathbf{v}_{\mathbf{k}}$, the first term in Eq. (2.9), since during the time $\tau_{\mathbf{k}}$ the electron does not scatter to any other state and its velocity is $\mathbf{v}_{\mathbf{k}}$. However, the relaxation time is in general larger than the quasiparticle lifetime, since if scattering is anisotropic, more than one scattering event is necessary to lose the memory of the initial velocity. In this case corrections to the MFP $\tau_{\mathbf{k}}\mathbf{v}_{\mathbf{k}}$ must be taken into account because during the relaxation process the electron scatters to different states with velocity distinct from $\mathbf{v}_{\mathbf{k}}$.

As shown in Fig. 2.2 the MT vertex corrections correspond to the contribution to the MFP from the states $\mathbf{k} + \mathbf{q}$, the states to which the considered electron scatters. If the scattering of the electron is due to electron-electron interactions,

then the considered electron has a scattering partner—an electron in state \mathbf{p} . Momentum conservation requires that the scattering partner scatters from \mathbf{p} to $\mathbf{p} - \mathbf{q}$ if umklapp processes are neglected. The contribution to the MFP from the scattering partner is represented by the AL diagrams. The electron-electron scattering is the elementary process if the scattering of the initial electron proceeds via the excitation of a collective mode. The scattering partner of the initial electron can be considered as part of the collective excitation. Thus the AL terms represent the contribution of the collective excitation to transport.

However, it turns out that neglecting AL diagrams and thus assuming collective excitations not to contribute to transport is a valid approximation in certain cases. The AL terms have been considered by Kontani *et al.* [13, 72] for the case of scattering due to spin fluctuations in a model for cuprates. They show that due to enhanced scattering with momentum change $\mathbf{q} \approx \mathbf{G}/2$, where \mathbf{G} is a reciprocal lattice vector, the AL terms are suppressed due to *umklapp scattering* such that the AL terms become negligible in comparison to the MT terms. Figure 2.2 illustrates the physics behind this result. If the momentum exchange is approximately $\mathbf{q} \approx \mathbf{G}/2$, umklapp allows the scattering partner to scatter from $\mathbf{p} - \mathbf{q}$ to \mathbf{p} , which is obtained from the usual process by time reversal. If the electron-electron interaction is short ranged then both the usual and the umklapp processes have the same probability. On average their contributions to the MFP cancel out.

Based on the results of Kontani *et al.* [13, 72] we will neglect AL terms in the following. This is mainly motivated by the fact that the physical reasons leading to the suppression of AL terms can be applied to all real systems for which our calculations are relevant.

2.4 Transport in the presence of a magnetic field

The magnetic field alone does not bring the system out of equilibrium: It can be verified that the ansatz $f_{\mathbf{k}} = n_F(\varepsilon_{\mathbf{k}})$ is a solution of the kinetic equation (2.5) in this case. The deviation from equilibrium is therefore controlled by the force $\mathbf{F}|_{B=0}$. Hence, the standard ansatz for the non-equilibrium distribution in the presence of a magnetic field reads [73]

$$f_{\mathbf{k}} = n_F(\varepsilon_{\mathbf{k}}) - n'_F(\varepsilon_{\mathbf{k}}) \mathbf{F}|_{B=0} \cdot \mathbf{\Lambda}_{\mathbf{k}}, \quad (2.17)$$

2 Transport theory

cf. Eq. (2.8), with

$$\Lambda_{\mathbf{k}} = \Lambda_{\mathbf{k}}^{(0)} + \Lambda_{\mathbf{k}}^{(1)} + \dots, \quad (2.18)$$

where $\Lambda_{\mathbf{k}}^{(n)}$ is of order n in \mathbf{B} . Inserting this ansatz into Eq. (2.5), proceeding in analogy to the $\mathbf{B} = 0$ case, and separating the different orders in \mathbf{B} , we obtain the set of equations

$$\Lambda_{\mathbf{k}}^{(0)} = \tau_{\mathbf{k}} \mathbf{v}_{\mathbf{k}} + \tau_{\mathbf{k}} \sum_{\mathbf{q}} W_{\mathbf{k}}^{\mathbf{k}+\mathbf{q}} \Lambda_{\mathbf{k}+\mathbf{q}}^{(0)}, \quad (2.19)$$

$$\Lambda_{\mathbf{k}}^{(n+1)} = \tau_{\mathbf{k}} \frac{e}{\hbar} [\mathbf{B} \cdot (\mathbf{v}_{\mathbf{k}} \times \nabla_{\mathbf{k}})] \Lambda_{\mathbf{k}}^{(n)} + \tau_{\mathbf{k}} \sum_{\mathbf{q}} W_{\mathbf{k}}^{\mathbf{k}+\mathbf{q}} \Lambda_{\mathbf{k}+\mathbf{q}}^{(n+1)} \quad \text{for } n \geq 0. \quad (2.20)$$

For later use, we now consider a two-dimensional system in the xy -plane and the magnetic field pointing in the z -direction, $\mathbf{B} = B\mathbf{z}$. The FS now becomes a Fermi line. Considering \mathbf{k} on the Fermi line and parametrizing the Fermi line by some parameter θ , the operator acting on $\Lambda_{\mathbf{k}}^{(n)}$ in Eq. (2.20) can be written as

$$\frac{e}{\hbar} [\mathbf{B} \cdot (\mathbf{v}_{\mathbf{k}} \times \nabla_{\mathbf{k}})] = \omega_{\theta} \partial_{\theta}, \quad (2.21)$$

with the cyclotron frequency

$$\omega_{\theta} = \eta \frac{eB}{\hbar} \frac{|\mathbf{v}_{\theta}|}{|d\mathbf{k}_{\theta}/d\theta|}, \quad (2.22)$$

where $\eta = \text{sgn}(\mathbf{v}_{\theta} \cdot \mathbf{k}_{\theta})$.

Within the Drude approximation $\Lambda_{\theta}^{(0)} \approx \Lambda_{\theta}^{D(0)} \equiv \tau_{\theta} \mathbf{v}_{\theta}$. Summing up all $\Lambda^{D(n)}$ given in Eqs. (2.19) and (2.20) results in a differential equation for the Drude MFP in a magnetic field,

$$\Lambda_{\theta}^D = \tau_{\theta} \mathbf{v}_{\theta} + \tau_{\theta} \omega_{\theta} \partial_{\theta} \Lambda_{\theta}^D. \quad (2.23)$$

We can understand this equation if we consider electrons as classical particles. Let the velocity of the electrons be $\mathbf{v}(t) = v(\cos \phi(t), \sin \phi(t))$ and the Lorentz force acting on them $(eB/\hbar) \mathbf{z} \times \mathbf{v}(t)$. The classical equation of motion reads

$$\frac{d}{dt} \mathbf{v}(t) = \frac{eB}{\hbar m} \mathbf{z} \times \mathbf{v}(t) \equiv \omega \mathbf{z} \times \mathbf{v}(t) \quad (2.24)$$

and describes the orbital motion of the electrons. If we now assume a finite lifetime of the electrons so that the number of electrons decays with $\exp(-t/\tau)$, the average velocity of the electrons reads $\langle \mathbf{v} \rangle = \int dt/\tau \exp(-t/\tau) \mathbf{v}(t)$. Applying

$\int dt/\tau \exp(-t/\tau)[\dots]$ on both sides of Eq. (2.24) and noting that $\mathbf{z} \times \mathbf{v} = \partial_\phi \mathbf{v}$ we find

$$\langle \mathbf{v} \rangle = \mathbf{v}(0) + \tau \omega \partial_\phi \langle \mathbf{v} \rangle. \quad (2.25)$$

Equation (2.25) has the same form as Eq. (2.23) and one can thus interpret Eq. (2.23) as describing the effect of the orbital motion of the electrons in the magnetic field on the MFP. Note, however, that free electrons are rotated by a polar angle ϕ , whereas the electrons on a lattice move along the Fermi line (parametrized by θ). This is because on the lattice the velocity is perpendicular to the Fermi line and the Lorentz force changes the momentum of the electrons according to $\hbar d\mathbf{k}/dt = (eB/\hbar) \mathbf{z} \times \mathbf{v}_{\mathbf{k}}$.

2.5 Conductivity of single crystals and twinned crystals

The conductivity tensor σ relates the total charge current \mathbf{J} defined in Eq. (2.2) and the electric field \mathbf{E} [74],

$$\mathbf{J} = \sigma \mathbf{E}. \quad (2.26)$$

Inserting the ansatz (2.17) into Eq. (2.7) we find

$$\sigma^{ij} = e^2 \sum_{\mathbf{k}} [-n'_F(\varepsilon_{\mathbf{k}})] v_{\mathbf{k}}^i \Lambda_{\mathbf{k}}^j. \quad (2.27)$$

In the continuum limit, the sum over \mathbf{k} goes over into an integral over the d -dimensional \mathbf{k} -space. Changing the integration variables we can write

$$\sum_{\mathbf{k}} [\dots] \rightarrow \int d\varepsilon \int_{\varepsilon} dS \frac{1}{|\mathbf{v}_{\mathbf{k}}|} \left| \frac{d\mathbf{k}}{dS} \right| [\dots] = \int d\varepsilon \langle N_{\mathbf{k}}[\dots] \rangle_{\varepsilon}, \quad (2.28)$$

where $\langle [\dots] \rangle_{\varepsilon} = \int_{\varepsilon} dS [\dots] / \int_{\varepsilon} dS$ is the average over the constant-energy surface and

$$N_{\mathbf{k}} \equiv \frac{1}{|\mathbf{v}_{\mathbf{k}}|} \left| \frac{d\mathbf{k}}{dS} \right| \int_{\varepsilon} dS \quad (2.29)$$

is the momentum-resolved density of states. The derivative of the Fermi distribution has a peak at the Fermi level, $\varepsilon_{\mathbf{k}} = 0$, with a width of order $k_B T$. Assuming that the velocity and the MFP are nearly constant in the range $k_B T$ around the Fermi level, we can perform the energy integral on the right-hand side of Eq.

(2.27), leading to

$$\sigma^{ij} = e^2 \langle N_{\mathbf{k}} v_{\mathbf{k}}^i \Lambda_{\mathbf{k}}^j \rangle_{\text{FS}}, \quad (2.30)$$

where $\langle [\dots] \rangle_{\text{FS}} = \langle [\dots] \rangle_{\varepsilon=0}$ denotes the average over the FS.

In the chapters 5 and 6 we will consider the conductivity of iron pnictides in the nematic and the SDW phase. In these phases the crystal symmetry is orthorhombic such that the orthogonal crystallographic in-plane (xy -plane) directions a_{O} and b_{O} are not equivalent, in contrast to the equivalent directions a_{T} and b_{T} in the tetragonal phase. The inequivalence of the directions a_{O} and b_{O} is reflected in the *anisotropic* in-plane conductivity of single crystals. However, the transition from the tetragonal to the orthorhombic phase leads to the formation of structural twin domains as shown in Fig. 2.3 [75]. The domains are rotated by 90° with respect to each other in the xy -plane, and extend through the whole thickness of the crystal in the z -direction. The twinned crystal as a whole restores the C_4 symmetry in the xy -plane such that the in-plane conductivity of twinned crystals is *isotropic*. To measure the in-plane anisotropy of transport the crystals have to be detwinned, usually by applying uniaxial pressure [2].

In the following I will calculate the in-plane conductivity of the twinned crystal in terms of the in-plane conductivity of the single crystal,

$$\sigma = \begin{pmatrix} \sigma^{xx} & \sigma^{xy} \\ \sigma^{yx} & \sigma^{yy} \end{pmatrix}, \quad (2.31)$$

with arbitrary σ^{ij} . This is a non-trivial and, in general, analytically not even feasible task [76]. For two-dimensional polycrystals, however, there exists an *exact* relation between the conductivity of the polycrystals and the corresponding single crystal [77], which goes back to the works of Dykhne [78, 79]. Dykhne realized that in 2D there exists a symmetry transformation, which does not change the macroscopic properties of the polycrystal if the directions of the crystallites are equally distributed. Proceeding analogously as in Refs. [78, 79], I will show that the relation also holds between the conductivity of twinned and detwinned iron pnictides shown in Fig. 2.3. Considering the material to be quasi-two-dimensional is a valid approximation due to relatively weak z -dispersion [34] and the extended domains in z -direction [75].

We consider a twinned two-dimensional crystal in external electric and magnetic fields. Let $\mathbf{e}(\mathbf{r})$ and $\mathbf{j}(\mathbf{r})$ be the local electric field and the local charge current, respectively. The total electric field $\mathbf{E} = \int dV \mathbf{e}(\mathbf{r})$ and the total current $\mathbf{J} =$

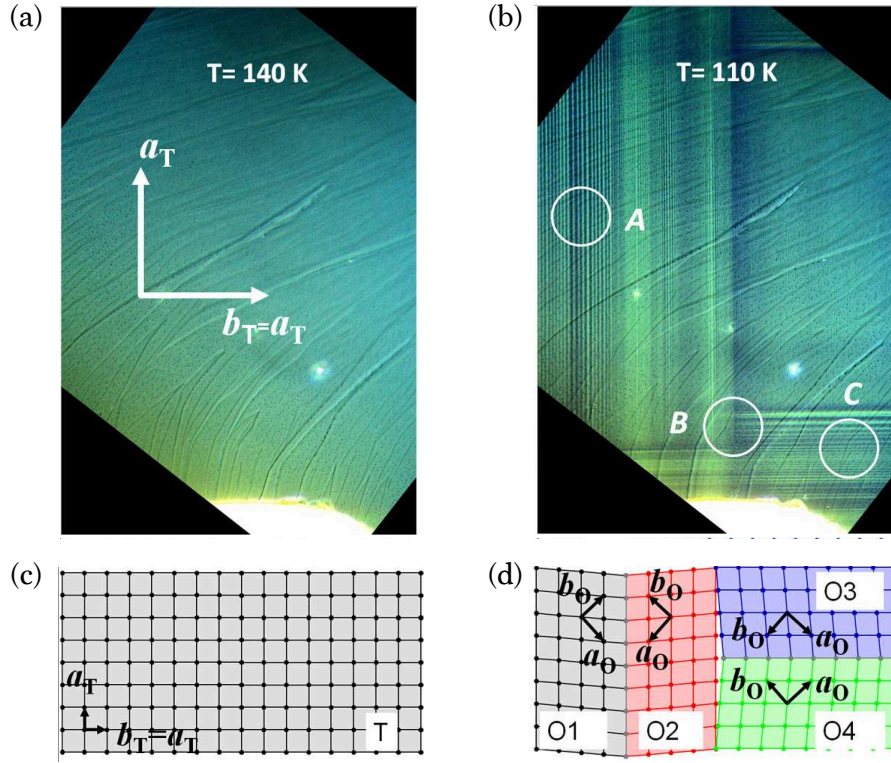


Figure 2.3: (a) Optical image of the xy -plane of a BaFe₂As₂ single crystal in the tetragonal phase. (b) Same as (a) but in the orthorhombic phase, in which a pattern of domain walls is formed. The typical domain width is about $10 \mu\text{m}$. In the z -direction the domains extend through the whole thickness of the crystal. (c) Schematic lattice structure in the tetragonal phase. (d) Four possible domain patterns (O1–O4) of the lattice structure in the orthorhombic phase. The domains O1 and O2 (O3 and O4) easily form pairs since they share a common plane. This results in the formation of lamellae visible in (b) as the thin vertical and horizontal lines: The spot A corresponds to the domains O1 and O2, C to the domains O3 and O4, and B to the crossed domains O1-O2 and O3-O4. From Ref. [75].

2 Transport theory

$\int dV \mathbf{j}(\mathbf{r})$ are obtained through integration over the crystal volume. \mathbf{E} and \mathbf{J} are related by Ohm's law

$$\mathbf{J} = \bar{\sigma} \mathbf{E}, \quad (2.32)$$

where the conductivity of the twinned crystal can be written as

$$\bar{\sigma} = \begin{pmatrix} \bar{\sigma}^{xx} & \bar{\sigma}^{xy} \\ -\bar{\sigma}^{xy} & \bar{\sigma}^{xx} \end{pmatrix} \quad (2.33)$$

since we assume the twinned crystal to be C_4 -symmetric. The local quantities fulfill the Ohm's law

$$\mathbf{j}(\mathbf{r}) = \sigma(\mathbf{r}) \mathbf{e}(\mathbf{r}), \quad (2.34)$$

where, depending on the domain, $\sigma(\mathbf{r})$ is either σ or $R\sigma R^{-1}$, where R is the 90° rotation matrix. \mathbf{j} and \mathbf{e} also fulfill the Maxwell equations

$$\nabla \cdot \mathbf{j} = 0 \quad \text{and} \quad \nabla \times \mathbf{e} = 0. \quad (2.35)$$

We introduce a transformation of the local quantities,

$$\mathbf{j}(\mathbf{r}) = \mathbf{j}'(\mathbf{r}) + a \det[\sigma(\mathbf{r})] R \mathbf{e}'(\mathbf{r}) \quad \text{and} \quad \mathbf{e}(\mathbf{r}) = a R \mathbf{j}'(\mathbf{r}), \quad (2.36)$$

where $a \equiv 1/[\sigma^{yx}(\mathbf{r}) - \sigma^{xy}(\mathbf{r})]$. Noting that a and $\det[\sigma(\mathbf{r})]$ are independent of \mathbf{r} , one can show that \mathbf{j}' and \mathbf{e}' fulfill Maxwell's equations (2.35) as well as Ohm's law (2.34) with the same conductivity tensor $\sigma(\mathbf{r})$. The total electric field $\mathbf{E}' = \int dV \mathbf{e}'(\mathbf{r})$ and the total current $\mathbf{J}' = \int dV \mathbf{j}'(\mathbf{r})$ should thus obey

$$\mathbf{J}' = \bar{\sigma} \mathbf{E}' \quad (2.37)$$

with the same conductivity tensor as in Eq. (2.32). On the other hand, integrating Eqs. (2.36) over the volume and using Eq. (2.32) leads to

$$\mathbf{J}' = -a \det(\sigma) (I - a \bar{\sigma} R)^{-1} R \mathbf{E}', \quad (2.38)$$

where I is the 2D identity matrix. Comparison of the Eqs. (2.37) and (2.38)

determines the conductivity of the twinned crystal. The real solutions read (i)

$$\bar{\sigma}^{xx} = \sqrt{\sigma^{xx} \sigma^{yy} - \left(\frac{\sigma^{yx} + \sigma^{xy}}{2}\right)^2}, \quad (2.39)$$

$$\bar{\sigma}^{xy} = \frac{\sigma^{xy} - \sigma^{yx}}{2} \quad (2.40)$$

for $\sigma^{xx} \sigma^{yy} > (\sigma^{yx} + \sigma^{xy})^2/4$ and (ii)

$$\bar{\sigma}^{xx} = 0, \quad (2.41)$$

$$\bar{\sigma}^{xy} = \frac{\sigma^{xy} - \sigma^{yx}}{2} + \sqrt{\left(\frac{\sigma^{yx} + \sigma^{xy}}{2}\right)^2 - \sigma^{xx} \sigma^{yy}} \quad (2.42)$$

for $\sigma^{xx} \sigma^{yy} < (\sigma^{yx} + \sigma^{xy})^2/4$. In the case (ii), the conductivity of a single domain is not positive semidefinite, since $\sigma^{xx} \sigma^{yy} \geq (\sigma^{yx} + \sigma^{xy})^2/4$ is the criterion for positive semidefiniteness of σ . The positive semidefiniteness of the conductivity tensor is required for the thermodynamic stability of the system [80]. The conductivity of the whole twinned crystal is positive semidefinite in both cases. In case (ii) it is purely transversal, giving rise to dissipationless conductance, similar as in a quantum Hall system. However, due to the instability of single domains it is unclear whether the solution (ii) has physical significance; further investigations are necessary.

3 Negative transport times due to anisotropic interband scattering

In this chapter I will apply the formalism introduced in the previous chapter to a specific two-band model with anisotropic scattering. We have seen that anisotropic scattering requires the consideration of forward-scattering corrections in Eq. (2.9), which in general makes it difficult to find an analytical solution. Here I will discuss a model in which an exact analytical solution is possible even for very strong scattering anisotropy. This allows the analytical study of some interesting effects resulting from the scattering anisotropy. Parts of this chapter have been published in Ref. [17].

3.1 Introduction

We consider a simple excitonic model with two FSs of circular (2D) or spherical (3D) shapes separated by \mathbf{Q} , which can be holelike or electronlike. The model is illustrated in Fig. 3.1(a). We assume that the scattering rate $W_{s\mathbf{k}}^{s'\mathbf{k}'}$ entering the Boltzmann equation (2.9) is due to elastic scattering and has an isotropic intraband contribution W_i and an anisotropic interband contribution $W_a(\theta)$ which is an even function of the scattering angle θ spanned by \mathbf{k} and \mathbf{k}' ,

$$W_{s,\mathbf{k}}^{s',\mathbf{k}'} = \delta(\varepsilon_{\mathbf{k}} - \varepsilon_{\mathbf{k}'}) (\delta_{s'\bar{s}} W_a(\theta) + \delta_{s's} W_i), \quad (3.1)$$

where $\bar{s} = 2$ (1) for $s = 1$ (2).

We will find that such anisotropic interband scattering can lead to negative transport times: Minority carriers may drift in the direction opposite of what one would expect based on their charge. Negative transport times of minority carriers were predicted for systems with electron- and holelike FSs [81], based on

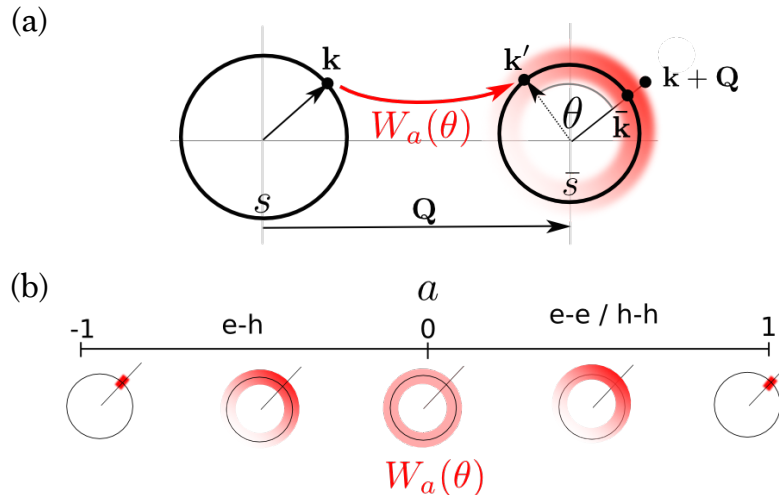


Figure 3.1: (a) Sketch of the two isotropic FSs s and \bar{s} , displaced by \mathbf{Q} , and the elastic interband scattering rate $W_a(\theta)$. (b) Illustration of the relation between the anisotropy parameter a and the shape of the function $W_a(\theta)$, for the case of $W_a(\theta)$ having a single peak at $\theta = 0$. In this case $a \in [-1, 0]$ corresponds to the electron-hole case (e-h) and $a \in [0, 1]$ corresponds to the electron-electron or hole-hole case (e-e/h-h). After Ref. [17].

strong electron-hole (*two-particle*) scattering. This *carrier drag* was first observed in semiconductor quantum wells [82]. It has not been appreciated that negative transport times can also arise due to anisotropic *single-particle* scattering in multiband systems.

Our model covers the special case of enhanced scattering for $\theta = 0$, which can be realized in materials close to an excitonic instability, e.g., electron-hole bilayers [66], iron pnictides [26, 51, 67], chromium and its alloys [63, 64], and the transition-metal dichalcogenides [65]. In these materials, nesting of electron and hole FSs strongly enhances interband spin or charge fluctuations with wavevectors close to the nesting vector. These fluctuations are expected to promote highly anisotropic scattering between the nested FSs.

In the iron pnictides, the effect of such scattering seems to be especially pronounced, as the normal-state transport coefficients show highly anomalous behavior. In particular, the unexpectedly small magnetoresistance is hard to reconcile with the strongly enhanced Hall coefficient if analyzed within a multiband model with isotropic scattering [3]. It is believed that this is due to anisotropic scattering due to spin fluctuations [45, 54, 83, 84], however, there are very few theoretical

investigations in this field. It has been shown that scattering off spin fluctuations could indeed explain the enhancement of the Hall coefficient [54], but the reduction of magnetoresistance remains puzzling.

In this chapter we will find that anisotropic scattering not only leads to an enhancement of the Hall coefficient [54], but also to a maximum at a characteristic anisotropy. At the same anisotropy the magnetoresistance shows a minimum with zero magnetoresistance, in agreement with the puzzling experimental observations [3]. We show that this anomaly can be explained by the occurrence of negative transport times.

3.2 Solution of the Boltzmann equation

According to the scattering rate given in Eq. (3.1) and the assumed rotational symmetry of the FSs, the model preserves rotational symmetry. Therefore, the Boltzmann equation (2.9) simplifies as the lifetime $\tau_{s\mathbf{k}}$ and the density of states $N_{s\mathbf{k}}$ do not depend on \mathbf{k} . From this one can also conclude that the MFP must be parallel to the only vector in Eq. (2.9), the velocity $\mathbf{v}_{s\mathbf{k}}$. The proportionality constant is independent of \mathbf{k} and is usually referred to as the transport or relaxation time τ_s^{tr} [74]. Inserting the ansatz $\mathbf{\Lambda}_{s\mathbf{k}} = \tau_s^{\text{tr}} \mathbf{v}_{s\mathbf{k}}$ and Eq. (3.1) into the Boltzmann equation (2.9) we find

$$\tau_s^{\text{tr}} \mathbf{v}_{s\mathbf{k}} = \tau_s \mathbf{v}_{s\mathbf{k}} + \tau_s \sum_{s'} \tau_{s'}^{\text{tr}} N_{s'} \langle [\delta_{s'\bar{s}} W_a(\theta) + \delta_{s's} W_i] \mathbf{v}_{s'\mathbf{k}'} \rangle_\theta, \quad (3.2)$$

where N_s is the density of states for FS s and the average over θ is denoted by $\langle \dots \rangle_\theta = \frac{1}{\pi} \int d\theta \dots$ for 2D and $\langle \dots \rangle_\theta = \frac{1}{2} \int d\theta \sin \theta \dots$ for 3D.

It is useful to rewrite the velocity in the integral in Eq. (3.2) as

$$\mathbf{v}_{s'\mathbf{k}'} = \mathbf{v}_{s'\bar{\mathbf{k}}} \cos \theta + v_{s'} \mathbf{e}_\perp \sin \theta, \quad (3.3)$$

where $v_s \equiv |\mathbf{v}_{s,\mathbf{k}}|$ is the Fermi velocity for FS s , \mathbf{e}_\perp denotes the unit vector perpendicular to $\mathbf{v}_{s,\mathbf{k}}$ in the plane spanned by $\mathbf{v}_{s,\mathbf{k}}$ and $\mathbf{v}_{s',\bar{\mathbf{k}}}$, and $\bar{\mathbf{k}}$ is the state on FS s' for which $\theta = 0$. Since $W_a(\theta)$ is an even function of θ , the term proportional to $\sin \theta$ averages to zero in the integral in Eq. (3.2). The cosine term averages to zero only in the term containing W_i . Altogether we arrive at

$$\tau_s^{\text{tr}} \mathbf{v}_{s\mathbf{k}} = \tau_s \mathbf{v}_{s\mathbf{k}} + \tau_s^{\text{tr}} \mathbf{v}_{s\bar{\mathbf{k}}} \tau_s N_s \langle W_a(\theta) \cos \theta \rangle_\theta. \quad (3.4)$$

Defining the scattering-anisotropy parameter

$$a_s^{\bar{s}} \equiv \eta \tau_s N_{\bar{s}} \langle W_a(\theta) \cos \theta \rangle_{\theta} = \eta \frac{N_{\bar{s}} \langle W_a(\theta) \cos \theta \rangle_{\theta}}{N_{\bar{s}} \langle W_a(\theta) \rangle_{\theta} + N_s W_i}, \quad (3.5)$$

where $\eta = \text{sgn}(\mathbf{v}_{s\mathbf{k}} \cdot \mathbf{v}_{\bar{s}\bar{\mathbf{k}}})$, we can solve Eq. (3.4) to obtain

$$\Lambda_{s\mathbf{k}} \equiv \tau_s^{\text{tr}} \mathbf{v}_{s\mathbf{k}} = \frac{\tau_s \mathbf{v}_{s\mathbf{k}} + \eta a_s^{\bar{s}} \tau_{\bar{s}} \mathbf{v}_{\bar{s}\bar{\mathbf{k}}}}{1 - a_s^{\bar{s}} a_{\bar{s}}^s}. \quad (3.6)$$

Note that the anisotropy parameter defined in Eq. (3.5) is confined to the range $[-1, 1]$. Many different realizations of $W_a(\theta)$ give the same anisotropy parameter, but for clarity we focus on the most relevant situation where $W_a(\theta)$ has a maximum at $\theta = 0$. In this case, the range $a \in [0, 1]$ corresponds to FSs of the same type (i.e. both electronlike or both holelike), whereas $a \in [-1, 0]$ corresponds to one electron and one hole FS as illustrated in Fig. 3.1(b). For both scenarios, $a = 0$ is the isotropic limit, $W_a(\theta) = \text{const}$, whereas $a = \pm 1$ are the strong-anisotropy limits, which can be achieved if the interband scattering dominates and is nearly a δ -function, i.e., $W_a(\theta) \approx W_a \delta(\theta)$ and $W_a \gg W_i$. In the electron-hole case, a peak at $\theta = 0$ naturally occurs close to an excitonic instability, due to the scattering by the enhanced spin or charge fluctuations, allowing $a \in [-1, 0]$ to be tuned by doping or temperature. Although there is no excitonic instability for the e-e/h-h case, collective fluctuations can still be enhanced due to the proximity of nesting.

3.3 Transport times

The transport time can easily be expressed in terms of the anisotropy parameters if we insert $\mathbf{v}_{\bar{s}\bar{\mathbf{k}}} = \eta v_{\bar{s}} \mathbf{v}_{s\mathbf{k}} / v_s$ into Eq. (3.6), leading to

$$\tau_s^{\text{tr}} = \tau_s \frac{1 + a_s^{\bar{s}} \gamma_{\bar{s}}}{1 - a_s^{\bar{s}} a_{\bar{s}}^s}, \quad (3.7)$$

where $\gamma_s = \tau_s v_s / (\tau_{\bar{s}} v_{\bar{s}})$ is the ratio between the Drude MFPs. For equal densities of states or if $\langle W_a(\theta) \rangle_{\theta} \gg W_i$, γ_s is the ratio of the FS areas. Equation (3.7) shows the relation between the lifetime and the transport time. $\tau_s^{\text{tr}} / \tau_s$ is plotted in Fig. 3.2(a), in which for simplicity the density of states on both FSs is set equal so that $a_s^{\bar{s}} = a_{\bar{s}}^s \equiv a$. We first consider the electron-hole case, $a \in [-1, 0]$. The carriers corresponding to the smaller FS area, which we will call minority carriers,

3 Negative transport times due to anisotropic interband scattering

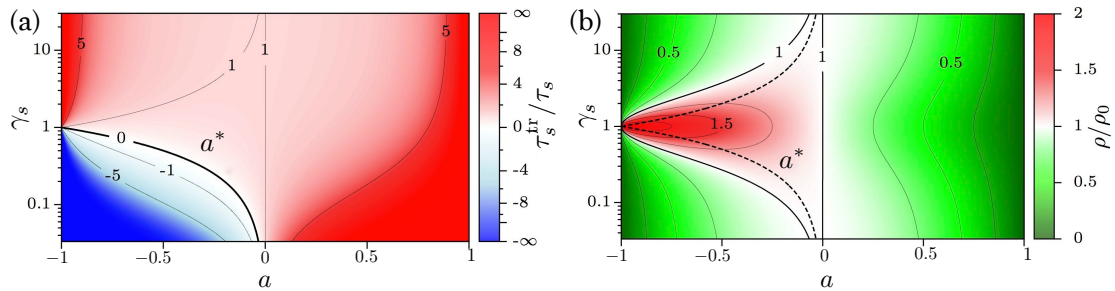


Figure 3.2: (a) Transport time τ_s^{tr} in units of the bare lifetime τ_s at FS s as a function of the anisotropy parameter a and the ratio of the FS areas, $\gamma_s = k_s^{d-1}/k_{\bar{s}}^{d-1}$. The corresponding plot of $\tau_s^{\text{tr}}/\tau_s$ would be the mirror image with respect to $\gamma_s = 1$. (b) Resistivity in terms of its isotropic limit, $\rho_0 \equiv \rho|_{a=0}$, as a function of a and γ_s . At $a = a^*$ (dashed), the transport time of the minority carriers changes sign and the resistivity has a maximum as a function of a . After Ref. [17].

have a negative transport time for

$$a < a^* \equiv -\min_s \gamma_s. \quad (3.8)$$

In the anisotropic limit, $a \rightarrow -1$, the transport times of minority (majority) carriers diverge to negative (positive) values, which can be understood as follows. For $a \rightarrow -1$, the scattering rate $W_a(\theta)$ becomes a δ -function and, therefore, an electron in the state $|s\mathbf{k}\rangle$ can only scatter to the state $|\bar{s}\bar{\mathbf{k}}\rangle$. Thus the system decouples into pairs of states, thereby becoming nonergodic. In general, the joint occupation of these two states in non-equilibrium $f_{s\mathbf{k}} + f_{\bar{s}\bar{\mathbf{k}}}$ will differ from that in equilibrium, $2n_F(\varepsilon_{\mathbf{k}})$. Scattering between the two states cannot relax the joint occupation and consequently the whole system cannot relax into equilibrium. This leads to the diverging transport times. The described mechanism is not applicable to the compensated case, $\gamma_s = 1$, for which $f_{s\mathbf{k}} + f_{\bar{s}\bar{\mathbf{k}}} = 2n_F(\varepsilon_{\mathbf{k}})$. I will refer to this case below.

For $a \approx -1$, the scattering between $|s\mathbf{k}\rangle$ and $|\bar{s}\bar{\mathbf{k}}\rangle$ still dominates and scattering to other states can be treated as a weak perturbation. This additional scattering leads to weak relaxation of $f_{s\mathbf{k}} + f_{\bar{s}\bar{\mathbf{k}}}$ and thus stabilizes a steady state. Still, the difference $f_{s\mathbf{k}} - f_{\bar{s}\bar{\mathbf{k}}}$ relaxes much more rapidly than $f_{s\mathbf{k}} + f_{\bar{s}\bar{\mathbf{k}}}$. Hence, in the steady state the former is much smaller in absolute value than the latter so that $f_{s\mathbf{k}} \approx f_{\bar{s}\bar{\mathbf{k}}}$. The occupation numbers on the same side of the two FSs are both either enhanced or reduced in comparison to the equilibrium state as illustrated in Fig. 3.3. In the electron-hole case, the electrons at these points have opposite

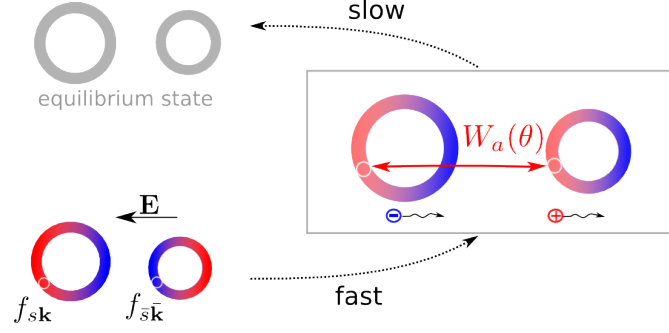


Figure 3.3: Illustration of the relaxation process in the case that the interband scattering is strongly enhanced for $\theta = 0$. The occupation of the FS states $|s\mathbf{k}\rangle$ and $|\bar{s}\bar{\mathbf{k}}\rangle$ is nearly equalized after a short time in comparison to the duration of the relaxation process. In the electron-hole case this leads to the drift of minority carriers in the “wrong” direction.

velocities so that the electrons on one of the FSs have to drift in the “wrong” direction. As Fig. 3.2 shows, the direction of the drift and thus the signs of the transport times are set by the majority carriers.

On the other hand, for nearly isotropic scattering, $a \approx 0$, Fig. 3.2 shows that $\tau_s/\tau_{0,s}$ decreases with decreasing a regardless of the FS sizes. Slightly increasing anisotropy favors small- θ scattering. For the electron-hole case, this enhances backscattering since the velocities $\mathbf{v}_{s,\mathbf{k}}$ and $\mathbf{v}_{\bar{s},\bar{\mathbf{k}}}$ are opposite and is therefore more efficient in relaxing the current. For the compensated case, $\gamma_s = 1$, this mechanism is effective at all anisotropy levels. In particular, for $a \rightarrow -1$ the ratio goes to $\tau_s/\tau_{0,s} \rightarrow 1/2$, which means that the system relaxes twice as fast if the scattering is pure backscattering instead of completely isotropic.

In case of two electronlike or two holelike FSs, $a \in [0, 1]$, the carriers from both FSs always drift in the same direction, as expected. The transport times increase monotonically with a and diverge in the extreme anisotropic limit $a \rightarrow 1$. The increasing anisotropy favors small- θ scattering, which corresponds to forward scattering, and is thus increasingly inefficient at relaxing the current. The compensated case, $\gamma_s = 1$, is not special because $f_{s\mathbf{k}} + f_{\bar{s}\bar{\mathbf{k}}} \neq 2n_F(\varepsilon_{\mathbf{k}})$ for any γ_s if the FSs are of equal type.

3.4 Transport coefficients

In this section I will calculate measurable transport coefficients, to search for signatures of the negative transport times.

3.4.1 Resistivity

The resistivity can be obtained from the transport times by standard methods [74],

$$\rho = \left(e^2 \sum_s N_s v_s^2 \tau_s^{\text{tr}} \right)^{-1}. \quad (3.9)$$

For simplicity we consider equal densities of states, $N_s = N_{\bar{s}}$. In this case the resistivity relative to its isotropic limit reads

$$\frac{\rho}{\rho|_{a=0}} = \frac{1 - a^2}{1 + a \frac{2}{\gamma_1 + \gamma_2}}. \quad (3.10)$$

Fig. 3.2(b) shows that although minority carriers give a negative contribution to the current for $a < a^*$, the total current is always positive as required by the stability criterion [80].

In the uncompensated case ($\gamma_s \neq 1$) the competition between the two anisotropy effects, the usual enhancement of the resistivity due to backscattering and the reduction due to anisotropic scattering causes a maximum of ρ/ρ_0 as a function of a at $a = a^*$.

Consistent with previous investigations [54] we find that in compensated e-h systems ρ/ρ_0 exhibits an enhancement up to a factor of two due to the usual backscattering. The enhancement by a factor two can be achieved for $a \rightarrow -1$, which corresponds to pure backscattering, as discussed in section 3.3. In uncompensated e-h systems, however, anisotropy of the scattering causes a strong reduction of the resistivity below $a = a^*$, which occurs already at weak anisotropy, if the mismatch between the FS radii is large.

3.4.2 Magnetoresistance and Hall coefficient

As discussed in section 2.4, in the presence of a magnetic field it is useful to write $\Lambda_{s\mathbf{k}} = \sum_{n=0}^{\infty} \Lambda_{s\mathbf{k}}^{(n)}$, where $\Lambda_{s\mathbf{k}}^{(n)}$ is of order n in the magnetic field B . Standard analysis [73] then shows that for $\Lambda_{s\mathbf{k}}^{(1)}$ one has to replace $\mathbf{v}_{s\mathbf{k}}$ in the solution for $\Lambda_{s\mathbf{k}}^{(0)}$, Eq. (3.6), by $\omega_s \mathbf{z} \times \Lambda_{s\mathbf{k}}^{(0)}$, where $\omega_s = \text{sgn}(\mathbf{v}_{s\mathbf{k}} \cdot \mathbf{k}) (eB/\hbar) v_s/k_s$. Following

this analysis and again assuming $N_s = N_{\bar{s}}$ for simplicity, we obtain

$$\begin{aligned}\Lambda_{\mathbf{sk}}^{(1)} &= \frac{\tau_s}{1-a^2} (\omega_s \mathbf{z} \times \Lambda_{\mathbf{sk}}^{(0)} + \eta a \omega_{\bar{s}} \mathbf{z} \times \Lambda_{\bar{\mathbf{s}}\mathbf{k}}^{(0)}) \\ &= \left(\frac{\tau_s}{1-a^2} \right)^2 \mathbf{z} \times \mathbf{v}_{\mathbf{sk}} \gamma_{\bar{s}} [(\gamma_s + a)\omega_s + a(1 + \gamma_s a)\omega_{\bar{s}}],\end{aligned}\quad (3.11)$$

where we have used that $\Lambda_{\bar{\mathbf{s}}\mathbf{k}}^{(0)} = \Lambda_{\mathbf{sk}}^{(0)} \eta (1 + \gamma_s a)/(\gamma_s + a)$ as shown by Eq. (3.6). The solution for $\Lambda_{\mathbf{sk}}^{(2)}$ is obtained from Eq. (3.11) by increasing the superscript indices by one, which leads to

$$\begin{aligned}\Lambda_{\mathbf{sk}}^{(2)} &= -\left(\frac{\tau_s}{1-a^2} \right)^3 \mathbf{v}_{\mathbf{sk}} \gamma_{\bar{s}} [(\gamma_s + a)\omega_s^2 + a(1 + \gamma_s a)\omega_s \omega_{\bar{s}} \\ &\quad + a(1 + \gamma_s a)\omega_{\bar{s}}^2 + a^2(a + \gamma_s)\omega_s \omega_{\bar{s}}].\end{aligned}\quad (3.12)$$

The total MFP determines the conductivity tensor

$$\sigma^{ij} = e^2 \sum_{\mathbf{sk}} N_s \mathbf{v}_{\mathbf{sk}}^i \sum_n \Lambda_{\mathbf{sk}}^{(n)j}, \quad (3.13)$$

which in turn determines the resistivity and the Hall coefficient in the standard way [74]. The expressions in terms of the anisotropy parameter a read

$$\frac{R_H}{R_H|_{a=0}} = \frac{(1 + \gamma_s^2)^2 [\gamma_s (a + \gamma_s)^2 + \eta \gamma_s^\alpha (1 + a\gamma_s)^2]}{(1 + 2a\gamma_s + \gamma_s^2)^2 (\gamma_s^3 + \eta \gamma_s^\alpha)}, \quad (3.14)$$

$$\begin{aligned}\frac{\Delta\rho}{\Delta\rho|_{a=0}} &= (1 + \gamma_s^2)^2 \\ &\times \frac{[-\eta (a + \gamma_s)^2 + 2\gamma_s^\alpha (a + \gamma_s) (1 + a\gamma_s) - \eta \gamma_s^{2\alpha} (1 + a\gamma_s)^2]}{(1 - a^2) (1 + 2a\gamma_s + \gamma_s^2)^2 [2\gamma_s^{1+\alpha} - \eta (\gamma_s^2 + \gamma_s^{2\alpha})]},\end{aligned}\quad (3.15)$$

where the magnetoresistance is defined as $\Delta\rho \equiv [\rho(B) - \rho(0)]/\rho(0)$ and $\alpha \equiv 1/(d-1)$. Note that the results in Eqs. (3.14) and (3.15) differ from those in Ref. [17] where some vertex corrections for $\Lambda_{\mathbf{sk}}^{(1)}$ and $\Lambda_{\mathbf{sk}}^{(2)}$ were neglected.

The results for the electron-hole case are shown in Fig. 3.4. Most interestingly, in the presence of a magnetic field we encounter a second characteristic anisotropy

$$a^{**} \equiv -\frac{\gamma_s + \gamma_s^\alpha}{1 + \gamma_s^{\alpha+1}} \leq a^*, \quad (3.16)$$

at which the Hall coefficient and the magnetoresistance show a maximum and a minimum as a function of a , respectively. To understand the significance of the

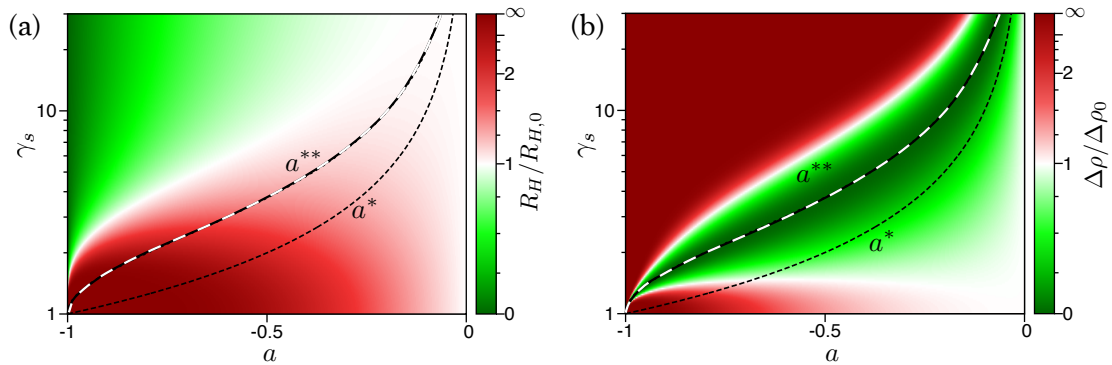


Figure 3.4: Hall coefficient (a) and magnetoresistance (b) for $d = 2$ as a function of a and γ_s , in units of the isotropic limits, $\Delta\rho_0 \equiv \Delta\rho|_{a=0}$ and $R_{H,0} \equiv R_H|_{a=0}$. At the characteristic anisotropy a^{**} (black-white dashed) the Hall coefficient has a maximum as a function of a . The magnetoresistance has a minimum at a^{**} with zero magnetoresistance. Results for 3D are qualitatively similar.

anisotropy a^{**} , it is useful to consider the deflection angle ϕ_s , i.e., the angle by which the electron on the FS s is deflected due to the magnetic field. This is easily achieved by noting that without the magnetic field the MFP reads $\Lambda_{s\mathbf{k}}^{(0)}$, while in the presence of a magnetic field the MFP reads $\Lambda_{s\mathbf{k}}^{(0)} + \Lambda_{s\mathbf{k}}^{(1)}$ to leading order in B , where $\Lambda_{s\mathbf{k}}^{(0)}$ is parallel to \mathbf{k} and, according to Eq. (3.11), $\Lambda_{s\mathbf{k}}^{(1)}$ is parallel to $\mathbf{z} \times \mathbf{k}$. This leads to

$$\phi_s = \arctan \frac{(\mathbf{z} \times \mathbf{k}) \cdot \Lambda_{s\mathbf{k}}^{(1)}}{\mathbf{k} \cdot \Lambda_{s\mathbf{k}}^{(0)}}. \quad (3.17)$$

The significance of the anisotropy a^{**} is that for $a = a^{**}$ the deflection angles on both FSs are equal,

$$\phi_s|_{a=a^{**}} = \phi_{\bar{s}}|_{a=a^{**}}, \quad (3.18)$$

which can be easily verified using the results for $\Lambda_{s\mathbf{k}}^{(0)}$ and $\Lambda_{s\mathbf{k}}^{(1)}$. Equal deflection angles are possible because one of the transport times is negative. Otherwise, if the transport times were both positive, the deflection angles would have different signs.

In a conventional electron-hole system with positive transport times, deflection angles with different signs lead to a reduced Hall coefficient compared to the Hall coefficient of a single-carrier system with otherwise comparable parameters. On the other hand, the magnetoresistance of a conventional electron-hole system is finite, while it is zero for a single-carrier system [74] because the absolute value of the total current does not change in the magnetic field.

In an electron-hole system with anisotropic scattering and $a \approx a^{**}$, the behavior of the Hall coefficient and magnetoresistance is qualitatively the same as that of a single-carrier system: The Hall coefficient is enhanced while the magnetoresistance is reduced. We can understand this by noting that at $a = a^{**}$ the deflection angles of both carriers are equal and the system thus behaves like a single-carrier system in a magnetic field.

A surprisingly small magnetoresistance in comparison to the Hall coefficient has been observed in iron pnictides [3], which might be a signature of negative transport times. In contrast to Ref. [17], here we find the magnetoresistance to be positive over the entire parameter range, in agreement with the experiments.

3.5 Conclusions

In conclusion, we have found that anisotropic single-particle scattering between electron and hole FSs causes the transport times to deviate dramatically from the lifetime. In particular, anisotropic scattering can lead to negative transport times for the minority carriers. The degree of anisotropy required for this decreases for increasing ratio between the size of the FSs. This effect does not depend on a particular microscopic origin of the anisotropic scattering and is distinct from carrier drag due to the two-particle electron-hole interaction [81, 82].

The most striking signatures of negative transport times are the enhanced Hall coefficient and zero magnetoresistance. Close to perfect nesting, negative transport times are restricted to the limit of strong scattering anisotropy and thus should only become evident in the transport just above the excitonic instability, e.g., close to the SDW transition in iron pnictides. It is encouraging that in the pnictides the magnetoresistance is rather small [3], while the Hall coefficient is strongly enhanced close to the SDW transition [4, 85], consistent with our predictions.

For imperfect nesting the effects could also be visible at weaker scattering anisotropy. One can speculate that the broad maximum [5, 86] in the Hall coefficient in LiFeAs and LiFeP as a function of temperature is related to the maximum at a^{**} , as these materials have rather poor nesting and γ_s could differ significantly from unity.

4 Transport in multiband systems with hot spots on the Fermi surface

In the previous chapter we have explored the effect of anisotropic interband scattering within a simple model of two concentric FSs with centers separated by \mathbf{Q} . Because of rotational symmetry of this model we could find an exact solution of the Boltzmann equation. In this chapter we will make the model more realistic with regard to iron pnictides by breaking the rotational symmetry of the FSs. This will lead to the revision of the concept of hot spots. In particular, we will find that this concept, developed for one-band systems, is not transferable to the case of iron pnictides. Parts of this chapter have been published in Ref. [18].

4.1 Introduction

In real materials such as iron pnictides, the distortion of the FSs from a perfectly circular shape can lead to the emergence of the so-called hot and cold regions on the FS, which can be understood in the following way: Consider the model of the previous chapter with two FSs of nearly equal radii and a scattering rate peaked at momentum transfer \mathbf{Q} . Now let us distort one of the 2D (3D) FSs such that its shape becomes elliptical (ellipsoidal). In 2D (3D) four points (two lines) emerge on each of the FSs such that each of these points (lines) can be connected to a point (line) on the other FS by \mathbf{Q} . These are the so-called *hot spots* (*hot lines*) [14, 87]. In the hot regions around these states, scattering is particularly strong, while in the cold regions not connected by \mathbf{Q} the scattering rate is lower.

To understand the transport, one can think of different parts of the FS as parallel connected resistors. In particular, for a FS with hot and cold regions, one can assume two parallel resistors with high and low resistivity, respectively. Since the total resistivity is set by the resistor with lower resistivity, one can conclude

that transport is dominated by the cold regions, while the hot regions are said to be “short circuited” by the cold regions.

The successful concept of hot and cold regions has been developed in the context of cuprates and heavy-fermion materials [14, 87]. This concept was implicitly assumed to hold also for the iron pnictides [3, 53, 58, 88]. An analysis of the lifetimes of excited electrons close to the FSs seems to support this picture [84]. The pnictides indeed show hot and cold regions with short and long *lifetimes*, respectively. Hence, one is led to assume that the states with short lifetimes do not significantly contribute to the transport [87].

In the previous chapters we have already seen, however, that the *relaxation times* might significantly deviate from the lifetimes in multiband systems. Indeed, in this chapter we will find that the concept of hot and cold regions fails for the case of iron pnictides. In contrast to the lifetimes, which are highly anisotropic around the Fermi pockets with deep minima at the hot spots, the effective relaxation times are found to be much more isotropic and to show no special features at the hot spots. Our approximate analytical solution of the Boltzmann equation [18] provides insight into the mechanism behind this effect: The anisotropy of the spin-fluctuation scattering increases the effective relaxation time. At the hot spots, the reduction of the relaxation time due to the stronger scattering is thus compensated by the increase due to the higher anisotropy.

4.2 Model

I use an effective two-dimensional two-band model for the FeAs layers of the iron pnictides [24]. The dispersions are given by

$$\varepsilon_{h\mathbf{k}} = \varepsilon_h - \mu + 2t_h (\cos k_x a + \cos k_y a), \quad (4.1)$$

$$\varepsilon_{e\mathbf{k}} = \varepsilon_e - \mu + t_{e,1} \cos k_x a \cos k_y a - t_{e,2} \xi (\cos k_x a + \cos k_y a), \quad (4.2)$$

where a is the iron-iron separation. I use a single-iron unit cell [34]. As illustrated in Fig. 4.1, the band h gives rise to a nearly circular holelike Fermi pocket at the center of the Brillouin zone, while the band e forms two electronlike pockets eX and eY , displaced by $\mathbf{Q}_X = (0, \pi)$ and $\mathbf{Q}_Y = (\pi, 0)$, respectively. The parameter ξ controls the ellipticity (eccentricity) of the electron pockets. The chemical potential μ will in the following be determined from the given filling n , i.e., the number of electrons per unit cell. Following Ref. [24], I take $\varepsilon_h = -3.5 t_h$, $\varepsilon_e = 3 t_h$,

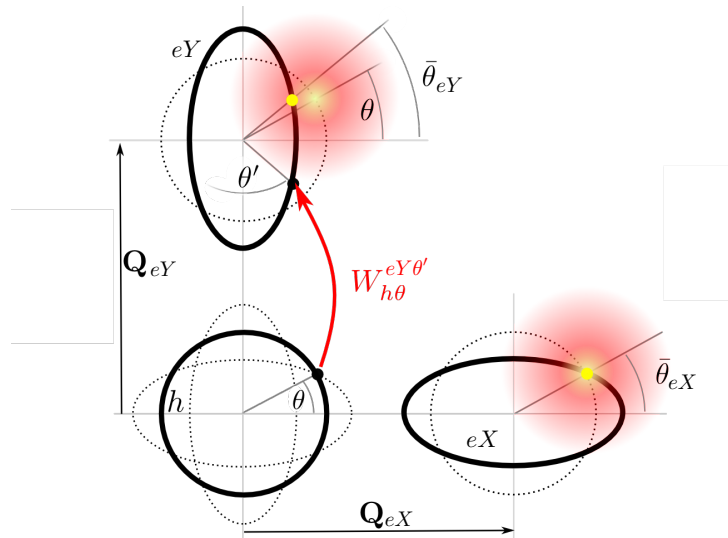


Figure 4.1: Illustration of the Fermi pockets and the scattering rates. An electron in state $|h, \theta\rangle$ is scattered to $|eY, \theta'\rangle$. The yellow dots indicate the maxima of the scattering rates $W_{h\theta}^{eY\theta'}$ and $W_{h\theta}^{eX\theta'}$ as functions of the polar angle θ' on the target Fermi pocket. The maxima stem from the enhanced spin susceptibility (color gradient) for the scattering wave vectors \mathbf{Q}_X and \mathbf{Q}_Y . The thin dotted lines show the FSs displaced by the nesting vectors. After Ref. [18].

$$t_{e,1} = 4t_h, \text{ and } t_{e,2} = t_h.$$

I assume that the transport behavior is dominated by the scattering off spin fluctuations. The spin-fluctuation spectrum determines the scattering rate as described in section 2.2. Within the considered model [24], I have investigated the spin-fluctuation spectrum numerically using the random-phase approximation. It is more convenient, however, to model the susceptibility phenomenologically, which allows to circumvent the numerically costly calculation of the spin-fluctuation spectrum and to focus on the transport behavior alone. We shall see that the precise form of the susceptibility is less important for transport if vertex corrections are included than for transport calculations based purely on lifetimes [84]. We use the Millis-Monien-Pines model [89], which has been used to fit neutron-scattering experiments [60, 61] on iron pnictides, thus providing realistic values for the parameters of the spin-fluctuation spectrum.

Together with momentum-independent impurity scattering, the scattering rate from a single-electron state $|b, \mathbf{k}\rangle$ to a state $|b', \mathbf{k}'\rangle$, where $b = e, h$ denotes the

band, can be written as

$$W_{b\mathbf{k}}^{b'\mathbf{k}'} = (1 - \delta_{bb'}) W_{\text{sf}} \frac{p_T(\varepsilon_{b\mathbf{k}} - \varepsilon_{b'\mathbf{k}'})}{(\varepsilon_{b\mathbf{k}} - \varepsilon_{b'\mathbf{k}'})^2 + \omega_{\mathbf{k},\mathbf{k}'}^2} + \delta(\varepsilon_{b\mathbf{k}} - \varepsilon_{b'\mathbf{k}'}) W_{\text{imp}}, \quad (4.3)$$

where W_{sf} and W_{imp} represent the overall strengths of the scattering due to spin fluctuations and impurities, respectively, $p_T(x)$ is defined in Eq. (2.12) and

$$\omega_{\mathbf{k},\mathbf{k}'} \equiv \Gamma_T \left(1 + \xi_T^2 \min[(\mathbf{k} - \mathbf{k}' + \mathbf{Q})^2] \right), \quad (4.4)$$

where the four possible values for \mathbf{Q} are $\pm\mathbf{Q}_X$ and $\pm\mathbf{Q}_Y$. With the Curie-Weiß temperature $-\theta_{\text{CW}} < 0$, the frequency scale and the correlation length are given by [54, 60] $\Gamma_T = \Gamma_0 (T + \theta_{\text{CW}})/\theta_{\text{CW}}$ and $\xi_T = \xi_0 \sqrt{\theta_{\text{CW}}/(T + \theta_{\text{CW}})} \exp(-T/T_0)$, respectively. Following Ref. [54], I here introduce an additional exponential decay of ξ_T to account for the high-temperature behavior and choose $T_0 = 200$ K. According to Ref. [60], I take $\xi_0 = 10a$, $\theta_{\text{CW}} = 30$ K and $\Gamma_0 = 4.2$ meV. The resulting form of $\omega_{\mathbf{k},\mathbf{k}'}$ and thus of $W_{b\mathbf{k}}^{b'\mathbf{k}'}$ is only valid as long as the system does not order antiferromagnetically or becomes superconducting.

The transport is governed by states on the Fermi pockets, denoted by $|s, \theta\rangle$, where $s = h, eX, eY$ is the pocket index and θ is the polar angle along the pocket, see Fig. 4.1. From Eq. (4.3) we see that in the low-temperature regime, $k_B T \ll \varepsilon_F$, the scattering rate is sharply peaked at $\varepsilon_{b\mathbf{k}} = \varepsilon_{b'\mathbf{k}'}$ so that scattering is nearly elastic. I exploit this fact by writing

$$W_{b\mathbf{k}_F}^{b'\mathbf{k}'_F} \approx \delta(\varepsilon_{b'\mathbf{k}'_F} - \varepsilon_F) W_{s\theta}^{s'\theta'}, \quad (4.5)$$

where

$$W_{s\theta}^{s'\theta'} \equiv (1 - \delta_{ss'}) W_{\text{sf}} \int d\varepsilon \frac{p(\varepsilon)}{\varepsilon^2 + \omega_{\mathbf{k},\mathbf{k}'}^2} + W_{\text{imp}} \quad (4.6)$$

is the effective elastic scattering rate between states on the Fermi pockets s, s' belonging to the bands b, b' . Since the spin susceptibility and thus $W_{b\mathbf{k}}^{b'\mathbf{k}'}$ is strongly momentum dependent, the elastic scattering rate $W_{s\theta}^{s'\theta'}$ strongly depends on the angles θ and θ' , in particular on the change in angle upon scattering, $\theta' - \theta$.

More specifically, the anisotropy stems from the spin-susceptibility peaks at the wave vectors $\pm\mathbf{Q}_X$ and $\pm\mathbf{Q}_Y$. For an initial state $|h, \theta\rangle$ with wave vector \mathbf{k} , the scattering rate has maxima for the final states $|eX, \bar{\theta}_{eX}\rangle$ and $|eY, \bar{\theta}_{eY}\rangle$, defined as the states on the Fermi pockets eX, eY with wave vectors closest to $\mathbf{k} + \mathbf{Q}_X$ and $\mathbf{k} + \mathbf{Q}_Y$, respectively, see Fig. 4.1. Similarly, for an initial state $|eX, \theta\rangle$ ($|eY, \theta\rangle$)

with wave vector \mathbf{k} , the scattering rate has a maximum for the final state $|h, \bar{\theta}_h\rangle$ with wave vector closest to $\mathbf{k} - \mathbf{Q}_X$ ($\mathbf{k} - \mathbf{Q}_Y$), where $\bar{\theta}_h \approx \theta$ since the hole pocket is nearly circular.

The scattering rate summed over all final states determines the lifetime of the state $|s, \theta\rangle$ (cf. section 2.2),

$$\tau_{s\theta} = \left(\frac{1}{2\pi} \sum_{s'} \int d\theta' N_{s'\theta'} W_{s\theta}^{s'\theta'} \right)^{-1}, \quad (4.7)$$

where $N_{s\theta} = |d\mathbf{k}_{s\theta}/d\theta|/|\pi\hbar \mathbf{v}_{s\theta}|$ is the state-resolved density of states (including spin-degeneracy) introduced in section 2.5.

4.3 Analytical considerations

With the new parametrization of the Fermi-pocket states, the Boltzmann equation (2.9) reads

$$\Lambda_{s\theta} = \Lambda_{s\theta}^D + \tau_{s\theta} \sum_{s'} \int \frac{d\theta'}{2\pi} N_{s'\theta'} W_{s\theta}^{s'\theta'} \Lambda_{s'\theta'}, \quad (4.8)$$

where $\Lambda_{s\theta}^D \equiv \tau_{s\theta} \mathbf{v}_{s\theta}$ is the Drude MFP, defined in section 2.3. In this section I will construct an approximate analytical solution of Eq. (4.8) that will fully account for the scattering anisotropy. The assumptions I will make are such that the result becomes exact in the limits of both strong and weak scattering anisotropy. Later, we will compare the approximation to numerical calculations.

As illustrated in Fig. 4.1, the scattering rate $W_{s\theta}^{s'\theta'}$ understood as a function of θ' has a maximum at $\theta' = \bar{\theta}_{s'}$, which of course depends on θ . The small difference between θ and $\bar{\theta}_{s'}$ stems from the ellipticity of the electron pockets. We now make two simplifying assumptions: (i) The peak of the scattering rate $W_{s\theta}^{s'\theta'}$ as a function of θ' is assumed to be symmetric around $\theta' = \bar{\theta}_{s'}$ and (ii) the peak width is small on the scale on which the Fermi velocity $|\mathbf{v}_{s\theta}|$ and the density of states $N_{s\theta}$ vary. Both assumptions become exact in the limit of very strongly peaked spin susceptibility, i.e., as the magnetic instability is approached. In the opposite limit of isotropic scattering, the forward-scattering corrections cancel out so that we also obtain the exact results.

On the right-hand side of Eq. (4.8), we split $\Lambda_{s'\theta'}$ into contributions parallel

and perpendicular to $\mathbf{\Lambda}_{s'\bar{\theta}_{s'}}$,

$$\mathbf{\Lambda}_{s'\theta'} = \frac{|\mathbf{\Lambda}_{s'\theta'}|}{|\mathbf{\Lambda}_{s'\bar{\theta}_{s'}}|} \left[\mathbf{\Lambda}_{s'\bar{\theta}_{s'}} \cos \Delta(s', \theta', \bar{\theta}_{s'}) + \mathbf{z} \times \mathbf{\Lambda}_{s'\bar{\theta}_{s'}} \sin \Delta(s', \theta', \bar{\theta}_{s'}) \right], \quad (4.9)$$

where $\Delta(s', \theta', \bar{\theta}_{s'})$ is the angle included by $\mathbf{\Lambda}_{s'\theta'}$ and $\mathbf{\Lambda}_{s'\bar{\theta}_{s'}}$. By virtue of the assumptions (i) and (ii), the sine term drops out and we obtain

$$\mathbf{\Lambda}_{s\theta} = \mathbf{\Lambda}_{s\theta}^D + \left(1 - \frac{1}{2} \delta_{s,h} \right) \sum_{s'} a_{s\theta}^{s'} \mathbf{\Lambda}_{s'\bar{\theta}_{s'}}, \quad (4.10)$$

where

$$a_{s\theta}^{s'} \equiv (1 + \delta_{s,h}) \tau_{s\theta} \int \frac{d\theta'}{2\pi} N_{s'\theta'} W_{s\theta}^{s'\theta'} \cos \Delta(s', \theta', \bar{\theta}_{s'}) \quad (4.11)$$

parametrizes the scattering anisotropy and in the following will be referred to as the *anisotropy parameter* similar to chapter 3. The Kronecker symbols $\delta_{s,h}$ appearing in Eqs. (4.10) and (4.11) ensure that $a_{s\theta}^{s'} \in [0, 1]$ and that $a_{s\theta}^{s'} \rightarrow 1$ corresponds to the limit of strong scattering anisotropy, $W_{s\theta}^{s'\theta'} \propto \delta(\theta' - \bar{\theta}_{s'})$, while $a_{s\theta}^{s'} \rightarrow 0$ gives the case of isotropic scattering, where the Drude result is recovered.

Iterating Eq. (4.10), we obtain $\mathbf{\Lambda}$ in terms of $\mathbf{\Lambda}^D$ as a power series in the anisotropy parameter. I now discuss the states appearing in this series. The zero-order contribution to $\mathbf{\Lambda}_{s\theta}$ is of course $\mathbf{\Lambda}_{s\theta}^D$, the Drude result for the same state $|s, \theta\rangle$. The first-order term involves $\mathbf{\Lambda}_{s'\bar{\theta}_{s'}}^D$ for the state $|s', \bar{\theta}_{s'}\rangle$. This is the *final* state on the Fermi pocket $s' \neq s$ to which the *initial* state $|s, \theta\rangle$ has the largest scattering rate. Due to the ellipticity of the electron pockets, the shift of the angle, $\bar{\theta}_{s'} - \theta$, is always directed towards the closest hot spot, i.e., the intersection of the Fermi pocket s with pocket s' shifted by the appropriate vector \mathbf{Q} . The state appearing in the second-order term is the one reached from $|s', \bar{\theta}_{s'}\rangle$ with the largest scattering rate, again shifted towards the closest hot spot. The states appearing in all higher-order terms are obtained in the same way. The whole process can be interpreted as an effective hopping of the electron along a sequence of states towards the closest hot spot, as illustrated by Fig. 4.2. The effective angular shift of the electrons along the Fermi line is due to the ellipticity of the electron pockets and vanishes for a purely circular pocket. I will now neglect the shift and focus on its effect in the next subsection.

Accordingly setting $\bar{\theta}_{s'} = \theta$ in Eq. (4.10), the MFPs for different θ decouple,

and we obtain

$$\Lambda_{h\theta} = \frac{\Lambda_{h\theta}^D + \frac{1}{2} (a_{h\theta}^{eX} \Lambda_{eX\theta}^D + a_{h\theta}^{eY} \Lambda_{eY\theta}^D)}{1 - \frac{1}{2} (a_{h\theta}^{eX} a_{eX\theta}^h + a_{h\theta}^{eY} a_{eY\theta}^h)}, \quad (4.12)$$

$$\Lambda_{eX\theta} = \Lambda_{eX\theta}^D + a_{eX\theta}^h \Lambda_{h\theta}, \quad (4.13)$$

$$\Lambda_{eY\theta} = \Lambda_{eY\theta}^D + a_{eY\theta}^h \Lambda_{h\theta}. \quad (4.14)$$

Since the anisotropy parameters $a_{s\theta}^{s'}$ are the only parameters in the solution, apart from the Drude MFPs $\Lambda_{s\theta}^D$, we will refer to these expressions as the *anisotropy approximation* (AA). Clearly, for $a_{s\theta}^{s'} \neq 0$ the MFPs involve the Drude solutions of all three Fermi pockets. This coupling between the pockets becomes stronger for larger anisotropy parameters. Additionally, the denominator in Eq. (4.12), which appears in all results, provides a factor that is larger than unity. In the anisotropic limit, $a_{s\theta}^{s'} \rightarrow 1$, the MFPs $\Lambda_{s\theta}$ of all three pockets at a certain angle θ become equal and diverge. Thus, for strong anisotropy the MFP either of the holes or of the electrons must be *inverted* relative to the Drude result $\Lambda_{s\theta}^D = \tau_{s\theta} \mathbf{v}_{s\theta}$, which corresponds to negative transport times, discussed in the previous chapter. We will see in section 4.4.2 that inverted MFPs occur on the hole pocket due to the dominance of states on the electron pockets.

Semiclassically, we can interpret our results as follows. The solution to the Boltzmann equation describes a non-equilibrium steady state in which the acceleration of the electrons due to external forces is balanced by scattering. The MFP of state $|s, \theta\rangle$ can be understood as the displacement that an electron suffers until its velocity $\mathbf{v}_{s\theta}$ is randomized by scattering. The lifetime $\tau_{s\theta}$ is the mean time between two scattering events. If the scattering is isotropic the velocity is randomized after a single scattering event and the MFP thus reads $\tau_{s\theta} \mathbf{v}_{s\theta} \equiv \Lambda_{s\theta}^D$. On the other hand, anisotropic scattering only partially randomizes the velocity so that the effective relaxation time exceeds the lifetime $\tau_{s\theta}$, giving rise to multiple scattering during the relaxation, see Fig. 4.2. The enhancement by the denominator in Eq. (4.12) accounts for this fact. In the extreme limit of $a_{s\theta}^{s'} \rightarrow 1$, the factor diverges, indicating that the velocities cannot relax at all and the MFPs become infinite.

4.3.1 Angular shift towards the hot spot

Let us now focus on the correction to the MFP due to the angular shift towards the hot spot for small ellipticities. For an estimate of the upper limit of the correction,

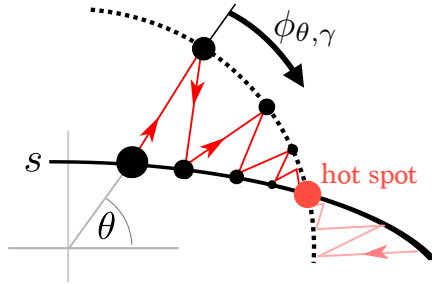


Figure 4.2: Scattering of an electron initially in state $|s, \theta\rangle$ between different pockets towards the closest hot spot (red dot). The sequence of states (black dots) is given by the maximum of the scattering rate. Their decreasing contribution to the MFP of the original state $|s, \theta\rangle$ is indicated by the decreasing size of the dots. The effective angular shift of the electronic state is denoted $\phi_{\theta, \gamma}$. After Ref. [18].

it is sufficient to consider only a *single* electron pocket. For simplicity we assume a circular hole pocket with the Fermi wave number k and an elliptical electron pocket described by the semi-major and semi-minor axis $k_a = k(1 - \epsilon^2)^{-1/4}$ and $k_b = k(1 - \epsilon^2)^{1/4}$, respectively, where ϵ is the eccentricity of the ellipse. To focus on the shift effect we assume constant anisotropy, $a_{s\theta}^s = a$. For two Fermi pockets and constant anisotropy, Eq. (4.10) takes the form

$$\Lambda_{s\theta} = \Lambda_{s\bar{\theta}}^D + a \Lambda_{s\bar{\theta}}, \quad (4.15)$$

where $\bar{h} = e$, $\bar{e} = h$. Using simple trigonometry, we find that for the given geometry, the difference between $\bar{\theta}$ and θ to leading order in the eccentricity ϵ reads $(\epsilon^4/16) \sin 4\theta$. Iterating Eq. (4.15), we obtain the solution for the electron pocket as

$$\Lambda_{e\theta} = \sum_{n=0}^{\infty} a^{2n} (\Lambda_{e\theta_n}^D + a \Lambda_{h\theta_n}^D), \quad (4.16)$$

with

$$\theta_n = \theta_{n-1} + \frac{\epsilon^4}{16} \sin 4\theta_{n-1} \quad \text{and} \quad \theta_0 = \theta. \quad (4.17)$$

The solution for the hole pocket follows immediately from Eqs. (4.15) and (4.16). Replacing the discrete index n by a continuous variable, we obtain

$$\Lambda_{e\theta} = -\frac{2 \ln a}{1 - a^2} \int_0^{\infty} dn a^{2n} (\Lambda_{e\theta_n}^D + a \Lambda_{h\theta_n}^D) + \mathbf{R}, \quad (4.18)$$

with a correction \mathbf{R} . By splitting the integration range into intervals $[m, m + 1]$ with integer m , one can easily show that

$$|\mathbf{R}| \leq \sum_n a^{2n} |(\mathbf{\Lambda}_{e\theta_n}^D + a\mathbf{\Lambda}_{h\theta_n}^D) - (\mathbf{\Lambda}_{e\theta_{n+1}}^D + a\mathbf{\Lambda}_{h\theta_{n+1}}^D)|, \quad (4.19)$$

which is obviously of higher order in ϵ^2 because of Eq. (4.17). Substituting $n = 4 \ln(1 + z)/\epsilon^4$ we obtain

$$\mathbf{\Lambda}_{e\theta} = \frac{1}{1 - a^2} \int_0^\infty dz \gamma \left(\frac{1}{1 + z} \right)^{\gamma+1} (\mathbf{\Lambda}_{e\theta(z)}^D + a\mathbf{\Lambda}_{h\theta(z)}^D), \quad (4.20)$$

with

$$\gamma \equiv 8 \frac{\ln(1/a)}{\epsilon^4} \quad (4.21)$$

and

$$\theta(z) \equiv \frac{1}{2} \arctan [(z + 1) \tan 2\theta]. \quad (4.22)$$

In the integral in Eq. (4.20), the factor $\gamma [1/(1 + z)]^{\gamma+1}$ acts as a distribution function which is normalized to unity and becomes a δ -function in the limit of zero ellipticity, i.e., for $\gamma \rightarrow \infty$. Hence, the largest shifts are achieved for small values of γ , which, according to Eq. (4.21), correspond to large scattering anisotropy and large ellipticity.

The shift also depends on the position on the pocket. There is no shift at the hot spots, $\theta = (2n - 1)\pi/4$, and at the cold spots, $\theta = n\pi/2$. The largest shift can be expected to occur between the hot and cold spots, in the vicinity of $(2n - 1)\pi/8$.

We can make further analytical progress by expanding the vector $(\mathbf{\Lambda}_{e\theta(z)}^D + a\mathbf{\Lambda}_{h\theta(z)}^D)$ to linear order in $\theta(z)$. This is best justified if the total angular shift is small, i.e., if we start with θ close to a hot spot. However, the total shift can never be larger than $\pi/4$ so that the approximation always gives at least qualitatively correct results for not excessive eccentricities. Equation (4.20) can then be written as

$$\mathbf{\Lambda}_{e\theta} = \frac{1}{1 - a^2} (\mathbf{\Lambda}_{e,\theta+\phi_{\theta,\gamma}}^D + a\mathbf{\Lambda}_{h,\theta+\phi_{\theta,\gamma}}^D), \quad (4.23)$$

with the effective angular shift

$$\begin{aligned} \phi_{\theta,\gamma} &= \int_0^\infty dz \gamma \left(\frac{1}{1 + z} \right)^{\gamma+1} \theta(z) - \theta \\ &\cong \frac{\sin 4\theta}{32} \frac{\epsilon^4}{\ln(1/a)} + \frac{\sin 8\theta}{512} \left[\frac{\epsilon^4}{\ln(1/a)} \right]^2 + \mathcal{O} \left(\left[\frac{\epsilon^4}{\ln(1/a)} \right]^3 \right). \end{aligned} \quad (4.24)$$

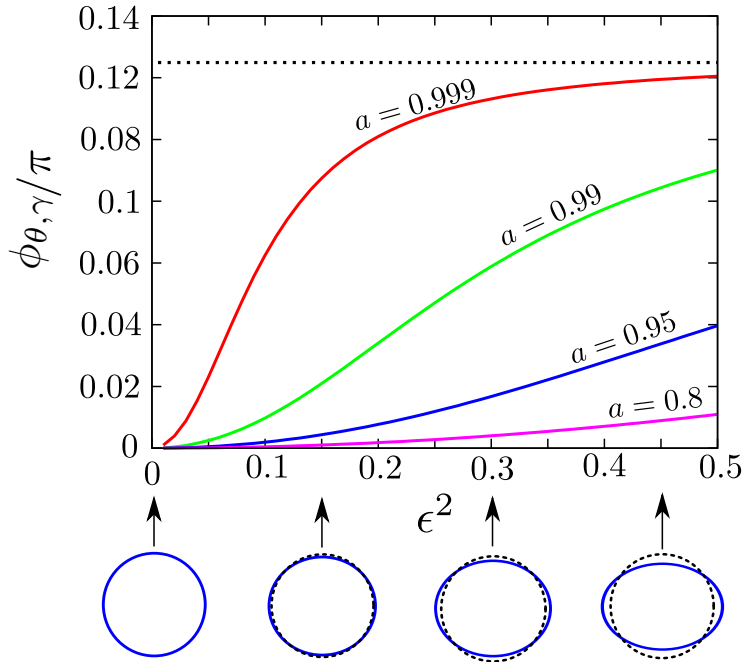


Figure 4.3: Effective angular shift $\phi_{\theta,\gamma}$ for the state $\theta = \pi/8$ as a function of ϵ^2 for different uniform anisotropies a . ϵ represents the eccentricity of the electron pocket. The shift is directed towards the hot spot at $\theta = \pi/4$, hence the maximal value of $\phi_{\theta,\gamma}/\pi$ is $1/8$. Below the graph, the shape of the electron pocket (solid line) corresponding to various values of ϵ^2 is indicated. From Ref. [18].

In Fig. 4.3 we plot the angular shift at $\theta = \pi/8$ for different anisotropies as a function of the eccentricity squared, ϵ^2 . Realistic scattering anisotropies hardly exceed the value $a = 0.95$ (see below), for which the shift is small up to $\epsilon^2 \approx 0.5$. Stronger ellipticities might, however, lead to significant corrections.

4.4 Results

To obtain quantitative results without approximations beyond the choice of the model and the semiclassical transport theory, we calculate the scattering rate given in Eq. (4.6) by numerical integration. Furthermore, we discretize the polar angle θ , choosing 160 sites on each Fermi pocket. Taking more points does not significantly change the results. The lifetimes given in Eq. (4.7) and the anisotropy parameters from Eq. (4.11) are obtained by summation over the discrete sites. For the calculation of the anisotropy parameter, the angle $\Delta(s', \theta', \theta)$ has been

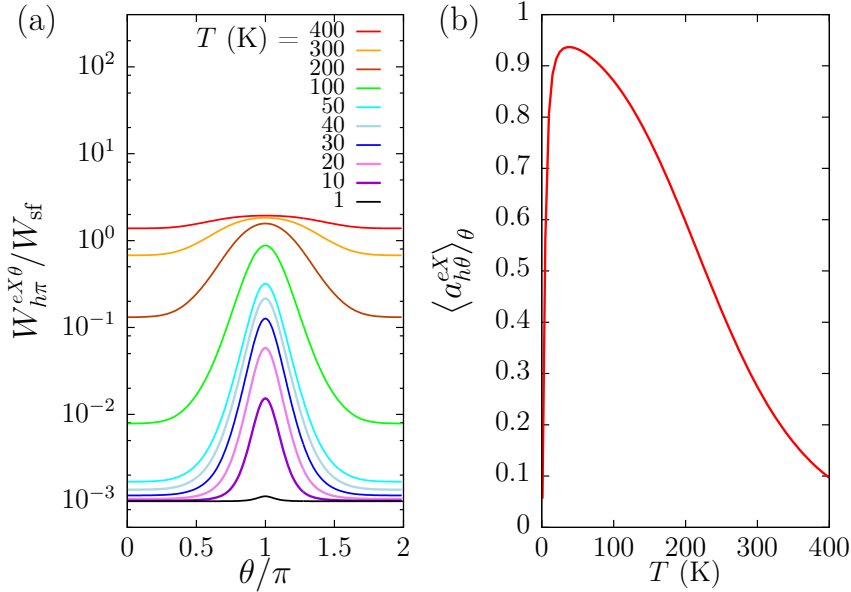


Figure 4.4: (a) Scattering rate at different temperatures for an electron in state $|h, \pi\rangle$ on the hole pocket scattered to the state $|eX, \theta\rangle$ on the electron pocket eX , as a function of the final-state angle θ . (b) Temperature dependence of the anisotropy parameter averaged over all angles θ for the scattering rate shown in panel (a). The parameters have been set to $\xi = 1$, $n = 2.08$, and $W_{\text{imp}}/W_{\text{sf}} = 10^{-3}$. After Ref. [18].

set approximately to $\theta' - \theta$. Finally, Eq. (4.8) is solved numerically by matrix inversion. The numerical results will be compared to the AA, which is given by inserting the lifetimes and the anisotropy parameters into Eqs. (4.12)–(4.14).

4.4.1 Scattering rate

Figure 4.4(a) shows the temperature dependence of the scattering rate for $\xi = 1$ and $W_{\text{imp}}/W_{\text{sf}} = 10^{-3}$. While at high temperatures the scattering rate is isotropic, at lower temperatures a peak due to spin fluctuations develops corresponding to scattering vectors close to \mathbf{Q}_X or \mathbf{Q}_Y . The peak becomes sharper as the temperature is lowered so that the scattering anisotropy increases. At very low temperatures spin fluctuations freeze out and only the isotropic impurity scattering remains so that the anisotropy vanishes again. In Fig. 4.4(b) we plot the anisotropy parameter corresponding to the scattering rate shown in Fig. 4.4(a), averaged over the Fermi pocket. It clearly exhibits the increase for decreasing temperature and the final sharp downturn at very low temperatures. Note that in real pnictides this low-temperature behavior will in most cases be preempted by antiferromagnetic or

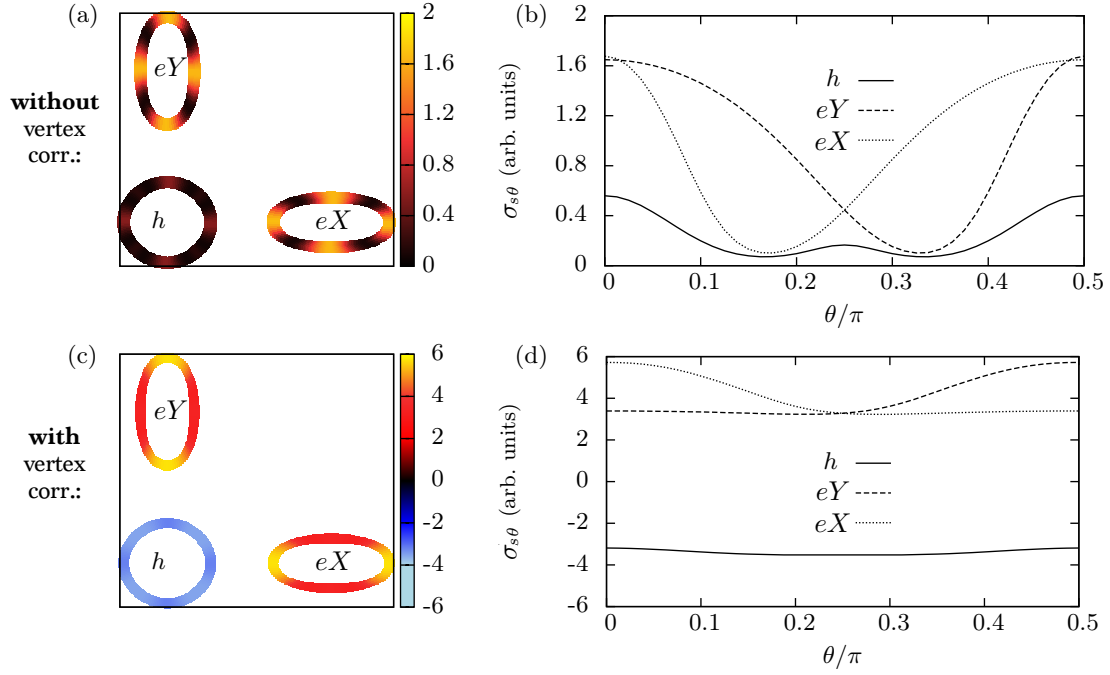


Figure 4.5: Contributions to the conductivity of states on the Fermi surface. Panels (a) and (b) show the Drude result (for which vertex corrections are neglected) as a color map and as a line plot along a quarter of the Fermi pockets, respectively. Note the reduction of the conductivity in the hot regions. Panels (c) and (d) show the same for the full numerical results (which include vertex corrections). The large anisotropy leads to negative conductivity from the hole pocket. No signatures of hot spots are apparent. The parameters are $\xi = 2.5$, $n = 2.08$, $T = 1$ K, and $W_{\text{imp}}/W_{\text{sf}} = 0$. After Ref. [18].

superconducting order, which are not described by our model spin susceptibility.

4.4.2 Hot-spot picture

In this subsection we will explore one of the most interesting results of this chapter. Choosing $T = 1$ K and $W_{\text{imp}}/W_{\text{sf}} = 0$, we focus on the regime of strong spin fluctuations with strong scattering anisotropy, where the difference between the Drude and the full result is the most striking.

We consider the state-resolved conductivity averaged over the directions of the electric field,

$$\sigma_{s\theta} \equiv e^2 N_{s\theta} \frac{v_{s\theta}^x \Lambda_{s\theta}^x + v_{s\theta}^y \Lambda_{s\theta}^y}{2}, \quad (4.25)$$

defined such that the total conductivity is $\sigma = \sum_s \int (d\theta/2\pi) \sigma_{s\theta}$. Figure 4.5 shows

the contributions $\sigma_{s\theta}$ resulting from the Drude approximation as well as from the full numerical calculation. The two are completely different. Most prominently, the hot-spot picture [3, 53, 58, 88] is no longer valid if forward-scattering corrections are taken into account. As discussed above, the scattering off spin fluctuations is strongest in the hot regions since the spin susceptibility is peaked at \mathbf{Q}_X and \mathbf{Q}_Y , see Fig. 4.1. Thus the lifetimes are shorter and the Drude MFP, $\Lambda_{s\theta}^D = \tau_{s\theta} \mathbf{v}_{s\theta}$ are smaller. This is indeed reflected by the suppressed conductivity in the hot regions shown in Figs. 4.5(a) and 4.5(b). However, no signatures of hot regions are seen in the full results in Figs. 4.5(c) and 4.5(d). This is due to the anisotropy of the scattering rate. In the hot regions, the anisotropy $a_{s\theta}'$ is enhanced relative to the cold regions which according to Eqs. (4.12)–(4.14) leads to an enhancement of the MFP, as was discussed in section 4.3. Thus the reduction of the lifetimes is compensated by the enhanced scattering anisotropy and the conductivity of the hot regions is comparable to that of other parts of the pockets, i.e., the short-circuiting of the hot spots does not occur.

Figure 4.5 also shows that the holes contribute negatively to the total conductivity in the full calculation. This corresponds to negative transport times discussed in chapter 3. For the set of parameters chosen in Fig. 4.5, the scattering anisotropy averaged over all Fermi states is close to unity, $\langle a \rangle_\theta = 0.96$. As discussed in section 4.3, such a huge anisotropy leads to a relaxation time that is much longer than the lifetime. In effect, during the relaxation, an electron initially on the hole pocket scatters multiple times between states on the hole pocket and states on the electron pockets at nearly the same polar angle θ . The velocities on the electron and hole pocket are nearly opposite. Since there are more states on the electron pockets and, as we see in Fig. 4.5(a) and (b), the lifetime on the electron pocket is larger, the electron spends the larger part of the relaxation time on the electron pockets. The electron thus on average drifts in the opposite direction to what one would get if it stayed on the hole pocket.

4.4.3 Transport coefficients

The transport coefficients can be obtained from the MFP. The conductivity tensor is given by

$$\sigma^{ij} = e^2 \sum_s \int \frac{d\theta}{2\pi} N_{s\theta} v_{s\theta}^i \Lambda_{s\theta}^j, \quad (4.26)$$

while the thermoelectric tensor reads [90]

$$\alpha^{ij} = -\frac{\pi^2 k_B^2 T}{3e} \frac{\partial \sigma^{ij}}{\partial \mu}. \quad (4.27)$$

We will focus on the resistivity

$$\rho = \frac{1}{\sigma^{xx}}, \quad (4.28)$$

the Hall coefficient

$$R_H = \frac{\sigma^{xy}}{(\sigma^{xx})^2 B}, \quad (4.29)$$

the Seebeck coefficient (thermopower)

$$S = -\frac{\alpha^{xx}}{\sigma^{xx}}, \quad (4.30)$$

and the Nernst coefficient

$$\mathcal{N} = \frac{\sigma^{xy} \alpha^{xx} - \sigma^{xx} \alpha^{xy}}{(\sigma^{xx})^2 B}. \quad (4.31)$$

We give the resistivity in units of

$$\rho_0 \equiv \frac{\hbar}{e^2} \frac{\hbar W_{\text{sf}}}{\mathcal{V}_0} \times 10^{-2} (\text{eV})^2, \quad (4.32)$$

where \mathcal{V}_0 is the volume of the unit cell, and the Nernst coefficient in units of

$$\mathcal{N}_0 \equiv \frac{\mathcal{V}_0}{e \rho_0} \times 10^{-5} \text{ V/K}. \quad (4.33)$$

For the scattering-strength ratio we choose in the following $W_{\text{imp}}/W_{\text{sf}} = 10^{-3}$.

Comparison of approximations

Figure 4.6 shows the temperature dependence of the transport coefficients, comparing the full numerical results with the Drude approximation and with the AA. We see that the Drude approximation results tend to coincide with the full calculation only at very high and very low temperatures, where the scattering is nearly isotropic, see Fig. 4.4. In the temperature range with strong anisotropy (20–150 K) the deviations from the Drude approximation are huge. On the other hand, the AA shows qualitative agreement with the full results over all temperatures and for both ellipticities. The agreement is even quantitative for the resistivity. It

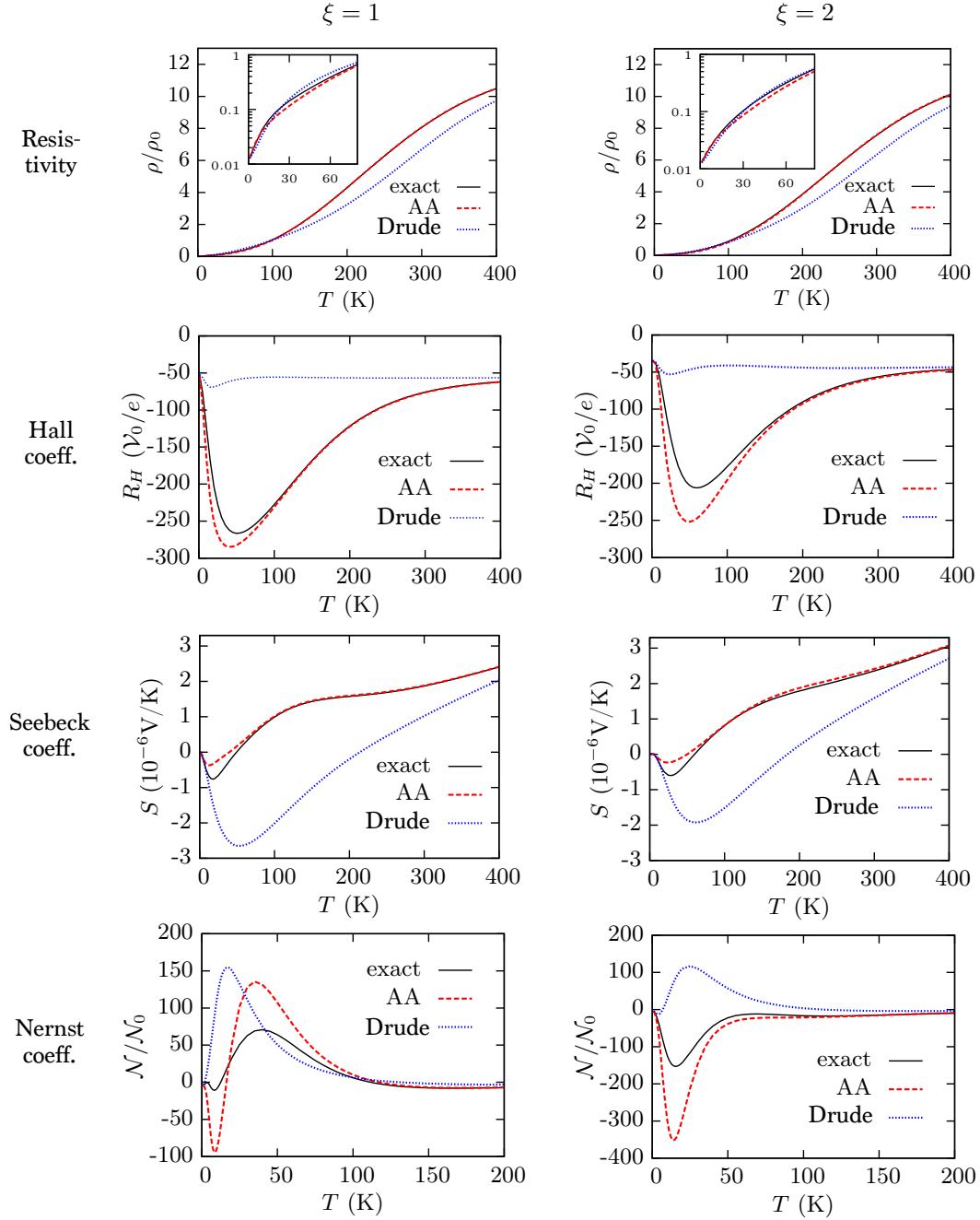


Figure 4.6: Temperature dependence of transport coefficients for filling $n = 2.05$ and ellipticity parameters $\xi = 1$ and $\xi = 2$, calculated with three different methods: Numerically (“exact”), semianalytically within the anisotropy approximation (“AA”) of Eqs. (4.12)–(4.14), and within the Drude approximation, Eq. (2.15), which consists of neglecting vertex corrections. After Ref. [18].

is the worst for the Nernst coefficient \mathcal{N} but even here the positive and negative extrema in \mathcal{N} are predicted by the AA close to the correct temperatures. For $\xi = 1$ the AA is slightly better than for $\xi = 2$ since the former value leads to less eccentric electron pockets. The close agreement between the AA and the full numerical results shows that the transport behavior does not sensitively depend on the precise details of the anisotropic scattering and thus justifies our use of the approximate susceptibility in Eq. (4.3).

Both the Drude approximation and the full results show strong temperature dependence. For the Drude approximation, this can be traced back to the non-trivial geometry of the Fermi pockets leading to the emergent hot-spot structure for temperatures around 100 K due to the high scattering anisotropies for this temperatures (cf. Fig. 4.4). However, as discussed in subsection 4.4.2, forward-scattering corrections invalidate the hot-spot picture for strong anisotropies. The temperature dependence of the Drude approximation results thus stems from the wrong origin. The true temperature dependence can be understood on the basis of the AA, which gives qualitatively correct results. Here, it is due to the strong temperature dependence of the anisotropy parameters $a_{s\theta}^{s'}$ shown in Fig. 4.4(b), i.e., it relies on the *corrections* to the Drude approximation in Eqs. (4.12)–(4.14).

The differences between the Drude approximation and the full results for the resistivity and the Hall coefficient are consistent with our considerations in chapter 3 for two circular Fermi pockets. In the resistivity, we note that the expected enhancement and reduction for high and low scattering anisotropies, respectively, lead to a more pronounced change of slope compared to the Drude approximation.

The enhancement of the Hall coefficient discussed in chapter 3 is also present [17, 54]. However, the extremum of the Hall coefficient in Fig. 4.6 is due to the maximum in the scattering anisotropy (cf. Fig. 4.4) and is thus of different origin than in chapter 3, where a maximum in the Hall coefficient was predicted for the case that the anisotropy crosses a characteristic anisotropy level a^{**} . We do not see any signatures of such a crossing in the present results.

For the thermoelectric effects, Fig. 4.6 shows that the Drude approximation results are even qualitatively incorrect, with the Seebeck and Nernst coefficients showing the wrong sign in the temperature range with strong scattering anisotropy. According to Eqs. (4.27) and (4.30), the Seebeck coefficient S is proportional to $\partial \ln \sigma^{xx} / \partial \mu = -\partial \ln \rho / \partial \mu$. In the Drude approximation, it stems from the shift of the hot spots with the chemical potential, i.e., with doping. In the full results and the AA, it is instead due to the change in the anisotropy parameters $a_{s\theta}^{s'}$

with the chemical potential. Figure 4.6 shows that for the chosen parameters, the two effects contribute to S with opposite sign. The full results for the Nernst coefficient \mathcal{N} change sign between the ellipticities $\xi = 1$ and $\xi = 2$. This effect is missed by the Drude approximation. We return to the Nernst coefficient below.

Qualitative differences between the Drude approximation and the full solution of the Boltzmann equation have also been reported for single-band cuprate models with strongly anisotropic scattering [13, 90]. The physics discussed here, including the inverted MFP of minority carriers and the contribution of hot spots to the transport, is qualitatively different though. These novel effects rely on the presence of multiple bands and Fermi pockets.

Doping dependence

We now turn to the doping dependence of the transport coefficients. Figures 4.7(a)–(d) show the full numerical solutions at different fillings, while Fig. 4.7(e) shows the conductivity of states on Fermi pockets (cf. Fig. 4.5) at the two temperatures $T = 100$ K and $T = 400$ K with strong and weak scattering anisotropy, respectively. Note that the conductivity of the hole pocket is negative for $T = 100$ K and $n \gtrsim 1.99$, i.e., towards the electron-doped side. On the hole-doped side the Drude MFPs of the holes is larger and, according to Eqs. (4.12)–(4.12), higher scattering anisotropy is required to invert the full MFP. The anisotropy, however, is low due to the large discrepancy in size between the electron and hole pockets.

At high temperatures, the transport coefficients all show a smooth doping dependence resulting from the change in the FSs and velocities in the presence of mostly isotropic scattering. In the intermediate temperature range, where anisotropic scattering is strong, this is overlaid by nontrivial doping dependence due to the forward-scattering corrections.

The resistivity around $T \approx 100$ K is largest for intermediate fillings, for which the Fermi pockets are well nested. This is because the narrow peaks in the spin susceptibilities at \mathbf{Q}_X and \mathbf{Q}_Y lead to efficient scattering only for nested Fermi pockets. The inefficiency of anisotropic scattering for small and large n causes a rapid decrease in the resistivity with doping, as shown in the inset in Fig. 4.7(a). Note that the *relative* change in ρ with doping is much larger here than at high temperatures. Since the Seebeck coefficient S is proportional to $\partial \ln \sigma^{xx} / \partial \mu = -\partial \ln \rho / \partial \mu = -\rho^{-1} \partial \rho / \partial \mu$, it is sensitive to this relative change in ρ with μ or n and is, therefore, strongly enhanced in the intermediate temperature range with strong scattering anisotropy, as Fig. 4.7(c) clearly shows.

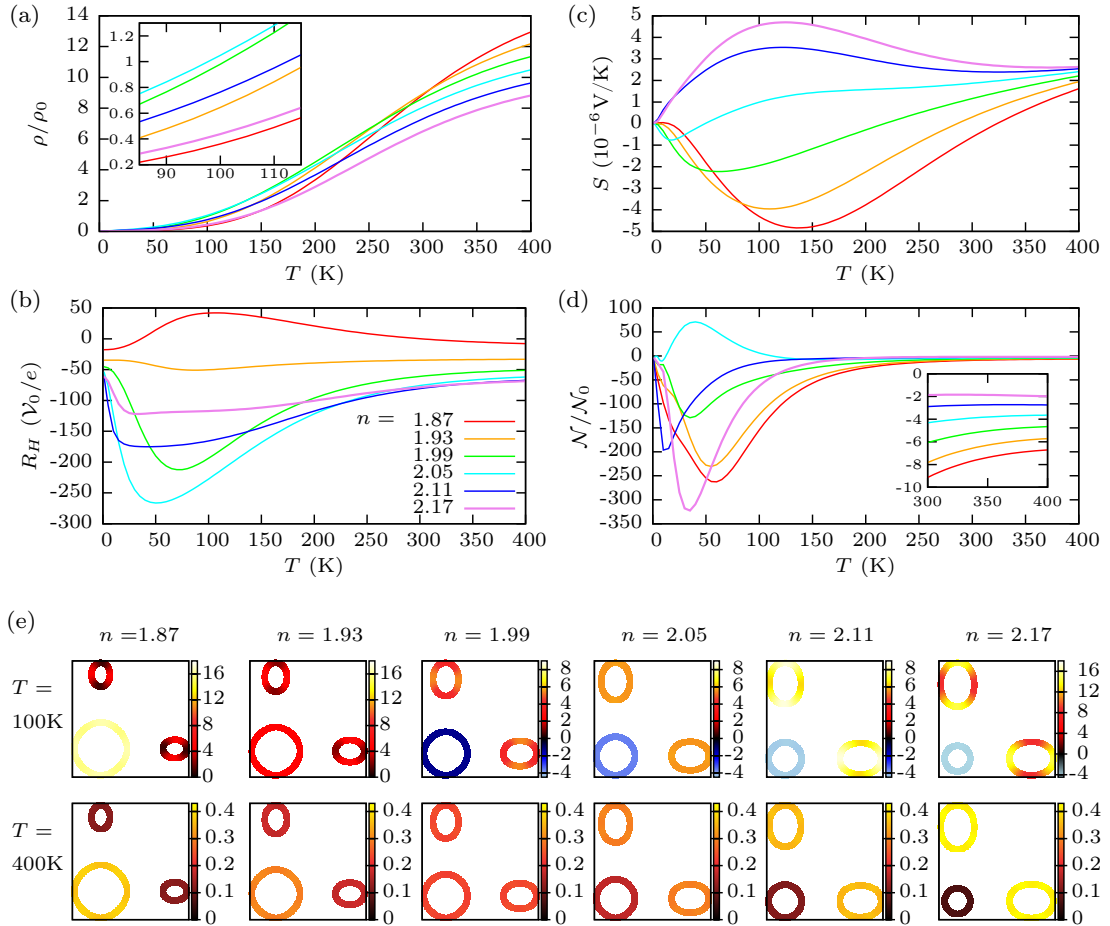


Figure 4.7: (a) Resistivity, (b) Hall coefficient, (c) Seebeck coefficient, and (d) Nernst coefficient as functions of temperature for different fillings n . (e) State-resolved conductivity (in arbitrary units) for $T = 100$ K and $T = 400$ K for all fillings considered. Note the different color scales used in different panels. From Ref. [18].

For the Hall coefficient R_H , Fig. 4.7(b), one would naively expect the largest and smallest values for the most strongly hole-doped and electron-doped cases, respectively, since electrons and holes contribute with opposite signs. This is indeed the case at $T \approx 400$ K, where the scattering is nearly isotropic and no negative conductivities occur. At $T \approx 100$ K, however, Fig. 4.7(b) shows a strong negative enhancement of R_H for intermediate filling. According to Fig. 4.7(e), the contribution of the holes to the total conductivity is negative in this range. In the semiclassical picture this means that the holes drift in the same direction as the electrons, reducing the charge current. Irrespective of that, the magnetic field deflects the holes and the electrons in the same direction. Hence, the inverted sign of the hole contribution reduces the conductivity without changing the Hall voltage. This gives rise to an enhancement of the Hall coefficient defined as the Hall voltage relative to the charge current.

The Nernst coefficient \mathcal{N} plotted in Fig. 4.7(d) is highly sensitive to small doping changes and also, as is evident from Fig. 4.6, to changes in the band parameters. Equations (4.27)–(4.29) and (4.31) show that

$$\mathcal{N} = \frac{3e}{\pi^2 k_B^2 T} \frac{\partial}{\partial \mu} \frac{R_H}{\rho} = \frac{3e}{\pi^2 k_B^2 T} \frac{\partial n}{\partial \mu} \frac{\partial}{\partial n} \frac{R_H}{\rho}. \quad (4.34)$$

The Nernst coefficient is thus sensitive to the nonmonotonic doping dependence of both ρ and R_H . For the cases we have considered, the contributions from ρ and R_H usually counteract each other. The complicated behavior of \mathcal{N} , for example the different sign of \mathcal{N} for $n = 2.05$ compared to the other fillings, is thus due to the quantitative competition of the doping dependences of ρ and R_H and not to any clear qualitative features in the FSs or the scattering. This suggests that the other coefficients might be more advantageous as probes of the electronic system. However, the detailed comparison of experimental transport coefficients and calculations for realistic models remains work for the future.

4.5 Conclusions

In this chapter we have found that the significant contribution of hot spots to the transport and the occurrence of negative conductivity contributions are the main features that distinguish the transport properties of pnictides from the previously considered one-band systems with similarly anisotropic scattering due to spin fluctuations [13, 14, 87]. This is in accordance with the differences found in transport

measurements. Some of the transport coefficients calculated in this chapter show qualitative agreement with experiments [3, 58, 88, 91–95]. However, calculations of transport coefficients for more realistic pnictide models are necessary to allow quantitative predictions.

The most surprising result of this chapter is that the hot spots are *not* short circuited by the cold regions of the Fermi pockets even for very strong scattering, which is in stark contrast to the situation in cuprates and heavy fermions [14, 87]. The enhanced scattering rate in the hot regions indeed leads to short lifetimes in the hot regions, but this effect is balanced by the enhanced MFP due to the anisotropic scattering. This breakdown of the concept of hot and cold regions is not found in a simple Drude approximation neglecting vertex corrections. In the next chapter we will see that in the nematic phase the unusual contribution of hot spots can explain the strong resistive anisotropy.

5 Resistive anisotropy in the nematic phase of iron pnictides

In this chapter we will consider the resistive anisotropy in the *nematic phase* of iron pnictides. The obtained results will offer insights into the origin of the nematic phase, which is currently one of the most intensively discussed topics in the field of high- T_c superconductivity [33, 38]. We will find that scattering due to spin fluctuations can explain the characteristic behavior of the anisotropy upon doping and annealing of samples. The unusual contribution of hot spots, which I have discussed in the previous chapter, turns out to be a crucial ingredient to explain the resistive anisotropy. Parts of this chapter have been published in Ref. [19].

5.1 Introduction

The nematic phase transition occurs at temperatures T_s above or coinciding with the magnetic ordering temperature T_N , at which the SDW state with ordering vector $\mathbf{Q}_X = (\pi, 0)$ or $\mathbf{Q}_Y = (0, \pi)$ is established (cf. the schematic phase diagram in Fig. 1.2(a)). Let the corresponding order parameters be Δ_X and Δ_Y . The nematic phase found for $T_N < T < T_s$ is characterized by a broken rotational symmetry between the x - and y -directions but no magnetic order, i.e., $\langle \Delta_{X,Y} \rangle = 0$. It is generally believed that the nematic state arises from electronic correlations [2]. A careful analysis within the Ginzburg-Landau theory of the terms in the free energy which are biquadratic in the two magnetic order parameters shows that the system might be unstable towards a state with broken symmetry of the magnetic fluctuation spectrum [37]. The nematic order parameter is thus $\phi \propto \langle \Delta_X^2 \rangle - \langle \Delta_Y^2 \rangle$. The broken symmetry of magnetic fluctuations in the nematic phase has recently been observed experimentally [62]. However, it is still under debate whether the primary driving force of the nematic instability are magnetic or orbital fluctuations [37, 45, 96–98].

The principal experimental signature of the electronic nature of the nematic phase is the pronounced difference between the resistivities along the x - and y -directions, $\Delta\rho \equiv (\rho_y - \rho_x)/\rho_x$ [2, 58, 99–101]. Understanding the origin of the resistive anisotropy should offer crucial insights into the origin of the nematicity. Two scenarios are debated: (i) the scattering off anisotropic impurity states [99, 102–105] and (ii) the scattering off fluctuating collective excitations with spectrum reflecting the underlying nematicity [19, 53, 58].

The existing descriptions of the resistive anisotropy due to spin fluctuations [53], i.e., within scenario (ii), are restricted to the limit of weak spin-fluctuation scattering compared to isotropic impurity scattering, although the former is likely stronger than the latter, except at very low temperatures when the spin fluctuations are frozen out [17, 18, 54, 85, 106]. Naturally, this limit is only compatible with small values of $\Delta\rho$, since the dominant impurity part leads to isotropic resistivity. Though in disagreement with the huge positive anisotropy up to $\Delta\rho \approx 0.5$ observed in experiments on electron-doped samples [2, 99], the theory correctly predicts negative $\Delta\rho$ for hole-doped samples [58].

Within scenario (i), the much larger $\Delta\rho$ in electron-doped $\text{Ba}(\text{Fe}_{1-x}\text{Co}_x)_2\text{As}_2$ [2] compared to hole-doped $\text{Ba}_{1-x}\text{K}_x\text{Fe}_2\text{As}_2$ [58, 101] is explained as a consequence of the stronger scattering off Co dopands placed *within* the iron plane [99, 102, 105]. The observed anisotropic impurity states are all elongated in the x -direction, hence giving a larger scattering cross section in the y -direction [102]. The negative $\Delta\rho$ measured for hole-doped samples then arises due to details of the band structure [105]. The dependence of $\Delta\rho$ on the degree of disorder is controversial: some experiments show, in agreement with scenario (i), a reduction of $\Delta\rho$ upon sample annealing, which is supposed to lower the degree of disorder [99], while others report a much weaker disorder dependence [100].

In this chapter, we consider scenario (ii) with spin-fluctuation scattering of arbitrary strength. For spin-fluctuation and isotropic impurity scattering of comparable strength, we will reproduce both the small negative $\Delta\rho$ for hole-doped samples and the large positive $\Delta\rho$ in electron-doped samples. We also show that the reduction of $\Delta\rho$ in electron-doped samples upon annealing is consistent with the spin-fluctuation scenario. In a nutshell, our results follow from the role of the spin-fluctuation scattering strength in controlling the size of the Fermi-surface regions that contribute to the resistive anisotropy.

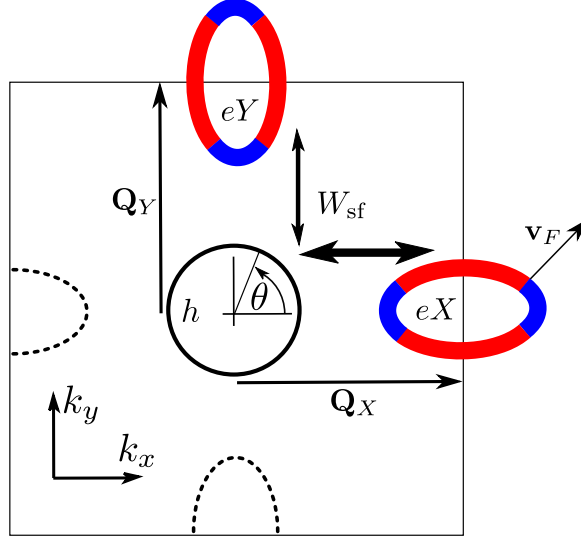


Figure 5.1: Hole (h) and electron (eX and eY) Fermi pockets of the two-band model. In the nematic phase, scattering between h and eX is stronger than between h and eY , as indicated by the arrows marked W_{sf} , giving rise to the resistive anisotropy. As discussed in the main text, the electron pockets can be divided into regions that contribute positively (red) or negatively (blue) to the anisotropy, depending on the direction of the Fermi velocity. States on each FS are parametrized by the angle θ to the x -axis with respect to the center of the pocket. From Ref. [19].

5.2 Model

The band structure we will use is based on the effective two-dimensional model introduced in chapter 4. However, the increased (decreased) iron-iron separation along the x - (y -) axis in the nematic state with $\phi > 0$ reduces (enlarges) the onsite energy of the iron d_{xz} (d_{yz}) orbital [107, 108]. To model the resulting changes in our band structure, we follow Ref. [33] and reduce the size of the eX pocket, enlarge the size of the eY pocket, and elongate the hole pocket along the x direction. This distortion is motivated by the orbital composition of the Fermi pockets [109]. We implement the distortion by introducing a parameter $\delta > 0$ in the dispersion relations in Eqs. (4.1) and (4.2) for the two bands h and e :

$$\varepsilon_{h\mathbf{k}} = \varepsilon_h - \mu + 2t_h [(1 - \delta) \cos k_x + (1 + \delta) \cos k_y], \quad (5.1)$$

$$\varepsilon_{e\mathbf{k}} = \varepsilon_e - \mu + t_{e,1} \cos k_x \cos k_y - t_{e,2} \xi [(1 + \delta) \cos k_x + (1 - \delta) \cos k_y], \quad (5.2)$$

where length is measured in units of the undistorted iron-iron separation. We use the same dispersion parameters as in Ref. [24] and fix the ellipticity of the electron pockets by choosing $\xi_e = 2$. The Fermi pockets are sketched in Fig. 5.1. The validity of the minimal model for the case of 122 pnictides was discussed in Ref. [58].

We assume transport to be dominated by scattering off spin fluctuations and isotropic impurities. We use a phenomenological model for the susceptibility in the nematic phase that has been employed for calculations in the impurity-dominated regime [53, 60, 61]. Similar to chapter 4, we introduce a total elastic scattering rate between states $|s, \theta\rangle$ on the Fermi pockets, parametrized by the pocket index s and the angle θ , cf. Fig. 4.1(b),

$$W_{s\theta}^{s'\theta'} \equiv (1 - \delta_{bb'})W_{\text{sf}}\alpha \int d\varepsilon' \varepsilon' \frac{\coth \frac{\varepsilon'}{2k_B T} - \tanh \frac{\varepsilon'}{2k_B T}}{\varepsilon'^2 + \omega_{\mathbf{q}}^2} + W_{\text{imp}}, \quad (5.3)$$

where $\omega_{\mathbf{q}} = \Gamma (\xi^{-2} \mp \phi + q_x^2(1 \pm \eta) + q_y^2(1 \mp \eta))$ with $\mathbf{q} = \mathbf{k}(s, \theta, \varepsilon_F) - \mathbf{k}(s', \theta', \varepsilon')$, where the wave vectors are measured from the center of the corresponding Fermi pocket. Further, b (b') is the band giving rise to the Fermi pocket s (s'), ξ is the correlation length in the isotropic phase, Γ is the Landau damping parameter, and η is the in-plane anisotropy of the correlation length. The upper (lower) sign corresponds to the scattering between the hole pocket and the electron pocket eX (eY). W_{sf} and W_{imp} represent the overall strengths of the scattering off spin fluctuations and impurities, respectively, and the numerical factor $\alpha = 10$ ensures that at the highest considered temperature (see below) $W_{\text{sf}}/W_{\text{imp}}$ is of the same order as the inverse ratio of average lifetimes due to scattering off spin fluctuations and impurities only, $W_{\text{sf}}/W_{\text{imp}} \sim \tau_{\text{imp}}/\tau_{\text{sf}}$.

As in the paramagnetic phase discussed in chapter 4, the susceptibility entering Eq. (5.3) is peaked at the nesting vectors \mathbf{Q}_X and \mathbf{Q}_Y . In the nematic phase, however, a finite order parameter $\phi > 0$ enhances the peak at \mathbf{Q}_X in the susceptibility, leading to stronger scattering between the hole pocket h and the electron pocket eX than between the pockets h and eY , as indicated in Fig. 5.1.

We focus on the dependence of the resistive anisotropy on doping (electron filling n) and on the relative strengths of spin-fluctuation and impurity scattering, controlled by $W_{\text{sf}}/W_{\text{imp}}$. The explicit temperature T in Eq. (5.3) controls the energy available for spin excitations and thus additionally affects the strength of spin-fluctuation scattering. In the relevant limit $k_B T \ll \omega_{\mathbf{q}}$, this leads to the familiar T^2 dependence. Since the nematic phase appears in a narrow temperature

interval above the Néel temperature $T_N(n)$ we choose the temperature $T(n) = T_N(n) = T_0 (1 - [(n - 2.09)/0.2]^2)$ with $T_0 = \max[T_N(n)] = 137$ K. This mimics the situation in 122 pnictides, where the magnetic order is suppressed upon doping the parent compound (see Fig. 1.2(a)), here taken to correspond to $n = 2.09$ [24]. Our results are qualitatively insensitive to the specific form of $T(n)$. Since the temperature tracks $T_N(n)$, it is reasonable to keep the parameters ξ , ϕ , and Γ fixed; we have checked that the qualitative behavior does not depend on their precise values.

5.3 Resistive anisotropy

To calculate the resistivity we solve the Boltzmann equation

$$\mathbf{\Lambda}_{s\theta} = \tau_{s\theta} \mathbf{v}_{s\theta} + \tau_{s\theta} \sum_{s'} \int \frac{d\theta'}{2\pi} N_{s'\theta'} W_{s\theta}^{s'\theta'} \mathbf{\Lambda}_{s'\theta'} \quad (5.4)$$

numerically, similar to chapter 4. The resistivity ρ_i in the direction $i = x, y$ is determined by the MFP,

$$\rho_i = \left(e^2 \sum_s \int \frac{d\theta}{2\pi} N_{s\theta} v_{s\theta}^i \Lambda_{s\theta}^i \right)^{-1} \equiv \left(\sum_s \int \frac{d\theta}{2\pi} \sigma_{s\theta}^i \right)^{-1}, \quad (5.5)$$

where $\sigma_{s\theta}^i$ is the contribution of the state $|s, \theta\rangle$ to the total conductivity $\sigma^i = \sum_s \int \frac{d\theta}{2\pi} \sigma_{s\theta}^i$. It is useful to decompose the resistive anisotropy into band and angular contributions,

$$\Delta\rho = \int \frac{d\theta}{2\pi} (\Delta\rho_{h\theta} + \Delta\rho_{e\theta}), \quad (5.6)$$

where the contributions from hole and electron pockets read, respectively,

$$\Delta\rho_{h\theta} \equiv \frac{1}{2\sigma^y} (\sigma_{h,\theta}^x - \sigma_{h,\theta}^y + \sigma_{h,\theta+\pi/2}^x - \sigma_{h,\theta+\pi/2}^y), \quad (5.7)$$

$$\Delta\rho_{e\theta} \equiv \frac{1}{\sigma^y} (\sigma_{eY,\theta}^x - \sigma_{eY,\theta}^y + \sigma_{eX,\theta+\pi/2}^x - \sigma_{eX,\theta+\pi/2}^y). \quad (5.8)$$

In Eq. (5.7), we consider the contributions from the hole-pocket states $|h, \theta\rangle$ and $|h, \theta + \pi/2\rangle$ together, since only the joint contribution vanishes in the paramagnetic, C_4 -symmetric phase and is thus a good measure of the state-resolved contributions to the resistive anisotropy. For the same reason, the states $|eY, \theta\rangle$ and $|eX, \theta + \pi/2\rangle$ are considered together in Eq. (5.8). According to the definition of $\Delta\rho_{e\theta}$, the contributions from states close to the minor axis of the elliptical

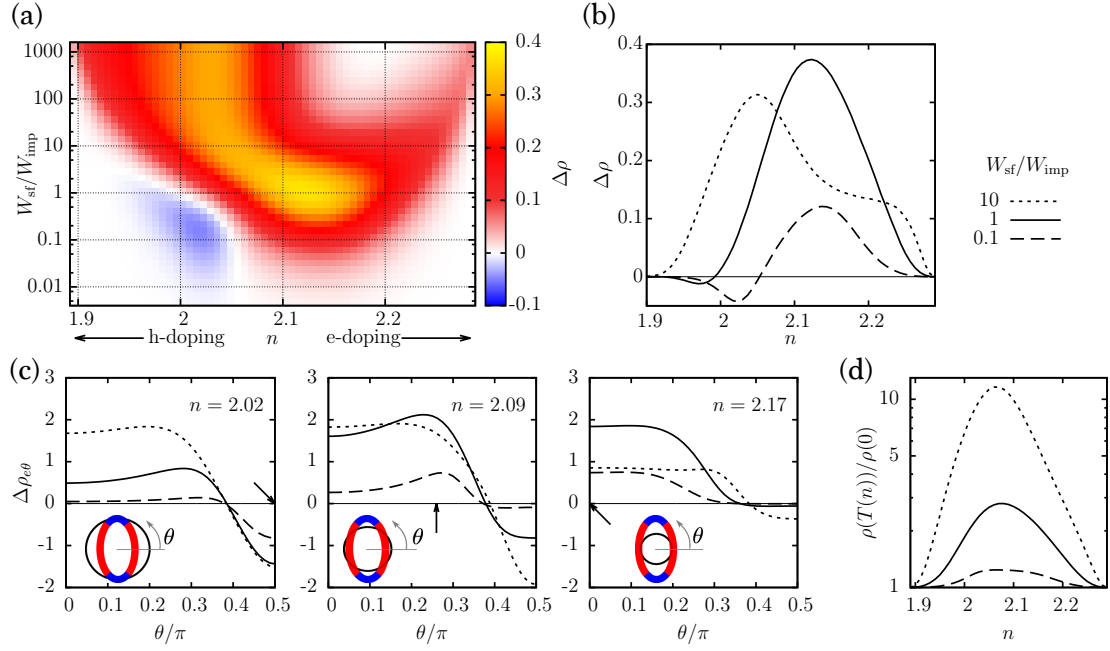


Figure 5.2: (a) Resistive anisotropy as a function of doping (parametrized by n) and of the relative strengths of spin-fluctuation and impurity scattering. (b) Resistive anisotropy as a function of doping for $W_{sf}/W_{imp} = 0.1, 1,$ and 10 . (c) Angle-resolved contributions of the electron pockets to the resistive anisotropy as defined in Eq. (5.8). While for $W_{sf}/W_{imp} = 0.1$ only regions close to the hot spots (indicated by arrows) contribute, for increasing W_{sf}/W_{imp} the contributing regions grow. (d) Ratio of averaged resistivities at the temperatures $T(n)$ considered in panels (a)–(c) and at $T = 0$ K. We choose the parameters $\eta = 0.5$, $\Gamma = 350$ meV, $\xi^{-2} = 0.027$, and $\phi = 0.017$. From Ref. [19].

electron pockets are found at $\theta \approx 0$, while the contributions from states close to the major axis are found at $\theta \approx \pi/2$.

5.3.1 Vanishing orbital splitting

We now focus on the resistive anisotropy resulting from the anisotropic spin-fluctuation spectrum alone and include the orbital splitting in the next subsection. Figure 5.2 summarizes the results for the resistive anisotropy for $\delta = 0$. In Fig. 5.2(a) the resistive anisotropy is plotted as a function of doping and the ratio W_{sf}/W_{imp} , while in Fig. 5.2(b) the doping dependence is illustrated for three characteristic values of W_{sf}/W_{imp} . The contributions $\Delta\rho_{e\theta}$ from the electron pockets are found to dominate the anisotropy, for which reason only these contributions

are shown in Fig. 5.2(c). As evident from Fig. 5.2(c) and illustrated in Fig. 5.1, the electron pockets can be divided into positively and negatively contributing parts, with the crossover located roughly where the Fermi velocity points in the diagonal direction; the parts close to the minor axis of the electron pockets contribute with positive sign, while the parts close to the major axis contribute with negative sign. The crossover is located where the Fermi velocity points in the diagonal direction. This is because the conductivity of the electron pocket eY is larger than that of eX due to the stronger scattering for the latter. Since the velocity of states close to the major axes are pointing in the x -direction for the pocket eX and in the y -direction for the pocket eY , the joint conductivity of these states is larger in the y -direction. Analogously, the joint conductivity of states close to the minor axes is larger in the x -direction.

The total resistive anisotropy in Figs. 5.2(a) and (b) shows a strong doping dependence, which changes qualitatively with $W_{\text{sf}}/W_{\text{imp}}$. The angle-resolved plots in Fig. 5.2(c) show that for increasing $W_{\text{sf}}/W_{\text{imp}}$ the contributing regions of the electron pockets expand. This is schematically illustrated in Fig. 5.3. For small $W_{\text{sf}}/W_{\text{imp}}$, the resistive anisotropy is dominated by regions close to the hot spots, whereas the “cold” regions, where spin-fluctuation scattering is weaker, give small contributions. Since the electron pockets have negatively and positively contributing parts, the position of the hot spots determines the sign of the resistive anisotropy. The negative (positive) extremum is found for the filling $n \approx 2.02$ ($n \approx 2.17$), for which the hot spots lie on the major (minor) axis of the electron pockets. The difference between the positive and negative extrema is due to different velocities and densities of states at the major and minor axes.

In the impurity-dominated limit, $W_{\text{sf}}/W_{\text{imp}} \ll 1$, the anisotropy is very small as impurity scattering is isotropic. With increasing $W_{\text{sf}}/W_{\text{imp}}$, the contributing regions of the electron pockets expand and the extrema of $\Delta\rho$ grow, until the active region starts to include parts contributing with the opposite sign. Upon further expansion, the positive and negative contributions begin to partially compensate each other. Since the negatively contributing regions are smaller, the negative extremum of $\Delta\rho$ is suppressed at a smaller ratio $W_{\text{sf}}/W_{\text{imp}}$ than the positive extremum. At $W_{\text{sf}}/W_{\text{imp}} \approx 1$ this results in a strong doping asymmetry with small negative values on the hole-doped side and large positive values on the electron-doped side.

We emphasize that the result that the hot spots contribute to $\Delta\rho$ even for dominant spin-fluctuation scattering, as evident from Fig. 5.2(c), is not obvious.

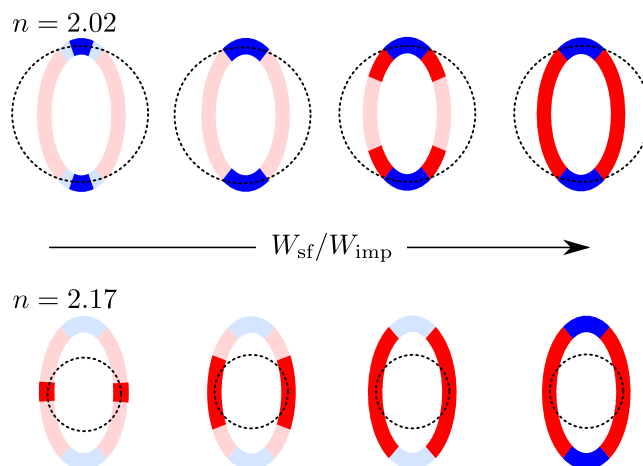


Figure 5.3: Contributing regions (bright colors) of the electron pockets to the resistive anisotropy for increasing strength of spin-fluctuation scattering. The blue-colored and red-colored regions of the electron pockets contribute negatively and positively to the resistive anisotropy, respectively. Two characteristic filling levels are considered, $n \approx 2.02$ and $n \approx 2.17$, with hot spots at the major and the minor axis of the electron pockets, respectively. For dominant impurity scattering, the main contributions come from hot spots. Increasing strength of spin-fluctuation scattering leads to an expansion of the contributing regions. Note that hot spots contribute even for strong spin-fluctuation scattering [18]. From Ref. [19].

Since in this limit the scattering at the hot spots is much stronger than in the cold regions, one would naively expect the hot spots to be short circuited by the cold regions [87], i.e., to be irrelevant for the transport, in which case $\Delta\rho$ would be significantly smaller [53, 58]. However, as we have seen in chapter 4 for the C_4 -symmetric state [18], the short-circuiting is compensated by enhanced forward-scattering corrections.

To compare the results to measurements, we have to identify the relevant range of W_{sf}/W_{imp} . In Fig. 5.2(d), we plot the calculated ratio of the averaged resistivity $\rho(T) \equiv (\rho_x + \rho_y)/2$ at $T = T(n)$ and at $T = 0$ K, where the spin excitations are frozen out and the resistivity is due to impurity scattering alone, which we assume to be temperature independent. Ignoring for the moment that the system is antiferromagnetic at $T = 0$ K, we observe that for $W_{sf}/W_{imp} = 1$ and $W_{sf}/W_{imp} = 10$ the resistivity ratios are comparable to those measured for as-grown and annealed samples, respectively [99]. The reduction of the density of states in the antiferromagnetic phase should increase the $T = 0$ K resistivity, however, and so our

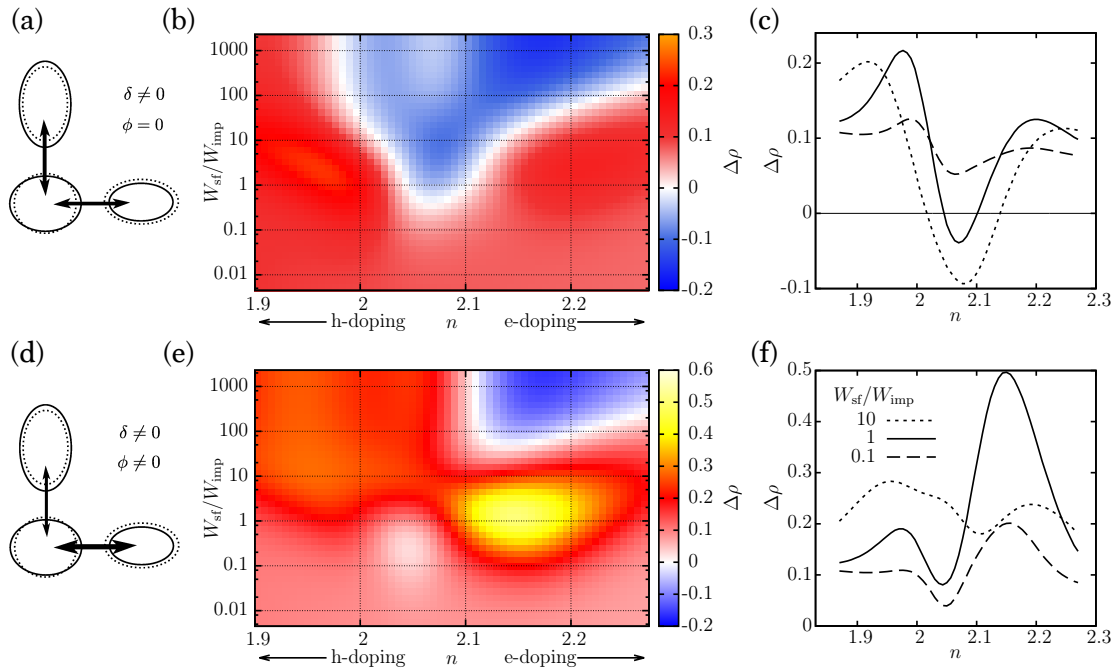


Figure 5.4: (a) Sketch of the Fermi pocket distortion and the scattering strength between the hole and the electron pockets. (b), (c) Resistive anisotropy in the presence of orbital splitting ($\delta = 0.03$) and a paramagnetic spin susceptibility ($\phi = 0$). (d), (e) (f) Same as (a), (b) (c) but for a nematic spin susceptibility ($\phi = 0.017$). After Ref. [19].

argument likely underestimates $W_{\text{sf}}/W_{\text{imp}}$.

For $W_{\text{sf}}/W_{\text{imp}} = 1$, Figs. 5.2(a) and (b) show a large positive peak with $\Delta\rho \approx 0.4$ in electron-doped samples and a small negative peak with $\Delta\rho \approx -0.01$ in hole-doped samples. This is in good agreement with experimental observations [2, 58, 99]. The results also show that in electron-doped samples an increase of $W_{\text{sf}}/W_{\text{imp}}$ beyond about 1 leads to a reduction of the peak value of $\Delta\rho$. A reduction of $\Delta\rho$ upon annealing was indeed observed in electron-doped $\text{Ba}(\text{Fe}_{1-x}\text{Co}_x)_2\text{As}_2$ [99], where this effect has been taken as strong evidence that the resistive anisotropy mainly stems from scattering at anisotropic impurity states. Our results show, however, that such a reduction is also consistent with anisotropic spin-fluctuation scattering. For the hole-doped samples, we predict an *increase* in $\Delta\rho$ with annealing if $W_{\text{sf}}/W_{\text{imp}} \gtrsim 1$, see Figs. 5.2(a) and (b), which to our knowledge has not been measured so far.

5.3.2 Finite orbital splitting

We now investigate the resistive anisotropy for a relatively large orthorhombic distortion of the band structure with $\delta = 0.03$, for which the relative difference of the electron-pocket areas is about 21%. For a nonzero orthorhombic distortion, the model displays a resistive anisotropy $\Delta\rho$ even when the nematic parameter in the susceptibility vanishes, $\phi = 0$. Results for this case are found in Figs. 5.4(b) and (c). The calculated $\Delta\rho$ is in rather poor agreement with experimental findings: neither the minimum near optimal doping nor the significant extent of negative values is observed. Note that while the magnitude of $\Delta\rho$ scales with δ , its qualitative behavior does not change significantly.

Figures 5.4(e) and (f) show the result for the combined effect of orbital splitting ($\delta = 0.03$) and the nematicity in the spin susceptibility ($\phi = 0.017$). The effect of the two sources of anisotropy appear to be additive and the characteristic signatures of the nematic spin fluctuations are still conspicuous. In particular, the large positive anisotropy in electron-doped samples and the much smaller anisotropy in hole-doped samples for $W_{\text{sf}}/W_{\text{imp}} \lesssim 1$ is still present, as is the reduction of the anisotropy in electron-doped samples for $W_{\text{sf}}/W_{\text{imp}} \gtrsim 2$. On the other hand, for $W_{\text{sf}}/W_{\text{imp}} \gg 1$, the weak contribution of the spin fluctuations in the case of electron doping means that the resistive anisotropy is controlled by the distortion of the band structure and becomes negative, as in Fig. 5.2.

5.4 Conclusions

We have shown that the twin puzzles of the doping asymmetry of $\Delta\rho$ and the reduction of $\Delta\rho$ upon annealing can be explained by the recently observed [62] anisotropic spin-fluctuation spectrum alone. The qualitative behavior is governed by the contributing regions on the elliptical electron pockets, in particular their growth with increasing spin-fluctuation strength. Importantly, the hot spots contribute to $\Delta\rho$ even for strong spin-fluctuation scattering, contrary to what was thought previously [53, 58]. Since spin fluctuations are particularly strong at the hot spots, this naturally leads to large anisotropies.

In contrast, the effect of orbital splitting [107, 108] alone cannot account for the observed resistive anisotropy. Better agreement might be achieved for a more sophisticated model of the band structure, although this would be at the expense of fine tuning. Including the nematicity in the spin-fluctuation spectrum gives much better agreement with experimental results, is robust against the distortion

of the band structure, and dominates over the contribution of the distorted band structure to the resistive anisotropy over a large parameter range.

6 Transport in the spin-density-wave phase of iron pnictides

In the preceding chapters we have seen that the multiband nature of iron pnictides gives rise to new phenomena which do not occur in one-band systems such as the extensively studied cuprates. An even larger difference between the two materials classes concerns their magnetic phases. Unlike in cuprates, the magnetic phase in iron pnictides is metallic and thus offers a new field to study the interplay between transport and itinerant magnetism [110, 111]. In this chapter, I will calculate the scattering rate resulting from the interaction of electrons with spin fluctuations, which in the SDW phase include propagating magnons. Most interestingly, we will find that this interaction leads to “interrupted” orbital motion of electrons in the magnetic field with clear signatures in the magnetoresistance.

6.1 Introduction

There has been very few theoretical investigations of transport in the SDW phase of iron pnictides. Specifically, the impact of spin fluctuations has not been considered so far. It has been proposed that some transport anomalies in the SDW phase might be caused by Dirac fermions [47, 112, 113], as the reconstructed bands below T_N show topologically protected Dirac nodes [46, 114, 115]. It has been discussed that the presence of Dirac fermions might explain the positive linear magnetoresistance, i.e., the linear increase of resistivity in the magnetic field [111, 112, 116, 117], in contrast to the quadratic behavior found in conventional metals [74]. An alternative scenario explains the linear magnetoresistance by the large velocity change along the Fermi line of the reconstructed pockets for $T \approx T_N$ [118].

In this chapter, we will see that even more exotic effects than positive linear mag-

netoresistance can occur if the coupling of electrons to spin fluctuations is taken into account. It turns out that spin fluctuations cause strong scattering between different sides of the small reconstructed pockets. In an applied magnetic field, this scattering leads to an interruption of orbital motion—certain points emerge on the Fermi line which can not be passed by electrons moving along the Fermi line (cf. section 2.4 for orbital motion in the magnetic field). The consequences are drastic: A critical magnetic field emerges above which the conductivity tensor is no longer positive definite, indicating that the system becomes thermodynamically unstable [80]. This critical field exists irrespective of the presence of other FSs which contribute to the conductance.

Interruption of orbital motion is also possible if the relaxation time at the hot spots (or hot lines in 3D) is suppressed, as has been discussed in Refs. [118, 119]. The corresponding mechanism is distinct from the one we discuss here. It also has distinct signatures in transport, e.g., a linear magnetoresistance that is positive and non-saturating. In chapter 4 we have seen that in pnictides the relaxation time at hot spots is *not* suppressed however, which undermines the relevance of this mechanism [118, 119].

To explore signatures of interrupted orbital motion, we will study the magnetoresistance of single-domain single crystals as well as of polycrystals and of crystals with twin domains [75]. We will find that in twinned crystals as well as in polycrystals interrupted orbital motion has no special signatures for weak magnetic fields, whereas for strong magnetic fields the resistivity drops to zero. In single crystals the Fermi pockets with interrupted orbital motion give rise to linear magnetoresistance already for weak magnetic fields. Most exotically, the linear magnetoresistance is *negative* for certain directions of the charge current, which makes it a clear signature of the mechanism I propose.

6.2 Model

We study the SDW phase using the effective two-band model introduced in chapters 4 and 5. Following Refs. [24, 55], we use the Hamiltonian

$$\begin{aligned}
 H = & \sum_{A\mathbf{k}\sigma} \varepsilon_{A\mathbf{k}} c_{A\mathbf{k}\sigma}^\dagger c_{A\mathbf{k}\sigma} \\
 & + \frac{1}{2V} \sum_{\mathbf{k}\mathbf{k}'\mathbf{q}} \sum_{\sigma\sigma'} \sum_{ABCD} U_{(AB),(CD)}(\sigma, \sigma') c_{A\mathbf{k}+\mathbf{q}\sigma}^\dagger c_{C\mathbf{k}'-\mathbf{q}\sigma'}^\dagger c_{D\mathbf{k}'\sigma'} c_{B\mathbf{k}\sigma}
 \end{aligned} \tag{6.1}$$

where $\sigma = \pm 1$ denotes the spin and capital letters denote the two bands e and h . The onsite coupling constants read

$$U_{(hh),(hh)}(\sigma, \sigma') = U_{(ee),(ee)}(\sigma, \sigma') = g_1 \delta_{\sigma', -\sigma}, \quad (6.2)$$

$$U_{(he),(he)}(\sigma, \sigma') = U_{(eh),(eh)}(\sigma, \sigma') = g_{2a} \delta_{\sigma', -\sigma}, \quad (6.3)$$

$$U_{(he),(eh)}(\sigma, \sigma') = U_{(eh),(he)}(\sigma, \sigma') = g_{2b}, \quad (6.4)$$

$$U_{(ee),(hh)}(\sigma, \sigma') = U_{(hh),(ee)}(\sigma, \sigma') = g_{cf}. \quad (6.5)$$

The dispersion relations appearing in Eq. (6.1) were defined in Eqs. (4.1) and (4.2),

$$\varepsilon_{h\mathbf{k}} = \varepsilon_h - \mu + 2t_h (\cos k_x a + \cos k_y a), \quad (6.6)$$

$$\varepsilon_{e\mathbf{k}} = \varepsilon_e - \mu + t_{e,1} \cos k_x a \cos k_y a - t_{e,2} \xi (\cos k_x a + \cos k_y a). \quad (6.7)$$

We set the ellipticity of the electron pockets to $\xi = 1$; other parameters are as in chapter 4. It has been shown that this model exhibits a SDW phase around the filling $n = 2.085$ [24]. This is the filling we will consider in the following. Mean-field decoupling the Hamiltonian with the order parameter

$$\Delta \equiv -\frac{g_{cf} + g_{2a}}{2V} \sum_{\mathbf{k}, \sigma} \sigma \langle c_{h\mathbf{k}\sigma}^\dagger c_{e\mathbf{k}+\mathbf{Q}\sigma} \rangle_{\text{MF}}, \quad (6.8)$$

which has to be determined self-consistently, leads to the mean-field Hamiltonian

$$H_{\text{MF}} = \sum'_{\mathbf{k}, \sigma} \mathbf{c}^\dagger(\mathbf{k}\sigma) \begin{pmatrix} \varepsilon_{h\mathbf{k}} & 0 & 0 & \sigma\Delta \\ 0 & \varepsilon_{h\mathbf{k}+\mathbf{Q}} & \sigma\Delta & 0 \\ 0 & \sigma\Delta & \varepsilon_{e\mathbf{k}} & 0 \\ \sigma\Delta & 0 & 0 & \varepsilon_{e\mathbf{k}+\mathbf{Q}} \end{pmatrix} \mathbf{c}(\mathbf{k}\sigma), \quad (6.9)$$

where the primed sum over \mathbf{k} runs only over the reduced Brillouin zone according to the SDW state with ordering vector \mathbf{Q} , which is taken to be $\mathbf{Q} = (\pi, 0)$. In Eq. (6.9) the pseudo-spinor notation,

$$\mathbf{c}^\dagger(\mathbf{k}\sigma) \equiv (c_{h\mathbf{k}\sigma}^\dagger, c_{h\mathbf{k}+\mathbf{Q}\sigma}^\dagger, c_{e\mathbf{k}\sigma}^\dagger, c_{e\mathbf{k}+\mathbf{Q}\sigma}^\dagger), \quad (6.10)$$

was introduced. The mean-field Hamiltonian is diagonalized by the unitary operator

$$\mathcal{U}(\mathbf{k}\sigma) \equiv \begin{pmatrix} -\sigma u(\mathbf{k}) & 0 & 0 & -v(\mathbf{k}) \\ 0 & -\sigma u(\mathbf{k} + \mathbf{Q}) & -v(\mathbf{k} + \mathbf{Q}) & 0 \\ 0 & v(\mathbf{k} + \mathbf{Q}) & -\sigma u(\mathbf{k} + \mathbf{Q}) & 0 \\ v(\mathbf{k}) & 0 & 0 & -\sigma u(\mathbf{k}) \end{pmatrix}, \quad (6.11)$$

where

$$u(\mathbf{k}) = \frac{\epsilon_{eh}^-(\mathbf{k}) - \sqrt{\epsilon_{eh}^-(\mathbf{k})^2 + \Delta^2}}{\sqrt{\Delta^2 + \left(\epsilon_{eh}^-(\mathbf{k}) - \sqrt{\epsilon_{eh}^-(\mathbf{k})^2 + \Delta^2}\right)^2}}, \quad (6.12)$$

$$v(\mathbf{k}) = \frac{\Delta}{\sqrt{\Delta^2 + \left(\epsilon_{eh}^-(\mathbf{k}) - \sqrt{\epsilon_{eh}^-(\mathbf{k})^2 + \Delta^2}\right)^2}}, \quad (6.13)$$

and $\epsilon_{AB}^\pm(\mathbf{k}) \equiv (\varepsilon_{A\mathbf{k}+\mathbf{Q}} \pm \varepsilon_{B\mathbf{k}})/2$. The energy eigenvalues read

$$E_1(\mathbf{k}) = \epsilon_{eh}^+(\mathbf{k}) + \sqrt{\epsilon_{eh}^-(\mathbf{k})^2 + \Delta^2}, \quad (6.14)$$

$$E_2(\mathbf{k}) = \epsilon_{he}^+(\mathbf{k}) + \sqrt{\epsilon_{he}^-(\mathbf{k})^2 + \Delta^2}, \quad (6.15)$$

$$E_3(\mathbf{k}) = \epsilon_{he}^+(\mathbf{k}) - \sqrt{\epsilon_{he}^-(\mathbf{k})^2 + \Delta^2}, \quad (6.16)$$

$$E_4(\mathbf{k}) = \epsilon_{eh}^+(\mathbf{k}) - \sqrt{\epsilon_{eh}^-(\mathbf{k})^2 + \Delta^2}. \quad (6.17)$$

The solution of the mean-field problem determines the ordering temperature T_N for a given set of coupling constants. The four reconstructed bands $E_\mu(\mathbf{k})$ in Eqs. (6.14)–(6.17) (which will be denoted by Greek letters in the following) give rise to Fermi pockets with changed topology in comparison to the paramagnetic state [55, 120]. For the considered filling $n = 2.085$ and elliptical electron pockets ($\xi = 1$), the pocket reconstruction can be visualized as follows: In the magnetic Brillouin zone, which is reduced according to the ordering vector $\mathbf{Q} = (\pi, 0)$ becoming a reciprocal lattice vector, the electron pocket eX is backfolded on top of the hole pocket h (see Fig. 1.2(a)). For temperatures below but close to T_N , the opening of the gap affects only the hot spots, i.e., points at which the electron pocket eX crosses the hole pocket h , resulting in four “banana pockets” (so-called for their crescent-like shape) as shown in Fig. 1.2(a). The electron pocket eY is only weakly affected by the band reconstruction. Lowering the temperature results in

shrinking of the banana pockets, and, eventually, to their pairwise disappearance. The effect on transport of these so-called *Lifshitz transitions* has been studied recently within the same *band* model considered here [120].

It has been pointed out however that in more realistic, *orbital* models at least two of the reconstructed pockets belong to an underlying Dirac spectrum with topologically protected Dirac nodes [46, 114, 115]. The Dirac nodes, which prevent the disappearance of pockets, are absent in the considered band model. Moreover, the two-dimensional density of states of the Dirac bands depends linearly on the Fermi energy, whereas it is constant for parabolic bands. In fact, the disappearance of pockets within our model causes step-like changes of the total density of states, while it is otherwise nearly constant as a function of temperature. These strong qualitative differences between the simplified band model and the more realistic orbital models lead to the conclusion that the band model is not suitable for a study of the *temperature dependence* of transport in the SDW phase. We therefore restrict ourselves to transport at a fixed temperature, which we choose as $T = 0.93 T_N$.

6.3 Spin-fluctuation scattering

We will now calculate the spin-fluctuation spectrum within the mean-field state. For the low-energy transport we can neglect the contribution of the longitudinal susceptibility, which is gapped in the SDW phase, and focus on the transverse spin susceptibility, which includes the contribution of the Goldstone mode [50, 51]. The transverse susceptibility is defined as

$$\begin{aligned}
\chi^{+-}(\mathbf{q}, i\omega_n) &= \sum_{A,B,C,D} \sum_{n,m} \sum_{\mathbf{k},\mathbf{k}'} \int_0^{1/k_B T} d\tau e^{i\omega_n \tau} \\
&\quad \times \langle T_\tau c_{A\mathbf{k}+(\mathbf{q}+n\mathbf{Q})\downarrow}^\dagger(\tau) c_{B\mathbf{k},\uparrow}(\tau) c_{C\mathbf{k}'-(\mathbf{q}+m\mathbf{Q})\uparrow}^\dagger(0) c_{D\mathbf{k}',\downarrow}(0) \rangle \\
&\equiv \sum_{A,B,C,D} \sum_{n,m} \chi_{(A,B,n),(C,D,m)}^{+-}(\mathbf{q}, i\omega_n), \tag{6.18}
\end{aligned}$$

where the sum over $n, m = 0, 1$ is required to include the so-called *umklapp* susceptibilities, which are possible in the SDW phase [50, 51].

Following Refs. [50, 51, 55], we calculate the susceptibility within the random-phase approximation (RPA). It is useful to introduce a matrix notation, in which \hat{M} is a tensor with components $M_{(A,B,n),(C,D,m)}$. The susceptibility tensor has been defined in Eq. (6.18). The Dyson equation for the RPA susceptibility is dia-

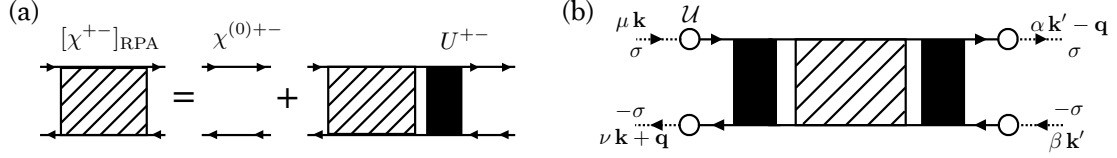


Figure 6.1: (a) Dyson equation for the RPA susceptibility represented by a striped box. The black box depicts the interaction vertex U^{+-} . (b) Spin-fluctuation propagator (striped box) dressed with interaction vertices (black boxes). The circles with dashed and solid legs represent the transformation factors \mathcal{U} between the eigenbasis for the paramagnetic state and the eigenbasis for the mean-field SDW state.

grammatically represented in Fig. 6.1(a). In tensor notation, the Dyson equation reads

$$[\hat{\chi}^{+-}(\mathbf{q}, i\omega_n)]_{\text{RPA}} = \hat{\chi}^{(0)+-}(\mathbf{q}, i\omega_n) + [\hat{\chi}^{+-}(\mathbf{q}, i\omega_n)]_{\text{RPA}} \hat{U}^{+-} \hat{\chi}^{(0)+-}(\mathbf{q}, i\omega_n), \quad (6.19)$$

where

$$U_{(A,B,n),(C,D,m)}^{+-} = U_{(AB),(CD)}(\sigma, -\sigma) \delta_{nm}. \quad (6.20)$$

The bare susceptibility reads

$$\begin{aligned} \chi_{(A,B,n),(C,D,m)}^{(0)+-}(\mathbf{q}, i\omega_n) &= -\frac{k_B T}{V} \sum_{\mathbf{k}, i\nu_n} \sum_{i,j,\nu,\mu} G_{\nu}^{(0)}(\mathbf{k} - \mathbf{q}, i\nu_n - i\omega_n) G_{\mu}^{(0)}(\mathbf{k}, i\nu_n) \\ &\quad \times \mathcal{U}_{(A,i),(\mu)}^*(\mathbf{k}\sigma) \mathcal{U}_{(B,|i-n|),(\nu)}(\mathbf{k} - \mathbf{q} - \sigma) \\ &\quad \times \mathcal{U}_{(C,|j-m|),(\nu)}^*(\mathbf{k} - \mathbf{q} - \sigma) \mathcal{U}_{(D,j),(\mu)}(\mathbf{k}\sigma), \end{aligned} \quad (6.21)$$

where $G_{\mu}^{(0)}(\mathbf{k}, i\nu_n) = (E_{\mu}(\mathbf{k}) - i\nu_n)^{-1}$ is the electron Green's function for the mean-field state. To obtain Eq. (6.21), the unitary transformation defined in Eq. (6.11) has been applied to the ladder operators in Eq. (6.18). The Dyson equation can be readily solved by matrix inversion, giving the result

$$[\hat{\chi}^{+-}(\mathbf{q}, i\omega_n)]_{\text{RPA}} = \hat{\chi}^{(0)+-}(\mathbf{q}, i\omega_n) [\hat{1} - \hat{U}^{+-} \hat{\chi}^{(0)+-}(\mathbf{q}, i\omega_n)]^{-1}. \quad (6.22)$$

In contrast to the paramagnetic phase, in the SDW phase the coupling between the electrons and the spin fluctuations is momentum dependent due to momentum-dependent transformation factors given in Eq. (6.11). The bosonic spin-fluctuation propagator dressed with transformed coupling constants is shown schematically in Fig. 6.1(b). The momentum dependence of the coupling between electrons and

the spin-fluctuation propagator is crucial: Neglecting the momentum dependence would cause diverging forward scattering of electrons, violating Adler's theorem, which states that the coupling of electrons to a Goldstone mode vanishes for zero transferred momentum [121].

The dressed spin-fluctuation propagator, cf. Fig. 6.1(b), reads

$$\begin{aligned}
 S_{(\nu\mu),(\alpha\beta)}(\mathbf{k}, \mathbf{k}'; \sigma, -\sigma; \mathbf{q}, i\omega_n) &= \sum_{j,k,n,m} \sum_{A,B,C,D} \mathcal{U}_{A,j;\nu}^*(\mathbf{k} + \mathbf{q}, -\sigma) \mathcal{U}_{B,|j-n|;\mu}(\mathbf{k}, \sigma) \\
 &\times (\hat{U}^{+-} [\hat{\chi}^{+-}(\mathbf{q}, i\omega_n)]_{\text{RPA}} \hat{U}^{+-})_{(A,B,n),(C,D,m)} \\
 &\times \mathcal{U}_{C,|k-m|;\alpha}^*(\mathbf{k}' - \mathbf{q}\sigma) \mathcal{U}_{D,k;\beta}(\mathbf{k}', -\sigma). \quad (6.23)
 \end{aligned}$$

With that we can readily obtain the scattering rate from the spectral function of the propagator as described in chapter 2 (note that, in contrast to the notation in chapter 2, the propagator in Eq. (6.23) includes the coupling constants),

$$W_{\mu\mathbf{k}\sigma}^{\nu\mathbf{k}+\mathbf{q}-\sigma} = \frac{p_T(\omega)}{\omega} \text{Im} S_{(\nu\mu),(\mu\nu)}^R(\mathbf{k}, \mathbf{k} + \mathbf{q}, \sigma, -\sigma; \mathbf{q}, \omega), \quad (6.24)$$

with $p_T(x)$ as defined in Eq. (2.12).

Due to the presence of particle-hole excitations at zero energy, the magnon excitations are broadened because of Landau damping. We assume that the spectral function of the spin fluctuations divided by ω has a broader peak at $\omega = 0$ than the function $p_T(\omega)$, which describes the available phase space for spin-fluctuation excitations and has a width of order $k_B T$. For sufficiently low temperatures we can thus approximate

$$W_{\mu\mathbf{k}}^{\nu\mathbf{k}+\mathbf{q}} \approx p_T(\omega) \lim_{\omega \rightarrow 0} \frac{\text{Im} S_{(\nu\mu),(\mu\nu)}^R(\mathbf{k}, \mathbf{k} + \mathbf{q}, \sigma, -\sigma; \mathbf{q}, \omega)}{\omega}, \quad (6.25)$$

where we have dropped the spin indices on the left-hand side since the spin-fluctuation propagator becomes independent of σ in the static limit. If the bandwidth is much smaller than $k_B T$, the scattering rate can be integrated over ω , giving a factor of $(\pi k_B T)^2$. Including also isotropic impurity scattering, the integrated scattering rate thus reads

$$W_{s\theta}^{s'\theta'} = (k_B T)^2 \lim_{\omega \rightarrow 0} \frac{\text{Im} S_{(\nu\mu),(\mu\nu)}^R(\mathbf{k}(\mu\theta), \mathbf{k}(\nu\theta'), \sigma, -\sigma; \mathbf{k}(\nu\theta') - \mathbf{k}(\mu\theta), \omega)}{\omega} + W_{\text{imp}}, \quad (6.26)$$

where we have parametrized the states on the Fermi surface by $s\theta$, as shown in the inset of Fig. 6.2: θ is the polar angle with respect to the k_x -axis (shifted by

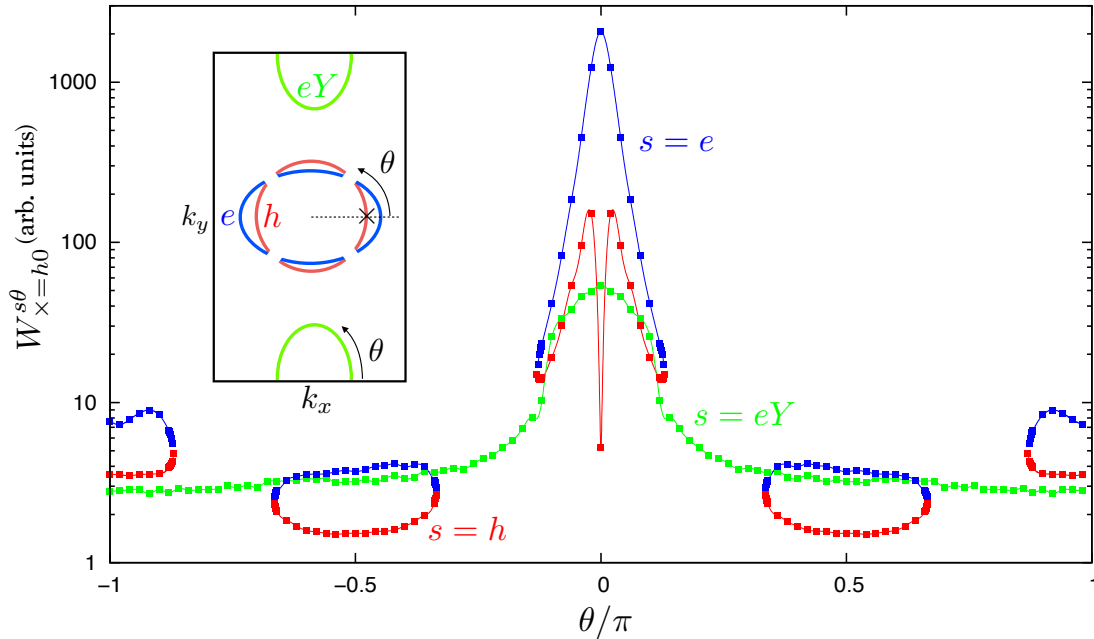


Figure 6.2: Scattering rate $W_{h_0}^{s\theta}$ as a function of the final state $s\theta$. The inset shows a sketch of the Fermi pockets. The symbol \times indicates the initial state for the scattering rate plotted in the main figure. The coupling constants are $g_1 = g_{2b} = 0$, $g_{cf} = 3.43 t_h$, $g_{2a} = 0.06 t_h$, which give a SDW-ordering temperature of $T_N = 0.065 t_h/k_B$. The temperature is set to $T = 0.93 T_N$, the filling is $n = 2.085$, and the ellipticity of the electron pockets is $\xi = 1$. The remaining band parameters are as in chapter 4.

$(0, \pi)$ for the pocket eY), $s = eY$ refers to the electron pocket that is weakly reconstructed, $s = e$ denotes those parts of the banana pockets that stem from the strongly reconstructed electron pocket, and $s = h$ denotes the parts that stem from the hole pocket.

The numerical calculation of the scattering rate consists of several steps and is partially similar to the numerical calculations in Ref. [55], where additional details can be found. We determine the mean-field state by a standard self-consistent iteration procedure. The bare susceptibilities are calculated according to Eq. (6.21), involving a summation over the Brillouin zone. The RPA susceptibility is obtained by numerical matrix inversion. The calculation of the propagator in Eq. (6.23) is similar to the calculation of the effective interaction vertex for Cooper pairing considered in Ref. [55]. For the limit $\omega \rightarrow 0$ in Eq. (6.26), we took a finite $\omega = 10^{-5} t_h$.

The scattering rate for an initial state $|s = h, \theta = 0\rangle$ is plotted in Fig. 6.2.

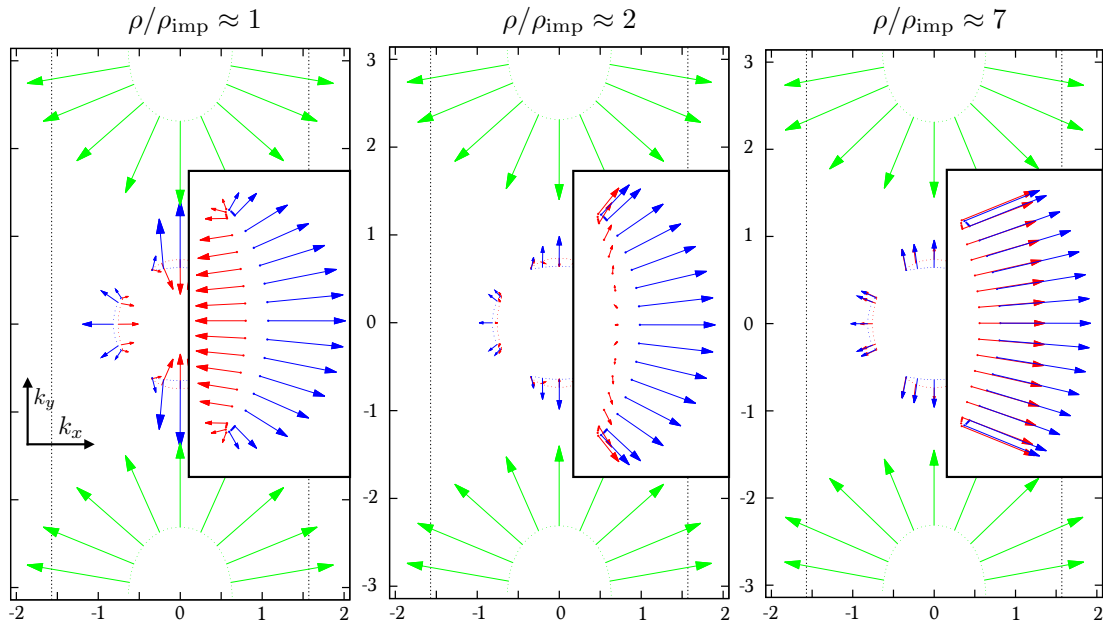


Figure 6.3: MFPs $\Lambda_{s\theta}^{(0)}$ (arrows) for states on the Fermi pockets for three different ratios $\rho/\rho_{\text{imp}} \approx 1, 2, 7$. The insets show close-ups of the right-hand banana pocket. The dashed line indicates the Brillouin zone boundary. The lattice constants are set to unity, $a_{\text{O}} \approx b_{\text{O}} \equiv 1$.

We see that the strongest scattering is found between states at different sides e and h of the banana pockets at nearly the same polar angle θ . It stems from the strong interpocket scattering between states initially separated by $\mathbf{q} \approx \mathbf{Q}$ in the paramagnetic phase, which has been discussed in chapters 4 and 5. Due to band reconstruction, the enhanced interpocket scattering at $T > T_N$ transforms into intrapocket scattering within the reconstructed pockets at $T < T_N$. In Fig. 6.2 we also see clearly that $\mathbf{q} \approx 0$ scattering is suppressed, in agreement with Adler's theorem [121].

With the scattering rate shown in Fig. 6.2 we can calculate the MFP in the absence of a magnetic field, $\Lambda_{s\theta}^{(0)}$, by solving the Boltzmann equation (4.8) numerically, similar to chapter 4. Discretizing the states on the pockets, we use 100 points for each $s = eY, e, h$ (see inset of Fig. 6.2) with a higher density of points at the turning points of the banana pockets.

It is interesting to compare the results for the MFP for different strengths of the spin-fluctuation scattering compared to the impurity scattering. We choose the strength of impurity scattering in Eq. (6.26) in such a way that the ratio ρ/ρ_{imp} is fixed, where ρ is the total resistivity and ρ_{imp} is the resistivity due to

impurity scattering alone. Realistic values for this ratio can be roughly estimated by comparison with the experimental resistivity ratios just below T_N and at $T = 0$, where spin fluctuations are “frozen out” and only impurity scattering contributes. According to measurements in Refs. [2, 99], typical ratios are $\rho/\rho_{\text{imp}} \approx 2$ and $\rho/\rho_{\text{imp}} \approx 10$ for as-grown and annealed 122 pnictides, respectively.

The results for the MFP for three characteristic ratios are shown in Fig. 6.3. In the figure we clearly see that increasing the strength of scattering due to spin fluctuations tends to equalize the MFPs on opposite sides of the banana pockets at the same polar angle θ . In the realistic case of $\rho/\rho_{\text{imp}} \approx 7$, we find approximately $\Lambda_{h\theta}^{(0)} \approx \Lambda_{e\theta}^{(0)}$. We can understand this by comparison to the situation in the paramagnetic phase discussed in chapter 4. In section 4.3 we found analytical expressions for the MFPs, see Eqs. (4.12)–(4.14), which revealed that the MFPs of the three states $|s'\theta\rangle$ with $s' = eX, eY, h$ at the same polar angle but on different pockets become equal in the strong-anisotropy limit. The interpretation was that due to enhanced scattering with momentum changes of $\mathbf{q} \approx (\pi, 0)$ or $\mathbf{q} \approx (0, \pi)$, during the relaxation time electrons are hopping between the states $|s'\theta\rangle$ at a fixed polar angle θ . Consequently, no matter which state the electron starts in, it tends to be scattered along a very similar path before being randomized. For the SDW phase, Fig. 6.2 shows that scattering is much stronger between $|e\theta\rangle$ and $|h\theta\rangle$ than between $|eY\theta\rangle$ and $|h\theta\rangle$. In this case, Eqs. (4.12)–(4.14) can be simplified as we can set $a_{h\theta}^{eY} = a_{eY\theta}^h \approx 0$. Otherwise, the situation is similar to the paramagnetic phase. In particular, we see that the MFP is not suppressed at the tips (also called turning points) of the banana pockets. Thus the mechanism of interrupted orbital motion due to suppressed relaxation times, as mentioned in Ref. [118], is not relevant here. We will see in the next section that orbital motion is nevertheless interrupted, although the mechanism of the interruption is different. The changed pocket topology in the SDW phase is crucial and leads to effects which cannot be found in the paramagnetic phase.

6.4 Interrupted orbital motion

According to the numerical results for the MFP for the realistic case $\rho/\rho_0 \sim 7$, the MFP on the two sides of the reconstructed pockets are nearly equal, $\Lambda_{h\theta}^{(0)} \approx \Lambda_{e\theta}^{(0)}$. To focus on the effect of the magnetic field, we assume for simplicity $\Lambda_{h\theta}^{(0)} = \Lambda_{e\theta}^{(0)} \equiv \Lambda_{\theta}^{(0)}$ and take

$$\Lambda_{\theta}^{(0)x} + i\Lambda_{\theta}^{(0)y} = l e^{i\theta}. \quad (6.27)$$

We include the magnetic field using the formalism described in section 2.4: The ansatz for the total MFP in the presence of the magnetic field $\mathbf{B} = B \mathbf{z}$ is written as $\Lambda_{s\theta} = \sum_{n=0}^{\infty} \Lambda_{s\theta}^{(n)}$ where $\Lambda_{s\theta}^{(n)}$ is of order n in B . For $\Lambda_{s\theta}^{(1)}$ one has to replace $\mathbf{v}_{s\theta}$ in the solution for $\Lambda_{s\theta}^{(0)}$ by $\omega_{s\theta} \partial_{\theta} \Lambda_{s\theta}^{(0)}$, where $\omega_{s\theta} = \eta_s e B / (\pi \hbar^2 N_{s\theta})$ is the cyclotron frequency of an electron in the state $s\theta$, $\eta_h = -1$, $\eta_e = 1$, and $N_{s\theta} \equiv |d\mathbf{k}_{s\theta}/d\theta| / |\pi \hbar \mathbf{v}_{s\theta}|$ is the state-resolved density of states. All higher-order terms $\Lambda_{s\theta}^{(n)}$ are obtained by increasing the order index by one in the solution of the previous order. Hence, an analytical solution for $\Lambda_{s\theta}^{(0)}$ determines $\Lambda_{s\theta}$, the MFP for $B \neq 0$.

An analytical solution for $\Lambda_{s\theta}^{(0)}$ has been provided in section 4.3. In the strong anisotropy limit, $a \approx 1$, the result can be written in the form

$$\Lambda_{\theta}^{(0)} = \tau (p_e \mathbf{v}_{e\theta} + p_h \mathbf{v}_{h\theta}), \quad (6.28)$$

with some positive and dimensionless coefficients $p_{e,h}$ with $p_e + p_h = 1$ and $\tau > 0$, which can be interpreted as an effective relaxation time. From Eq. (6.28) it follows that the full MFP Λ_{θ} satisfies

$$\begin{aligned} \Lambda_{\theta} &= \Lambda_{\theta}^{(0)} + \Omega_{\theta} \partial_{\theta} \Lambda_{\theta}^{(0)} + \Omega_{\theta} \partial_{\theta} (\Omega_{\theta} \partial_{\theta} \Lambda_{\theta}^{(0)}) + \dots \\ &= \Lambda_{\theta}^{(0)} + \Omega_{\theta} \partial_{\theta} \Lambda_{\theta}, \end{aligned} \quad (6.29)$$

where

$$\Omega_{\theta} = \tau (p_e \omega_{e\theta} + p_h \omega_{h\theta}) \equiv \beta_{\theta} B. \quad (6.30)$$

The factor

$$\beta_{\theta} = \tau \left(\frac{p_e}{\pi \hbar N_{e\theta}} - \frac{p_h}{\pi \hbar N_{h\theta}} \right) \frac{e}{\hbar} \quad (6.31)$$

will be called *deflection factor* in the following. The sign of Ω_{θ} is given by $\text{sgn}[(p_e/N_{e\theta} - p_h/N_{h\theta})B]$. For clarity we will assume $\Omega_{\theta} \geq 0$ in the following—the other case can be obtained by symmetry considerations.

In section 2.4 we have demonstrated that the change of the MFP in the presence of a magnetic field is due to the orbital motion of electrons along the Fermi line. Let us now consider the orbital motion on one banana pocket, as described by Eq. (6.29). We can divide the banana pocket into nearly circular regions for $-\bar{\theta} \leq \theta \leq \bar{\theta}$ and small turning regions near the “banana tips” $\bar{\theta} \leq \theta \leq (\bar{\theta} + \epsilon)$ and $-(\bar{\theta} + \epsilon) \leq \theta \leq -\bar{\theta}$ as indicated in Fig. 6.4. For the circular regions, we can assume constant densities of states $N_{s\theta}$ and therefore $\Omega_{\theta} \equiv \Omega$. For the turning regions, the Fermi line changes from perpendicular to the radial vector at $\theta = \pm\bar{\theta}$ to parallel

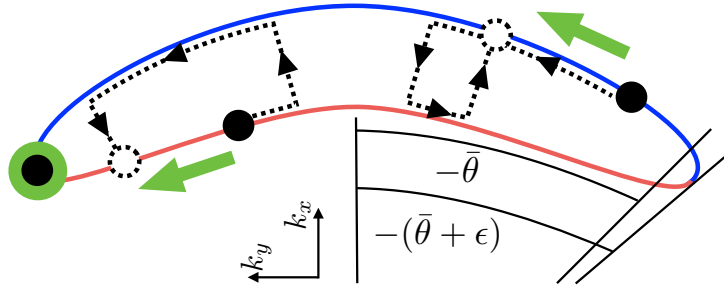


Figure 6.4: Orbital motion on the banana pocket with strong scattering between opposite sides of the pocket. Due to scattering, the effective motion along the Fermi line (indicated by the green arrows) changes sign at the turning point of the pocket. An electron at the turning point $\bar{\theta} + \epsilon$ thus effectively does not move any further.

at $\theta = \pm(\bar{\theta} + \epsilon)$. The state-resolved density of states $N_{s\theta} \equiv |d\mathbf{k}_{s\theta}/d\theta|/|\pi\hbar\mathbf{v}_{s\theta}|$ in our parametrization thus becomes infinite at $\theta = \pm(\bar{\theta} + \epsilon)$ and with that $\Omega_{\pm(\bar{\theta} + \epsilon)} = 0$. This alone does not necessarily signify an interruption of the orbital motion since a diverging $\partial_{\theta}\mathbf{\Lambda}_{\theta}^{(0)}$ can lift the suppressed Ω_{θ} at $\theta = \pm(\bar{\theta} + \epsilon)$. This would happen if the MFP were parallel to the velocity, as is the case within the Drude approximation, $\mathbf{\Lambda}_{\theta}^{(0)} = \mathbf{\Lambda}_{\theta}^D \equiv \tau_{s\theta}\mathbf{v}_{s\theta}$. Crucially, in the considered case $\partial_{\theta}\mathbf{\Lambda}_{\theta}^{(0)}$ is finite at $\theta = \pm(\bar{\theta} + \epsilon)$ due to spin-fluctuation scattering equalizing the MFP on both sides of the pocket. According to Eq. (6.29) together with $\Omega_{\pm(\bar{\theta} + \epsilon)} = 0$ this leads to

$$\mathbf{\Lambda}_{\pm(\bar{\theta} + \epsilon)} = \mathbf{\Lambda}_{\pm(\bar{\theta} + \epsilon)}^{(0)}, \quad (6.32)$$

i.e., no orbital motion at $\theta = \pm(\bar{\theta} + \epsilon)$. We can understand this semiclassically in the following way: The Lorentz force changes the momentum of an electron according to $\hbar d\mathbf{k}/dt = (eB/\hbar)\mathbf{z} \times \mathbf{v}_{\mathbf{k}}$. In case of the isotropic scattering, this leads to a clockwise (counterclockwise) orbital motion on an electronlike (holelike) FS. In the considered case, however, the electrons scatter much more strongly between states on the opposite sides of the banana pocket than to other states. We have already discussed in section 6.3 that due to this scattering the MFPs of the electrons on the opposite sides become equal. As illustrated in Fig. 6.4, this also leads to an equalized orbital motion on opposite sides such that the electrons on one of the two sides are effectively deflected in the opposite direction compared to the direction if the scattering were isotropic. Which side dominates with regard to the orbital motion is determined by the sign of the deflection factor in Eq. (6.31). Hence, we find that the motion along the Fermi line changes its direction

and is therefore zero at the turning point. In contrast, within the scenario of Refs. [118, 119] interrupted orbital motion is due to suppressed relaxation times and the motion along the Fermi line does *not* change its direction.

With the boundary condition, Eq. (6.32), the solution to the differential equation (6.29) reads

$$\Lambda_\theta = \int_\theta^{\bar{\theta}+\epsilon} d\theta' \frac{\Lambda_{\theta'}^{(0)}}{\Omega_{\theta'}} \exp\left(-\int_\theta^{\theta'} d\theta'' \frac{1}{\Omega_{\theta''}}\right) + \Lambda_{\bar{\theta}+\epsilon}^{(0)} \exp\left(-\int_\theta^{\bar{\theta}+\epsilon} d\theta'' \frac{1}{\Omega_{\theta''}}\right). \quad (6.33)$$

Assuming a small ϵ , we can take $\Lambda_{\theta'}^{(0)} \approx \Lambda_{\bar{\theta}}^{(0)}$ for $\bar{\theta} \leq \theta' \leq \bar{\theta} + \epsilon$. A straightforward calculation then leads to

$$\Lambda_\theta = \int_\theta^{\bar{\theta}} d\theta' \frac{\Lambda_{\theta'}^{(0)}}{\Omega} e^{-(\theta'-\theta)/\Omega} + e^{-(\bar{\theta}-\theta)/\Omega} \Lambda_{\bar{\theta}}^{(0)}. \quad (6.34)$$

Using Eq. (6.27), we find

$$\Lambda_\theta^x + i\Lambda_\theta^y = \frac{l}{1 + \Omega^2} \left[e^{i\theta}(1 + i\Omega) + \Omega e^{-(\bar{\theta}-\theta)/\Omega} e^{i\bar{\theta}}(\Omega - i) \right], \quad (6.35)$$

which is the final result for the MFP in the presence of a magnetic field of arbitrary strength. The second term in the brackets is an anomalous term coming from the interruption of orbital motion at the turning point. We see that the anomalous term gives rise to a finite MFP in the limit $B \rightarrow \infty$. In the next section we will see that interrupted orbital motion on reconstructed pockets leads to characteristic signatures in the magnetoresistance.

6.5 Magnetoresistance

To calculate the magnetoresistance I divide the total conductivity $\sigma = \sigma_o + \sigma_b$ in a normal contribution σ_o and a contribution from the banana pockets with interrupted orbital motion, σ_b . To keep the discussion clear, I will assume only one pair of banana pockets and model the normal contribution by a circular pocket. This is sufficient to discuss the qualitative aspects of the signatures of interrupted orbital motion. The generalization to four banana pockets with interrupted orbital motion and non-circular pockets with normal motion is straightforward. The

conductivity of the circular Fermi pocket reads

$$\sigma_{\circ}^{xx}(B) = \sigma_{\circ}^{yy}(B) = \sigma_{\circ}(0) \frac{1}{1 + \Omega_{\circ}^2}, \quad (6.36)$$

$$\sigma_{\circ}^{xy}(B) = -\sigma_{\circ}^{yx}(B) = \sigma_{\circ}(0) \frac{\Omega_{\circ}}{1 + \Omega_{\circ}^2}, \quad (6.37)$$

where $\sigma_{\circ}(0) \equiv \sigma_{\circ}^{yy}(0) = \sigma_{\circ}^{xx}(0)$ and $\Omega_{\circ} = \beta_{\circ}B$. For the banana pockets the contributions from $\bar{\theta} \leq \theta \leq \bar{\theta} + \epsilon$ are negligible. Assuming the velocity to be a constant radial vector, we calculate from Eq. (6.35),

$$\begin{aligned} \sigma_b^{xx}(B) + i\sigma_b^{xy}(B) &= \frac{\sigma_b(0)}{1 + \Omega^2} (\bar{\theta}^2 - \sin^2 \bar{\theta} \cos^2 \bar{\theta})^{-\frac{1}{2}} \left\{ [\bar{\theta} + \sin \bar{\theta} \cos \bar{\theta}] [1 + i\Omega] \right. \\ &\quad \left. + \frac{2\Omega^2}{1 + \Omega^2} e^{-\frac{\bar{\theta}}{\Omega}} \left[\Omega \sin \bar{\theta} \cosh \frac{\bar{\theta}}{\Omega} + \cos \bar{\theta} \sinh \frac{\bar{\theta}}{\Omega} \right] e^{i\bar{\theta}} [\Omega - i] \right\}, \end{aligned} \quad (6.38)$$

$$\begin{aligned} \sigma_b^{yy}(B) + i\sigma_b^{yx}(B) &= \frac{\sigma_b(0)}{1 + \Omega^2} (\bar{\theta}^2 - \sin^2 \bar{\theta} \cos^2 \bar{\theta})^{-\frac{1}{2}} \left\{ [\bar{\theta} - \sin \bar{\theta} \cos \bar{\theta}] [1 - i\Omega] \right. \\ &\quad \left. + \frac{2\Omega^2}{1 + \Omega^2} e^{-\frac{\bar{\theta}}{\Omega}} \left[\sin \bar{\theta} \cosh \frac{\bar{\theta}}{\Omega} - \Omega \cos \bar{\theta} \sinh \frac{\bar{\theta}}{\Omega} \right] e^{-i\bar{\theta}} [i\Omega - 1] \right\}, \end{aligned} \quad (6.39)$$

where $\sigma_b(0) \equiv \sqrt{\sigma_b^{xx}(0)\sigma_b^{yy}(0)}$. The resistivity is determined by inverting the conductivity tensor.

Due to broken C_4 symmetry, the resistivity is anisotropic, i.e., the resistivity parallel to the current depends on the direction ϕ of the current in the xy -plane. It would thus be most useful to compare it to measurements on single crystals. However, so far magnetoresistance measurements, to my knowledge, exist only for twinned crystals [112, 116], in which the sample as a whole restores the C_4 symmetry and resistivity is isotropic. I have shown in section 2.5 that there exists an exact relation between the conductivity of the single crystal and the corresponding conductivity $\bar{\sigma}$ of the twinned crystal [75]. The relation reads

$$\bar{\sigma}^{xx} = \bar{\sigma}^{yy} = \sqrt{\sigma^{xx}\sigma^{yy} - \left(\frac{\sigma^{xy} + \sigma^{yx}}{2}\right)^2}, \quad (6.40)$$

$$\bar{\sigma}^{xy} = -\bar{\sigma}^{yx} = \frac{\sigma^{xy} - \sigma^{yx}}{2}. \quad (6.41)$$

and is the same as between the conductivities of single crystals and polycrystals [77].

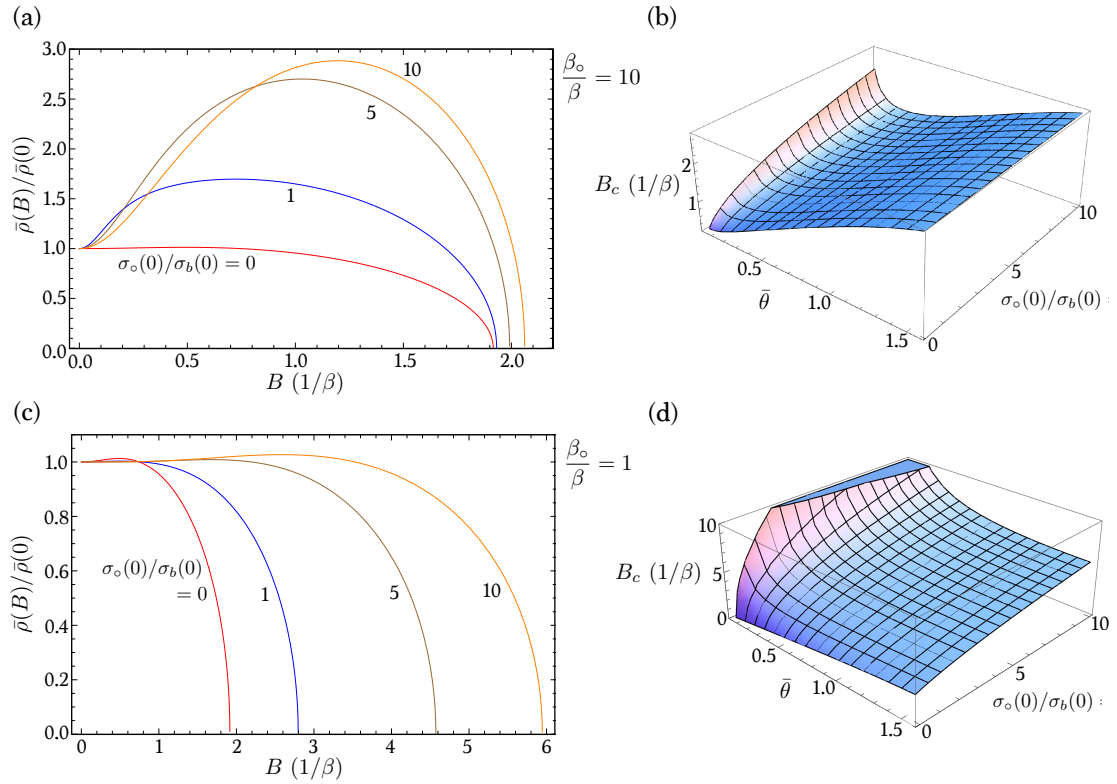


Figure 6.5: Magnetoresistance of twinned crystals and polycrystals. (a) Magnetoresistance for $\bar{\theta} = \pi/3$, $\beta_o/\beta = 10$, and different ratios of zero-field conductivities $\sigma_o(0)/\sigma_b(0)$. (b) Critical magnetic field at which $\bar{\rho}(B) = 0$ as a function of $\bar{\theta}$ and $\sigma_o(0)/\sigma_b(0)$ for $\beta_o/\beta = 10$. (c), (d) same as (a), (b) but for $\beta_o/\beta = 1$. For $B > B_c$, the conductivity tensor of a single domain is no longer positive definite, indicating a thermodynamic instability of the considered state.

We will first consider the magnetoresistance of *twinned* crystals (or, equivalently, polycrystals), $\bar{\rho}(B) = \bar{\sigma}^{xx}/[(\bar{\sigma}^{xx})^2 + (\bar{\sigma}^{xy})^2]$. Figure 6.5 shows the magnetoresistance for different ratios $\sigma_o(0)/\sigma_b(0)$. Since the deflection factor β is an average of the deflection factors from different sides of the banana pocket, which have different signs, it is reasonable to assume that $\beta_o > \beta$. In Fig. 6.5 we see that there exists a critical magnetic field at which the resistivity drops to zero. According to Eq. (6.41), at the critical field

$$\sigma^{xx}\sigma^{yy}\Big|_{B=B_c} = \left(\frac{\sigma^{xy} + \sigma^{yx}}{2}\right)^2\Big|_{B=B_c}, \quad (6.42)$$

which marks the crossover at which the conductivity tensor of single domains, σ , loses the positive semidefiniteness. For $B > B_c$, the conductivity tensor is not positive semidefinite, which means that a charge current in certain crystallographic directions reduces the entropy of the system. The state of a single domain thus becomes unstable [80], probably towards a charge-modulated state. The investigation of the state for $B > B_c$ goes beyond the scope of this work, but is an intriguing direction for future study. Figures 6.5(b) and (d) indicate that the critical field exists for arbitrary sizes of the reconstructed pockets and for arbitrary strengths of the zero-field conductivity. If the deflection factor on the banana pocket is much smaller than that of other pockets, the critical magnetic field is nearly independent of $\sigma_o(0)/\sigma_b(0)$.

We now come to the magnetoresistance of *detwinned* single crystals. The results are shown in Fig. 6.6. Most importantly, we find a signature of interrupted orbital motion already in the low-field magnetoresistance. The pockets with interrupted orbital motion give a contribution to the magnetoresistance that is linear in B , in contrast to pockets without interruption, which give a contribution that is quadratic in B . Thus at $B = 0$ the differential magnetoresistance $d[\rho(B)/\rho(0)]/dB$ is finite only due to the pockets with interrupted orbital motion. Most exotically, the linear term is negative for $\phi \in [-\pi/2, 0]$ and $\phi \in [\pi/2, \pi]$ and is independent of β_o/β . At $B = B_c$ the resistivity is zero for the current direction ϕ that minimizes the resistivity. The current flow in this direction is thus dissipationless. For $B > B_c$ the resistivity for this direction is formally negative. The instability of a system with negative resistivity is obvious, since a charge flow can reinforce the electric field which has produced the charge flow in the first place.

It is difficult to find a complete semiclassical explanation of the results but we can partially understand the behavior of the magnetoresistance in the following

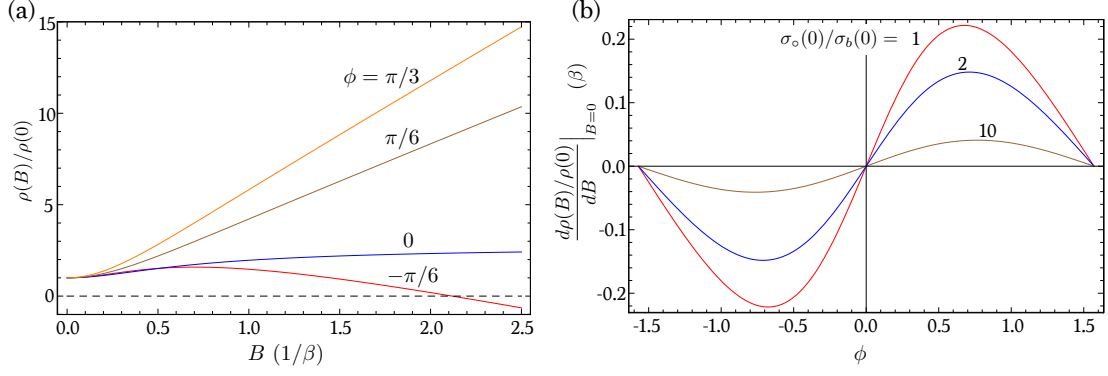


Figure 6.6: Magnetoresistance of detwinned single crystals. (a) Magnetoresistance for $\bar{\theta} = \pi/3$, $\beta_o/\beta = 10$, and $\sigma_o(0)/\sigma_b(0) = 10$ for different directions ϕ of the current. In the direction $\phi \approx -\pi/6$ the resistivity becomes negative at $\beta B \approx 2.1$. Negative resistivity indicates a thermodynamic instability of the system. (b) Differential magnetoresistance at $B = 0$ as a function of ϕ for $\bar{\theta} = \pi/3$ and different $\sigma_o(0)/\sigma_b(0)$. The differential magnetoresistance does not depend on β_o/β .

way: Consider the total resistance of a system composed of two parallel connected resistors A and B, where A corresponds to the usual Fermi pockets and B to the pockets with interrupted orbital motion. The resistivity of A will grow proportional to B^2 until it saturates for $\beta_o B \sim 1$, which is the usual behavior of metals [74]. On the other hand, the resistivity of B goes to zero when the interruption affects the majority of states on the pocket. This happens as soon as the effective cyclotron frequency is on the order of the effective relaxation time. In our formalism this corresponds to $\beta B \sim 1$. Since the total resistance of two parallel resistors is set by the smaller one, the total resistance becomes zero as soon as the resistance of B goes to zero. Thus a critical magnetic field with $\beta B_c \sim 1$ exists independently of the existence of other carriers in the system.

It remains to understand the drop of the resistivity of the resistor B. Here it is useful to recall the semiclassical picture for the magnetoresistance of conventional metals. It is intuitively clear that for $\beta B \sim 1$ the orbital motion of electrons leads, on the one hand, to a randomization of the effective velocity of electrons and, on the other hand, to an increase of the Hall electric field. An increased Hall electric field increases the total electric field such that the electrons are additionally accelerated. The two effects compete since the randomization of velocity enlarges the resistivity, while the accelerating effect of the Hall electric field reduces the resistivity. For a conventional metal, the first effect dominates, leading to a po-

sitive magnetoresistance. For FSs with interrupted orbital motion however, the complete randomization of the velocity is impossible. Depending on the direction of the applied current, this can lead to a decrease of the resistivity due to the dominance of the accelerating effect of the Hall electric field.

6.6 Conclusions

To summarize, I have studied the scattering rate resulting from the interaction of electrons with spin fluctuations in the SDW phase. The spin-fluctuation spectrum includes the Goldstone mode and leads to strong scattering between different sides of the reconstructed banana pockets. We have seen that for a realistic strength of spin-fluctuation scattering, the MFPs on one side of each reconstructed pocket are inverted, which leads to the interruption of the orbital motion of electrons along the Fermi line in the presence of a magnetic field. The finite MFP of states at which the orbital motion stops makes the mechanism distinct from the one mentioned in Ref. [118] and leads to specific signatures in the magnetoresistance.

For twinned crystals and polycrystals the interrupted orbital motion implies a critical magnetic field at which the resistivity drops to zero and the system becomes thermodynamically unstable. The critical magnetic field strength depends on details of the system, but should be such that the effective cyclotron frequency is on the order of the inverse effective relaxation time. For detwinned crystals, on the other hand, I have found signatures of interrupted orbital motion already for weak magnetic fields. I predict a linear magnetoresistance which oscillates as a function of the direction of the current, ϕ , between negative and positive values with nodes at $\phi = n \pi/2$, where n is an integer. Positive linear magnetoresistance could also appear due to the Dirac spectrum [47, 112, 117] or due to a large velocity change at the turning points of the banana-shaped pockets [118]. However, none of these scenarios predicts a *negative* magnetoresistance. Direction-resolved measurements of the magnetoresistance for detwinned samples would therefore be a decisive test of the mechanism proposed in this chapter. However, to my knowledge, measurements of magnetoresistance of detwinned single crystals do not exist so far.

7 Summary and outlook

In this work I have investigated transport in multiband metals close to an excitonic instability. The main theoretical challenge has been the inclusion of collective fluctuations, which give rise to anisotropic scattering of electrons. I found a simple model in which the transport problem could be solved analytically even in case of strong scattering anisotropy [17]. The results uncovered a mechanism which may explain the suppressed magnetoresistance in connection with an enhanced Hall coefficient, measured in paramagnetic iron pnictides [3]. The analysis has shown that this effect is connected to the occurrence of negative transport times of minority carriers.

In a more advanced model including several characteristics of the iron pnictide FS, I studied the role of spin fluctuations in the transport behavior of these materials [18]. An approximate analytic solution has been discussed, along with full numerical calculations. The analytical results, which have shown a qualitative agreement with those obtained numerically, have been helpful to understand the unexpectedly large contribution of hot spots to the transport. The hot spots were found to not be “short circuited” by the cold regions of the FS, in contrast to the situation in cuprates and heavy-fermion materials. Further, we have seen that scattering anisotropy and the elliptical shape of the electron pockets leads to an effective Lorentz force [122], which shifts the electrons along the Fermi line towards the closest hot spot. The effect increases with increasing ellipticity and increasing scattering anisotropies.

Doping and temperature dependence of several transport coefficients has been considered. The anomalous temperature behavior qualitatively reproduces some aspects of the transport anomalies of iron pnictides. It could be ascribed to the temperature dependence of the scattering anisotropy, which in turn is due to the temperature-dependence of the available spin-fluctuation spectrum. In the nematic phase the strong contribution of hot spots could explain the huge resistive anisotropy measured in 122 pnictides [19]. The calculations have reproduced the characteristic doping dependence and have explained the difference between

annealed and as-frown samples without the assumption of anisotropic impurity states.

The most striking effects have been predicted for the SDW phase. Here, back-folding of the bands and the SDW gap lead to reconstructed pockets, which are banana-shaped for temperatures close to T_N . The presence of damped magnon excitations leads to strong scattering of electrons between opposite sides of the banana pockets. In principle, this scattering resembles the scattering between the electron and hole pockets in the paramagnetic phase. However, in the SDW phase the changed pocket topology leads to an unusual effect in the presence of an external magnetic field: The orbital motion becomes interrupted at the turning points of the banana pockets. In high magnetic fields the interrupted orbital motion makes the system unstable, which is characterized by a drop of the resistivity to zero. For low magnetic fields, my calculations predict a strong difference between the magnetoresistance of detwinned single crystals and twinned crystals or polycrystals. While there is no clear signature of interrupted orbital motion in twinned crystals or polycrystals, in detwinned single crystals the low-field magnetoresistance is linear with alternating sign of the slope as a function of the direction of the current. To my knowledge there are no other mechanisms which could explain such an effect, the measurement of which would thus be a decisive test of the theory.

Finally, some ideas for further investigations in this field should be given. There has been very little research considering the role of AL (Aslamazov-Larkin) vertex corrections for the conductivity in connection with scattering due to spin fluctuations. I have discussed in chapter 2 that, based on the results for cuprates [72], AL terms are suppressed in the specific case of short-ranged electron-electron interaction and commensurate fluctuations. To my knowledge, explicit calculations of AL vertex corrections in the multiband case have not been performed so far.

With regard to the physics of iron pnictides, it would be very interesting to consider orbital models and compare the impact of spin *and* orbital fluctuations on transport. A comparison with transport measurements could then be helpful to determine the dominant fluctuations, which could shed light on the mechanism of, e.g., the high-temperature superconductivity in these materials. As discussed in chapter 6, orbital models are especially important to consider the temperature dependence of transport coefficients in the SDW phase. This is because orbital models correctly include the topologically protected Dirac nodes in the spectrum [46, 114, 115]. So far, Dirac fermions in the SDW phase of iron pnictides [112]

received only little attention, although it has been proposed that they might significantly contribute to transport due to reduced relaxation rates [47]. The reduced relaxation rates are an effect of the Berry phase, which leads to suppressed backscattering of Dirac fermions [113].

Bibliography

- [1] A. Stern, *Ann. Phys. (NY)* **323**, 204 (2008).
- [2] J.-H. Chu, J. G. Analytis, K. De Greve, P. L. McMahon, Z. Islam, Y. Yamamoto, and I. R. Fisher, *Science* **329**, 824 (2010).
- [3] M. J. Eom, S. W. Na, C. Hoch, R. K. Kremer, and J. S. Kim, *Phys. Rev. B* **85**, 024536 (2012).
- [4] B. Shen, H. Yang, Z.-S. Wang, F. Han, B. Zeng, L. Shan, C. Ren, and H.-H. Wen, *Phys. Rev. B* **84**, 184512 (2011).
- [5] S. Kasahara, K. Hashimoto, H. Ikeda, T. Terashima, Y. Matsuda, and T. Shibauchi, *Phys. Rev. B* **85**, 060503(R) (2011).
- [6] S. M. Watts, S. Wirth, S. von Molnár, A. Barry, and J. M. D. Coey, *Phys. Rev. B* **61**, 9621 (2000).
- [7] I. Pallecchi, G. Lamura, M. Tropeano, M. Putti, R. Viennois, E. Giannini, and D. Van der Marel, *Phys. Rev. B* **80**, 214511 (2009).
- [8] G. D. Mahan, *Many-Particle Physics* (Kluwer Academic, New York, 2000).
- [9] J. Rammer and H. Smith, *Rev. Mod. Phys.* **58**, 323 (1986).
- [10] T. Kita, *Prog. Theor. Phys.* **123**, 78 (2010).
- [11] M. E. Fisher and J. S. Langer, *Phys. Rev. Lett.* **20**, 665 (1968).
- [12] S. Alexander, J. S. Helman, and I. Balberg, *Phys. Rev. B* **13**, 304 (1976).
- [13] H. Kontani, *Rep. Prog. Phys.* **71**, 026501 (2008).
- [14] A. Rosch, *Phys. Rev. Lett.* **82**, 4280 (1998).
- [15] D. Jérôme, M. Rieux, and J. Friedel, *Philos. Mag.* **23**, 1061 (1971).

- [16] M. T. Béal-Monod, K. Maki, and H. Fukuyama, *J. Low Temp. Phys.* **9**, 73 (1972).
- [17] M. Breitzkreiz, P. M. R. Brydon, and C. Timm, *Phys. Rev. B* **88**, 085103 (2013).
- [18] M. Breitzkreiz, P. M. R. Brydon, and C. Timm, *Phys. Rev. B* **89**, 245106 (2014).
- [19] M. Breitzkreiz, P. M. R. Brydon, and C. Timm, *Phys. Rev. B* **90**, 121104(R) (2014).
- [20] L. V. Keldysh and Y. V. Kopayev, *Sov. Phys. Solid State* **6**, 2219 (1965).
- [21] D. Jérôme, T. M. Rice, and W. Kohn, *Phys. Rev.* **158**, 462 (1967).
- [22] N. I. Kulikov and V. V. Tugushev, *Sov. Phys. Uspekhi* **27**, 954 (1984).
- [23] D. Buker, *Phys. Rev. B* **54**, 5713 (1981).
- [24] P. M. R. Brydon, J. Schmiedt, and C. Timm, *Phys. Rev. B* **84**, 214510 (2011).
- [25] B. A. Volkov, Y. V. Kopayev, and A. I. Rusinov, *Sov. Phys. JETP* **41**, 952 (1976).
- [26] A. V. Chubukov, D. V. Efremov, and I. Eremin, *Phys. Rev. B* **78**, 134512 (2008).
- [27] I. I. Mazin and J. Schmalian, *Physica C* **469**, 614 (2009).
- [28] Y. Kamihara, T. Watanabe, M. Hirano, and H. Hosono, *J. Am. Chem. Soc.* **130**, 3296 (2008).
- [29] M. Rotter, M. Tegel, and D. Johrendt, *Phys. Rev. Lett.* **101**, 107006 (2008).
- [30] Z.-A. Ren, W. Lu, J. Yang, W. Yi, X.-L. Shen, Z.-C. Li, G.-C. Che, X.-L. Dong, L.-L. Sun, F. Zhou, et al., *Chin. Phys. Lett.* **25**, 2215 (2008).
- [31] X. Wang, Q. Liu, Y. Lv, and W. B. Gao, *Solid State Commun.* **148**, 538 (2008).
- [32] P. Dai, J. Hu, and E. Dagotto, *Nature Phys.* **8**, 709 (2012).

Bibliography

- [33] R. M. Fernandes, A. V. Chubukov, and J. Schmalian, *Nature Phys.* **10**, 97 (2014).
- [34] D. C. Johnston, *Adv. Phys.* **59**, 803 (2010).
- [35] J. Paglione and R. L. Greene, *Nature Phys.* **6**, 645 (2010).
- [36] A. V. Chubukov, *Ann. Rev. Condens. Matter Phys.* **3**, 57 (2012).
- [37] R. M. Fernandes, A. V. Chubukov, J. Knolle, I. Eremin, and J. Schmalian, *Phys. Rev. B* **85**, 109901 (2012).
- [38] J. C. Davis and P. J. Hirschfeld, *Nature Phys.* **10**, 184 (2014).
- [39] X. Wang, T. Wu, G. Wu, H. Chen, and Y. L. Xie, *Phys. Rev. Lett.* **102**, 117005 (2009).
- [40] M. A. Tanatar, N. Ni, G. D. Samolyuk, S. L. Bud'ko, P. C. Canfield, and R. Prozorov, *Phys. Rev. B* **79**, 134528 (2009).
- [41] K. Kuroki, S. Onari, R. Arita, H. Usui, Y. Tanaka, H. Kontani, and H. Aoki, *Phys. Rev. Lett.* **101**, 087004 (2008).
- [42] J. Lorenzana, G. Seibold, C. Ortix, and M. Grilli, *Phys. Rev. Lett.* **101**, 186402 (2008).
- [43] S. Raghu, X.-L. Qi, C.-X. Liu, D. J. Scalapino, and S.-C. Zhang, *Phys. Rev. B* **77**, 220503 (2008).
- [44] H. Kontani and Y. Yamakawa, *Phys. Rev. Lett.* **113**, 047001 (2014).
- [45] S. Onari and H. Kontani, *Phys. Rev. Lett.* **109**, 137001 (2012).
- [46] Y. Ran, F. Wang, H. Zhai, A. Vishwanath, and D. H. Lee, *Phys. Rev. B* **79**, 014505 (2009).
- [47] T. Morinari, E. Kaneshita, and T. Tohyama, *Phys. Rev. Lett.* **105**, 037203 (2010).
- [48] C. Liu, A. D. Palczewski, R. S. Dhaka, T. Kondo, R. M. Fernandes, E. D. Mun, H. Hodovanets, A. N. Thaler, J. Schmalian, S. L. Bud'ko, et al., *Phys. Rev. B* **84**, 020509 (2011).
- [49] I. Eremin and A. V. Chubukov, *Phys. Rev. B* **81**, 024511 (2010).

- [50] J. Knolle, I. Eremin, A. V. Chubukov, and R. Moessner, *Phys. Rev. B* **81**, 140506(R) (2010).
- [51] P. M. R. Brydon and C. Timm, *Phys. Rev. B* **79**, 180504 (2009).
- [52] R. M. Fernandes and J. Schmalian, *Supercond. Sci. Technol.* **25**, 084005 (2012).
- [53] R. M. Fernandes, E. Abrahams, and J. Schmalian, *Phys. Rev. Lett.* **107**, 217002 (2011).
- [54] L. Fanfarillo, E. Cappelluti, C. Castellani, and L. Benfatto, *Phys. Rev. Lett.* **109**, 096402 (2012).
- [55] J. Schmiedt, P. M. R. Brydon, and C. Timm, *Phys. Rev. B* **89**, 054515 (2014).
- [56] S. Graser, A. F. Kemper, T. A. Maier, H.-P. Cheng, P. J. Hirschfeld, and D. J. Scalapino, *Phys. Rev. B* **81**, 214503 (2010).
- [57] O. K. Andersen and L. Boeri, *Ann. Phys.* **1**, 8 (2011).
- [58] E. C. Blomberg, M. A. Tanatar, R. M. Fernandes, I. I. Mazin, B. Shen, H.-H. Wen, M. D. Johannes, J. Schmalian, and R. Prozorov, *Nature Commun.* **4**, 1914 (2013).
- [59] J. Zhang, R. Sknepnek, and J. Schmalian, *Phys. Rev. B* **82**, 134527 (2010).
- [60] D. S. Inosov, J. T. Park, P. Bourges, D. L. Sun, Y. Sidis, A. Schneidewind, K. Hradil, D. Haug, C. T. Lin, B. Keimer, et al., *Nature Phys.* **6**, 8 (2009).
- [61] S. O. Diallo, D. K. Pratt, R. M. Fernandes, W. Tian, J. L. Zarestky, M. Lumsden, T. G. Perring, C. L. Broholm, N. Ni, S. L. Bud'ko, et al., *Phys. Rev. B* **81**, 214407 (2010).
- [62] X. Lu, J. T. Park, R. Zhang, H. Luo, A. H. Nevidomskyy, Q. Si, and P. Dai, *Science* **345**, 657 (2014).
- [63] B. I. Halperin and T. M. Rice, *Rev. Mod. Phys.* **40**, 755 (1968).
- [64] E. Fawcett, H. L. Alberts, V. Y. Galkin, D. R. Noakes, and J. V. Yakhmi, *Rev. Mod. Phys.* **66**, 25 (1994).

Bibliography

- [65] G. Li, W. Z. Hu, D. Qian, D. Hsieh, M. Z. Hasan, E. Morosan, R. J. Cava, and N. L. Wang, *Phys. Rev. Lett.* **99**, 027404 (2007).
- [66] B. Y. K. Hu, *Phys. Rev. Lett.* **85**, 820 (2000).
- [67] Q. Han, Y. Chen, and Z. D. Wang, *EPL* **82**, 37007 (2008).
- [68] H. Kontani, *Phys. Rev. B* **64**, 054413 (2001).
- [69] H. Kohno and K. Yamada, *Prog. Theor. Phys.* **80**, 623 (1988).
- [70] L. P. Kadanoff and G. Baym, *Quantum statistical mechanics: Green's function methods in equilibrium and nonequilibrium problems* (Benjamin, New York, 1989).
- [71] M. J. Rice, *Phys. Rev.* **162**, 189 (1967).
- [72] H. Kontani, K. Kanki, and K. Ueda, *Phys. Rev. B* **59**, 14723 (1999).
- [73] P. L. Taylor, *Proc. R. Soc. A* **275**, 200 (1963).
- [74] J. M. Ziman, *Principles of the Theory of Solids* (Cambridge University Press, London, 1965).
- [75] M. A. Tanatar, A. Kreyssig, S. Nandi, N. Ni, S. L. Bud'ko, P. C. Canfield, A. I. Goldman, and R. Prozorov, *Phys. Rev. B* **79**, 180508(R) (2009).
- [76] A. M. Dykhne and I. M. Kaganova, *Phys. Rep.* **1573**, 263 (1997).
- [77] A. M. Dykhne and A. A. Snarski, *JETP* **102**, 475 (2006).
- [78] A. M. Dykhne, *Sov. Phys. JETP* **32**, 348 (1971).
- [79] A. M. Dykhne, *Sov. Phys. JETP* **32**, 63 (1971).
- [80] L. D. Landau, J. S. Bell, M. J. Kearsley, L. P. Pitaevskii, E. Lifshitz, and J. B. Sykes, *Electrodynamics of Continuous Media* (Pergamon Press, New York, 1984).
- [81] T. McLean and E. Paige, *J. Phys. Chem. Solids* **16**, 220 (1960).
- [82] R. A. Höpfel, J. Shah, P. A. Wolff, and A. C. Gossard, *Phys. Rev. Lett.* **56**, 2736 (1986).
- [83] P. Prelovšek, I. Sega, and T. Tohyama, *Phys. Rev. B* **80**, 014517 (2009).

- [84] A. F. Kemper, M. M. Korshunov, T. P. Devereaux, J. N. Fry, H.-P. Cheng, and P. J. Hirschfeld, *Phys. Rev. B* **83**, 184516 (2011).
- [85] L. Fang, H. Luo, P. Cheng, Z. Wang, Y. Jia, G. Mu, B. Shen, I. I. Mazin, L. Shan, C. Ren, et al., *Phys. Rev. B* **80**, 140508 (2009).
- [86] F. Rullier-Albenque, D. Colson, A. Forget, and H. Alloul, *Phys. Rev. Lett.* **109**, 187005 (2012).
- [87] R. Hlubina and T. M. Rice, *Phys. Rev. B* **51**, 9253 (1995).
- [88] S. Arsenijević, H. Hodovanets, R. Gaál, L. Forró, S. L. Bud'ko, and P. C. Canfield, *Phys. Rev. B* **87**, 224508 (2013).
- [89] A. J. Millis, *Phys. Rev. B* **42**, 167 (1990).
- [90] D. I. Pikulin, C. Y. Hou, and C. W. J. Beenakker, *Phys. Rev. B* **84**, 035133 (2011).
- [91] Z. W. Zhu, Z. A. Xu, X. Lin, G. H. Cao, C. M. Feng, G. F. Chen, Z. Li, J. L. Luo, and N. L. Wang, *New J. Phys.* **10**, 63021 (2008).
- [92] E. D. Mun, S. L. Bud'ko, N. Ni, and P. C. Canfield, *Phys. Rev. B* **80**, 054517 (2009).
- [93] A. Kondrat, J. E. Hamann-Borrero, N. Leps, M. Kosmala, O. Schumann, A. Köhler, J. Werner, G. Behr, M. Braden, R. Klingeler, et al., *Eur. Phys. J. B* **70**, 461 (2009).
- [94] M. Matusiak, Z. Bukowski, and J. Karpinski, *Phys. Rev. B* **81**, 020510(R) (2009).
- [95] K. Ohgushi and Y. Kiuchi, *Phys. Rev. B* **85**, 064522 (2012).
- [96] W. Lv and P. Phillips, *Phys. Rev. B* **84**, 174512 (2011).
- [97] V. Stanev and P. B. Littlewood, *Phys. Rev. B* **87**, 161122(R) (2013).
- [98] S. Liang, A. Moreo, and E. Dagotto, *Phys. Rev. Lett.* **111**, 047004 (2013).
- [99] S. Ishida, M. Nakajima, T. Liang, K. Kihou, C. H. Lee, A. Iyo, H. Eisaki, T. Kakeshita, Y. Tomioka, T. Ito, et al., *Phys. Rev. Lett.* **110**, 207001 (2013).

Bibliography

- [100] H. H. Kuo and I. R. Fisher, *Phys. Rev. Lett.* **112**, 227001 (2014).
- [101] J. J. Ying, X. F. Wang, T. Wu, Z. J. Xiang, R. H. Liu, Y. J. Yan, A. F. Wang, M. Zhang, G. J. Ye, P. Cheng, et al., *Phys. Rev. Lett.* **107**, 067001 (2011).
- [102] M. P. Allan, T.-M. Chuang, F. Masee, Y. Xie, N. Ni, S. L. Bud'ko, G. S. Boebinger, Q. Wang, D. S. Dessau, P. C. Canfield, et al., *Nature Phys.* **9**, 220 (2013).
- [103] Y. Inoue, Y. Yamakawa, and H. Kontani, *Phys. Rev. B* **85**, 224506 (2012).
- [104] M. N. Gastiasoro, P. J. Hirschfeld, and B. M. Andersen, *Phys. Rev. B* **89**, 100502(R) (2014).
- [105] M. N. Gastiasoro, I. Paul, Y. Wang, P. J. Hirschfeld, and B. M. Andersen, *Phys. Rev. Lett.* **113**, 127001 (2014).
- [106] S. Kasahara, T. Shibauchi, K. Hashimoto, K. Ikada, S. Tonegawa, R. Okazaki, H. Shishido, H. Ikeda, H. Takeya, K. Hirata, et al., *Phys. Rev. B* **81**, 184519 (2010).
- [107] M. Yi, D. Lu, J.-H. Chu, J. G. Analytis, A. P. Sorini, A. F. Kemper, B. Moritz, S.-K. Mo, R. G. Moore, M. Hashimoto, et al., *Proc. Natl. Acad. Sci. USA* **108**, 6878 (2011).
- [108] K. Nakayama, Y. Miyata, G. N. Phan, T. Sato, Y. Tanabe, T. Urata, K. Tanigaki, and T. Takahashi, *Phys. Rev. Lett.* **113**, 237001 (2014).
- [109] S. Graser, T. A. Maier, P. J. Hirschfeld, and D. J. Scalapino, *New J. Phys.* **11**, 025016 (2009).
- [110] F. Rullier-Albenque, D. Colson, and A. Forget, *Phys. Rev. B* **88**, 045105 (2013).
- [111] J. Hu, T. J. Liu, B. Qian, and Z. Q. Mao, *Phys. Rev. B* **88**, 094505 (2013).
- [112] K. K. Huynh, Y. Tanabe, and K. Tanigaki, *Phys. Rev. Lett.* **106**, 217004 (2011).
- [113] T. Ando, T. Nakanishi, and R. Saito, *J. Phys. Soc. Japan* **67**, 2857 (1998).
- [114] A. Lau and C. Timm, *Phys. Rev. B* **88**, 165402 (2013).

- [115] A. Lau and C. Timm, *Phys. Rev. B* **90**, 024517 (2014).
- [116] S. Ishida, T. Liang, M. Nakajima, K. Kihou, C. H. Lee, A. Iyo, H. Eisaki, T. Kakeshita, T. Kida, M. Hagiwara, et al., *Phys. Rev. B* **84**, 184514 (2011).
- [117] A. Abrikosov, *Phys. Rev. B* **58**, 2788 (1998).
- [118] A. E. Koshelev, *Phys. Rev. B* **88**, 060412 (2013).
- [119] A. Rosch, *Phys. Rev. B* **62**, 4945 (1999).
- [120] Y. Wang, M. N. Gastiasoro, B. M. Andersen, M. Tomić, H. O. Jeschke, R. Valentí, I. Paul, and P. J. Hirschfeld, *Phys. Rev. Lett.* **114**, 097003 (2015).
- [121] S. L. Adler, *Phys. Rev.* **137**, B1022 (1965).
- [122] C. M. Varma and E. Abrahams, *Phys. Rev. Lett.* **86**, 4652 (2001).

Acknowledgements

I finally want to say thank you to the people who have contributed to the writing of this thesis. First of all, my thanks go to my supervisor Carsten Timm, who gave me exactly as much support as I needed throughout my work at the TU Dresden. I can hardly imagine what he could have done better. Very importantly, he has given me enough freedom to develop my own ideas, which I strongly appreciate. I learned very much from him. My special thanks go also to Philip Brydon. I benefited a lot from the many discussions with him about physics and otherwise. It was a great pleasure to write papers together with him and Carsten. Philip and Carsten have also given very useful feedback on previous versions of this thesis.

I very much enjoyed my time at the TU Dresden, where I had many nice moments. Since this is customary, I will now list some of those people with whom I have spent maybe a little bit more time but I am sorry if I have forgotten someone important. These people are Jacob Schmiedt, Tim Ludwig, Darshan Joshi, Alexander Lau, Chris Koschenez, Oleksiy Kashuba, Fabian Zschoke, and Paolo Michetti.

At the end I want to thank my wife Marina and my daughter Christina for their patience, care, supply, and, of course, for their love.

Erklärung

Hiermit versichere ich, dass ich die vorliegende Arbeit ohne unzulässige Hilfe Dritter und ohne Benutzung anderer als der angegebenen Hilfsmittel angefertigt habe. Die aus fremden Quellen direkt oder indirekt übernommenen Gedanken sind als solche kenntlich gemacht. Die Arbeit wurde bisher weder im Inland noch im Ausland in gleicher oder ähnlicher Form einer anderen Prüfungsbehörde vorgelegt. Diese Dissertation wurde am Institut für theoretische Physik der Technischen Universität Dresden unter Betreuung von Herrn Prof. Dr. Carsten Timm angefertigt. Ich erkenne die Promotionsordnung der Fakultät Mathematik und Naturwissenschaften der Technischen Universität Dresden vom 23.02.2011 an.